

Analytical Methods Report 8804

**PREDICTION METHODS FOR POWERED LIFT VEHICLE AERODYNAMICS**

FINAL REPORT

Under Contract NAS2-12166

Prepared for:

NASA Ames Research Center  
Moffett Field, CA 94035

Prepared by:

PRIME CONTRACTOR

Sungyul Yoo and Brian Maskew  
Analytical Methods, Inc.  
2133 - 152nd Avenue N.E.  
Redmond, WA 98052  
(206) 643-9090

and

SUBCONTRACTOR

Donald W. Roberts  
AMTEC Engineering, Inc.  
11820 Northup Way  
Bellevue, WA 98005

N93-72448

Uncl us

29/02 0172868

(NASA-CR-184833) PREDICTION  
METHODS FOR POWERED LIFT VEHICLE  
AERODYNAMICS, PHASE 2 Final Report  
(Analytical Methods) 128 p

August 1988



## Report Documentation Page

1. Report No.	2. Government Accession No.	3. Recipient's Catalog No.
4. Title and Subtitle Prediction Methods for Powered Lift Vehicle Aerodynamics		5. Report Date March 1989
		6. Performing Organization Code
7. Author(s) Sungyul Yoo* and Brian Maskew* Donald W. Roberts**		8. Performing Organization Report No.
		10. Work Unit No.
9. Performing Organization Name and Address *Analytical Methods, Inc.      **Amtec Engineering, Inc. 2133 - 152nd Avenue N.E.      3055 - 112th Avenue N.E. Redmond, WA 98052      Suite 200 Bellevue, WA 98004		11. Contract or Grant No. NAS2-12166
		13. Type of Report and Period Covered Contractor Report - Final
12. Sponsoring Agency Name and Address National Aeronautics and Space Administration Ames Research Center Moffett Field, California 94035		14. Sponsoring Agency Code
15. Supplementary Notes Point of Contact: Mike Dudley, M/S N247-1 NASA Ames Research Center Moffett Field, CA 94035 TEL: (415) 694-5046		
16. Abstract This report summarizes work done in the Phase II project. A zonal method of iterative coupling between an inviscid code, VSAERO, and a viscous code, APPL, was employed. VSAERO, a low-order panel method, was modified to handle both an entire aircraft configuration and a jet wake/surface. APPL uses an accurate second-order, iterative, alternating-direction-implicit (ADI) algorithm to integrate the parabolized Navier-Stokes equations in a single marching pass through the domain and solves the jet region with a three-dimensional pressure equation to recover the elliptic effects. The jet model in VSAERO is refined to improve the stability of boundary relaxation and also to maintain a boundary shape. A correlation study with the available experimental data has been carried out to establish the range of validity of the method using a jet on a plate, a no-jet model, a lift-jet-only model and a vectored-thrust model with lift jet.  The results shown are in relative good agreement with the experimental data. However, it is indicated that a correct description of the geometry is a critical factor, and this study suggests further improvement in the coupling process is necessary to reflect strong entrainment modeling and to enhance usability.		
17. Key Words (Suggested by Author(s))  Zonal Method, ADI Parabolized Navier-Stokes Equations Elliptic Effects		18. Distribution Statement  Unclassified, Unlimited
19. Security Classification of this report Unclassified	20. Security Classification of this page Unclassified	21. No. of pages 121
		22. Price

## SUMMARY

This report summarizes work done in the Phase II project. A zonal method of iterative coupling between an inviscid code, VSAERO, and a viscous code, APPL, was employed. VSAERO, a low-order panel method, was modified to handle both an entire aircraft configuration and a jet wake/surface. APPL uses an accurate second-order, iterative, alternating-direction-implicit (ADI) algorithm to integrate the parabolized Navier-Stokes equations in a single marching pass through the domain and solves the jet region with a three-dimensional pressure equation to recover the elliptic effects. The jet model in VSAERO is refined to improve the stability of boundary relaxation and also to maintain a boundary shape. A correlation study with the available experimental data has been carried out to establish the range of validity of the method using a jet on a plate, a no-jet model, a lift-jet-only model and a vectored-thrust model with lift jet.

The results shown are in relatively good agreement with the experimental data. However, it is indicated that a correct description of the geometry is a critical factor, and this study suggests further improvement in the coupling process is necessary to reflect strong entrainment modeling and to enhance usability.

## TABLE OF CONTENTS

<u>Section No.</u>	<u>Page No.</u>
SUMMARY . . . . .	i
LIST OF FIGURES . . . . .	iv
1.0 INTRODUCTION	
1.1 General . . . . .	1
1.2 Statement of the Problem . . . . .	1
1.3 Phase II Objectives . . . . .	3
2.0 BASIC METHOD	
2.1 Inviscid Model (VSAERO) . . . . .	4
2.2 Viscous Model (APPL) . . . . .	4
2.2.1 Governing Equations . . . . .	8
2.2.2 Pressure Correction Relation . . . . .	9
2.2.3 Turbulence Model . . . . .	13
2.2.4 Numerical Method . . . . .	15
2.2.4.1 Marching Procedure . . . . .	16
2.2.4.2 Two-Dimensional Pressure Correction . . . . .	16
2.2.4.3 Boundary Conditions . . . . .	17
2.2.4.4 Numerical Damping . . . . .	18
2.2.4.5 Mesh Generation . . . . .	19
2.2.4.6 Plume Expansion and Trajectory . . . . .	19
2.3 Coupling Procedure . . . . .	21
3.0 NEW PROCEDURES	
3.1 Coupling . . . . .	24
3.2 VSAERO Modification . . . . .	27
3.3 APPL Modification . . . . .	28
4.0 RESULTS AND DISCUSSION . . . . .	31
4.1 A Jet on a Plate . . . . .	31
4.2 A No-Jet Model . . . . .	33
4.3 A Lift-Jet-Only Model . . . . .	33
4.4 A Vectored-Thrust Model with Lift Jet . . . . .	58
5.0 CONCLUSION AND RECOMMENDATIONS . . . . .	106
6.0 REFERENCES . . . . .	107

## TABLE OF CONTENTS (CONCLUDED)

<u>Section No.</u>	<u>Page No.</u>
APPENDIX: FILE MANAGEMENT	
A.1 File Communication . . . . .	110
A.2 Flow Chart . . . . .	111
A.3 File Format . . . . .	112

# LIST OF FIGURES

<u>Fig. No.</u>	<u>Title</u>	<u>Page No.</u>
1	New Jet Model	
(a)	New Jet Grid Plane Scheme . . . . .	5
(b)	Jet Reference Plane . . . . .	6
(c)	Local Coordinate System in Grid Plane . . . . .	7
2	Computational Cell Model	
(a)	Computational Cell for Continuity . . . . .	10
(b)	Indexing Convention and Location for Flow Variables . . .	11
3	Illustration of the Overlap Region in the VSAERO/APPL Coupling . . . . .	23
4	VSAERO Calculation	
(a)	Initial Model . . . . .	25
(b)	Second and Subsequent Models . . . . .	26
5	Centerline Velocity Decay for Turbulent Jet in a Coflowing Stream . . . . .	32
6	Jet at 60° Incidence	
(a)	Convergence of Jet Trajectory . . . . .	34
(b)	Streamwise Velocity Contours at Several Diameters Down- stream from Nozzle Exit . . . . .	35
(c)	Cross-Flow Velocity Vectors . . . . .	36
(d)	Convergence History (VNORM) at Y = 0.0; First and Fifth Iterations . . . . .	37
(e)	Convergence History (VNORM) at Y = 0.0; Fourth and Fifth Iterations . . . . .	38
(f)	Convergence History (VX) at Y = 0.0 . . . . .	39
(g)	Convergence History (VZ) at Y = 0.0 . . . . .	40
(h)	Symmetry in Convergence History (VNORM) at X = 3.0 . . .	41
(i)	Symmetry in Convergence History (VX) at X = 3.0 . . . .	42
(j)	Symmetry in Convergence History (VZ) at X = 3.0 . . . .	43
(k)	Boundary Condition for APPL from VSAERO (Upper VX) at Y = 0.0 . . . . .	44
(l)	Boundary Condition for APPL from VSAERO (Lower VX) at Y = 0.0 . . . . .	45
(m)	Boundary Condition for APPL from VSAERO (Upper VZ) at Y = 0.0 . . . . .	46
(n)	Boundary Condition for APPL from VSAERO (Lower VZ) at Y = 0.0 . . . . .	47
7	A V/STOL Configuration	
(a)	Lift-Jet Configuration in the V/STOL Tunnel . . . . .	48
(b)	Front Vectored-Thrust Configuration Showing each Cut on Both Wing and Fuselage Sections . . . . .	49

# LIST OF FIGURES (CONTINUED)

<u>Fig. No.</u>	<u>Title</u>	<u>Page No.</u>
8	A No-Jet-Nozzle Model	
(a)	Cp of Fuselage Bottom at Y = 0 . . . . .	50
(b)	Cp of Fuselage Bottom at Y = 1.25 . . . . .	51
(c)	Cp of Fuselage Bottom at Y = 2.0 . . . . .	52
(d)	Cp of Wing Section at Y = 5.04 . . . . .	53
(e)	Cp of Wing Section at Y = 7.79 . . . . .	54
(f)	Cp of Wing Section at Y = 10.55 . . . . .	55
(g)	Cp of Wing Section at Y = 16.05 . . . . .	56
9	Paneling of Lift-Jet Model	
(a)	Aircraft Paneling with Lift-Jet Wake . . . . .	57
(b)	Aircraft Paneling with Solid Wake-Jet Surface . . . . .	58
10	Jet-Off Case	
(a)	Cp of Fuselage Bottom at Y = 0 . . . . .	60
(b)	Cp of Fuselage Bottom at Y = 1.25 . . . . .	61
(c)	Cp of Fuselage Bottom at Y = 2.0 . . . . .	62
(d)	Cp of Wing Section at Y = 5.04 . . . . .	63
(e)	Cp of Wing Section at Y = 7.79 . . . . .	64
(f)	Cp of Wing Section at Y = 10.55 . . . . .	65
(g)	Cp of Wing Section at Y = 16.05 . . . . .	66
11	A Lift-Jet-On Case; $V_j/V_o = 4.878$	
(a)	Cp of Fuselage Bottom at Y = 0 . . . . .	67
(b)	Cp of Fuselage Bottom at Y = 1.25 . . . . .	68
(c)	Cp of Fuselage Bottom at Y = 2.0 . . . . .	69
(d)	Cp of Wing Section at Y = 5.04 . . . . .	70
(e)	Cp of Wing Section at Y = 7.79 . . . . .	71
(f)	Cp of Wing Section at Y = 10.55 . . . . .	72
(g)	Cp of Wing Section at Y = 16.05 . . . . .	73
(h)	Streamwise Velocity Contours at 90° Incidence . . . . .	74
(i)	Cross-Flow Velocity Vectors at 90° Incidence . . . . .	74
12	A Vectored-Thrust Model with Lift Jet (Dual Jet); First Iteration, $V_j/V_o = 3.354$	
(a)	Aircraft Paneling of Right-Hand Side . . . . .	76
(b)	Cp of Fuselage Bottom at Y = 0 . . . . .	77
(c)	Cp of Fuselage Bottom at Y = 1.25 . . . . .	78
(d)	Cp of Fuselage Bottom at Y = 2.0 . . . . .	79
(e)	Cp of Wing Nacelle Section at Y = 5.04 . . . . .	80
(f)	Cp of Wing Nacelle Section at Y = 7.79 . . . . .	81
(g)	Cp of Wing Section at Y = 10.55 . . . . .	82
(h)	Cp of Wing Section at Y = 16.05 . . . . .	83

# LIST OF FIGURES

<u>Fig. No.</u>	<u>Title</u>	<u>Page No.</u>
13	A Vectored-Thrust Model with Lift Jet (Dual Jet); Second Iteration	
(a)	Cp of Fuselage Bottom at Y = 0.0 . . . . .	84
(b)	Cp of Fuselage Bottom at Y = 1.25 . . . . .	85
(c)	Cp of Fuselage Bottom at Y = 2.0 . . . . .	86
(d)	Cp of Wing Nacelle Section at Y = 5.04 . . . . .	87
(e)	Cp of Wing Nacelle Section at Y = 7.79 . . . . .	88
(f)	Cp of Wing Section at Y = 10.55 . . . . .	89
(g)	Cp of Wing Section at Y = 16.05 . . . . .	90
14	Jet Trajectories	
(a)	Right-Hand Side Paneling with Dual Jet Surfaces at Second Iteration . . . . .	91
(b)	Paneling with Tightened Dual Jet Surfaces at Second Iteration . . . . .	92
15	Intersecting Jet Plumes of Both Cores and Boundaries at Third Iteration . . . . .	93
16	Development of Confluent Jet Core at Third Iteration . . . . .	94
17	Cp Distributions on the Outer Boundaries at the Third Iteration . . . . .	95
18	Vectored-Thrust Model with Lift Jet; Final Iteration	
(a)	Paneling of Aircraft with Jet Plume Surfaces . . . . .	97
(b)	Cp Distribution on Fuselage Bottom at Y = 0 . . . . .	98
(c)	Cp Distribution on Fuselage Bottom at Y = 1.25 . . . . .	99
(d)	Cp Distribution on Fuselage Bottom at Y = 2.0 . . . . .	100
(e)	Cp Distribution on Wing Nacelle Section at Y = 5.04 . . . . .	101
(f)	Cp Distribution on Wing Nacelle Section at Y = 7.79 . . . . .	102
(g)	Cp Distribution on Wing Section at Y = 10.55 . . . . .	103
(h)	Cp Distribution on Wing Section at Y = 16.05 . . . . .	104
19	Streamwise Velocity Contours for Lift Jet at 90° Incidence . . . . .	105
20	Cross-Flow Velocity Vectors for Lift Jet at 90° Incidence . . . . .	105
21	Streamwise Velocity Contours for Vectored-Thrust Jet at 90° Incidence . . . . .	106
22	Cross-Flow Velocity Vectors for Vectored-Thrust Jet at 90° Incidence . . . . .	106



## 1.0 INTRODUCTION

### 1.1 General

This is the final report on Phase II of a project aimed at improving prediction techniques for flows about V/STOL aircraft. Emphasis is placed on complex configurations with jets and control surfaces at large deflection angles. The strategy used is based on an iterative coupling between an advanced panel code, VSAERO, and a parabolized Navier-Stokes (PNS) code. VSAERO had been extended under a Phase I effort to improve the basic modeling of the jet boundaries in the presence of complex configurations. One of the aims of the present effort was to enhance and consolidate this model and to couple it with the APPL (PNS) code developed by AMTEC Engineering. Work on the latter code was aimed at incorporating elliptic terms for improved treatment of jets at large inclination to the onset flow. Treatment of three-dimensional pressure field terms is also a basic requirement for longer term objectives in the areas of jet/ground impingement and exhaust gas reingestion.

### 1.2 Statement of the Problem

Since the current trend in the design process for STOL and V/STOL aircraft requires the prediction of the effects of jet/surface interaction, a more reliable method describing the flow field around STOL and V/STOL bodies has been sought. The rising cost of wind tunnel testing, the growing capacity of high speed computers, and the development of new analytical tools has influenced this trend. Even though experiments using wind tunnel testing provide reliable results, these involve procedures which are expensive and difficult to set up, especially when a variety of design conditions are tested. Thus, at an early stage of the design process, modern designers often turn to CFD (Computational Fluid Dynamics) to obtain aerodynamic data. The modern trend towards a vectored thrust configuration which is designed to produce powered lift force during the takeoff and landing phases as well as to provide a pilot with vectored force during combat maneuver, has created a more complex environment which adds jet/surface interaction, jet-induced swirl, and jet entrainment to existing problems. The greatest impact on the airframe design is due to jet entrainment which needs to be predicted at an early stage.

The flow field around a powered lift aircraft reveals complex phenomena including vortical flows and separated flows from conventional high-lift devices caused by the high energy jet flows which may be at large deflection angles relative to the direction of vehicle motion. High nozzle pressure often causes the supersonic flow region at the initial jet plane. The aerodynamic environment associated with a jet emitting perpendicular to a flat plane in a cross flow shows that viscous forces dominate entrainment of mainstream fluid and flow separation on the downstream side of the jet initial zone.

It is well understood that only NS equations (or Reynolds-averaged Navier-Stokes (RANS) equations for turbulent flows) can handle this complex flow field. Although, in recent years, the introduction of supercomputers

has made it possible to solve the RANS equations in three-dimensional problems with some success, such solutions are restricted to local flow domains because of computing cost and huge storage requirements. Therefore, solutions of the three-dimensional RANS equations are still impractical for a complete powered lift vehicle. For computational efficiency, a zonal approach dividing the flow domain into multiple zones where each set of simplified RANS equations is solved, was pursued to attack this class of problem. This approach is called zonal, hybrid modeling, or viscous-inviscid interaction. Usually multiple zones are defined as fully viscous, inviscid rotational or inviscid irrotational. Each of the respective zones will employ a corresponding set of equations, and share its common, interdependent boundaries.

In the viscous equations, as a subset of the NS equations, the classical boundary layer equations have been very successful in practical engineering applications of problems when the Reynolds Number is high. Often coupled with an inviscid method, boundary layer methods are very useful tools in the calculation of flow fields. Since boundary layer equations are based on the assumption that the viscous layer is thin relative to the local radii of curvature of the surface, general problems usually violate this assumption and require a higher order of viscous equations. Three levels of approximations between the classical boundary layer equations and complete NS equations are commonly in use as simplified forms of RANS equations. These are a set of second-order boundary layer equations, thin-layer NS equations (TLNS) and parabolized NS equations (PNS), from which elliptic terms have been removed. The TLNS approximation which drops the diffusion terms parallel to the body surface, is quite successful in a class of flows in high-speed aerodynamics, while the PNS or partially parabolic (PPNS) approximation, neglecting only the streamwise diffusion terms, is applicable to both compressible and incompressible flow areas. A PNS procedure with space marching, subject to proper handling of streamwise pressure, is made successful when no massive separation exists.

Meanwhile, in the class of inviscid equations, the Euler full potential or potential equations are used. The Euler method has more generality than the others, because many of the major elements of fluid dynamics are incorporated in them. These govern the motion of an inviscid nonheat-conducting gas and have a different character in different flow regimes. Associated with the Euler equations are the companion set of small perturbation equations. In subsonic and supersonic flows, the Prandtl-Glauert equation is observed to provide the first-order theory for the potential function. Many different methods are used to obtain solutions to the Euler equations or any of the various reduced forms of the Euler equations. But among them, the integral method using the potential flow equation for subsonic or transonic flow with Mach number correction is much favored by industry over the finite difference method due to its computational efficiency. Flow conditions dominated by large areas of attached flow are treated with much success by this integral method, commonly called a "panel method". Several variations of this method currently exist in industry which utilize singularity distributions such as doublets, sources or vortices in the form of panels to model the desired configuration. An integral equation of the second kind can be formulated using Green's Identities to solve for the singularity distribution on the body. Typical examples of such methods applicable to subsonic flows are the Hess code (1), program VSAERO (2), and PANAIR (3), which are

all three dimensional panel methods. A comprehensive review among subsonic panel methods available as production codes which was made by Margason et al. (4), indicated that there is a trade-off between the increased accuracy attainable with the higher-order methods for a given number of panels, and the significantly greater cost and execution time required for their implementation. These methods are applicable to subsonic flows while recent success in the transonic regime has been achieved by Boppe (5).

Roberts (6) coupled a PNS solution for the jet with a surface singularity panel method for the aircraft configuration. In the present STOL or V/STOL configurations, the vertical jet in strong cross flow creates a situation which may not be appropriately modeled by a PNS method alone, so that it may become necessary to restore the RANS equations or to provide a means (such as the elliptic pressure equation) to restore ellipticity. A strong interaction between the jet and airframe requires many iterations to complete the interaction, unless the RANS-only solutions are pursued for a flow domain large enough to impose a free stream condition at the boundary. In this regard, the panel method for inviscid calculation can substantially reduce the computing time involved in iterations by an improved jet modeling technique and an efficient coupling technique.

The general configuration modeling program, VSAERO (2), (7), was first extended for powered lift applications under NASA Contract NAS2-11169 with very encouraging results (8). The basic formulation of the method assumes that regions dominated by viscous effects are confined to thin boundary layers on the attached flow regions of the vehicle surface and to thin free shear layers representing jet "boundaries" and wakes. The problem is thereby reduced to one of free vortex sheets embedded in a potential flow about the vehicle. The method includes an inner iterative "wake relaxation" loop to compute the strength and location of free vortex sheets representing jet and wake boundaries (9), (10). The computing effort for these calculations is very reasonable and very complicated configurations have been analyzed with the method (7).

The present approach, therefore, employs the zonal method using the VSAERO code modified to include the full aircraft configuration with a large jet deflection angle, and the APPL code with the elliptic pressure equation.

### 1.3 Phase II Objectives

There are three major objectives in the present Phase II effort.

- (1) Improve the jet model further using a coupled PNS zonal method. The scope of this investigation is directed towards better entrainment modeling for treatment of large jet deflection angles and strong jet surface interaction with a longer term view towards problems of jet/ground impingement.
- (2) Correlate the coupled PNS zonal method with available experimental data to establish the range of validity of the method.
- (3) Evaluate the handling of computed results with a view to improved presentation of calculated results and visual display.

## 2.0 BASIC METHOD

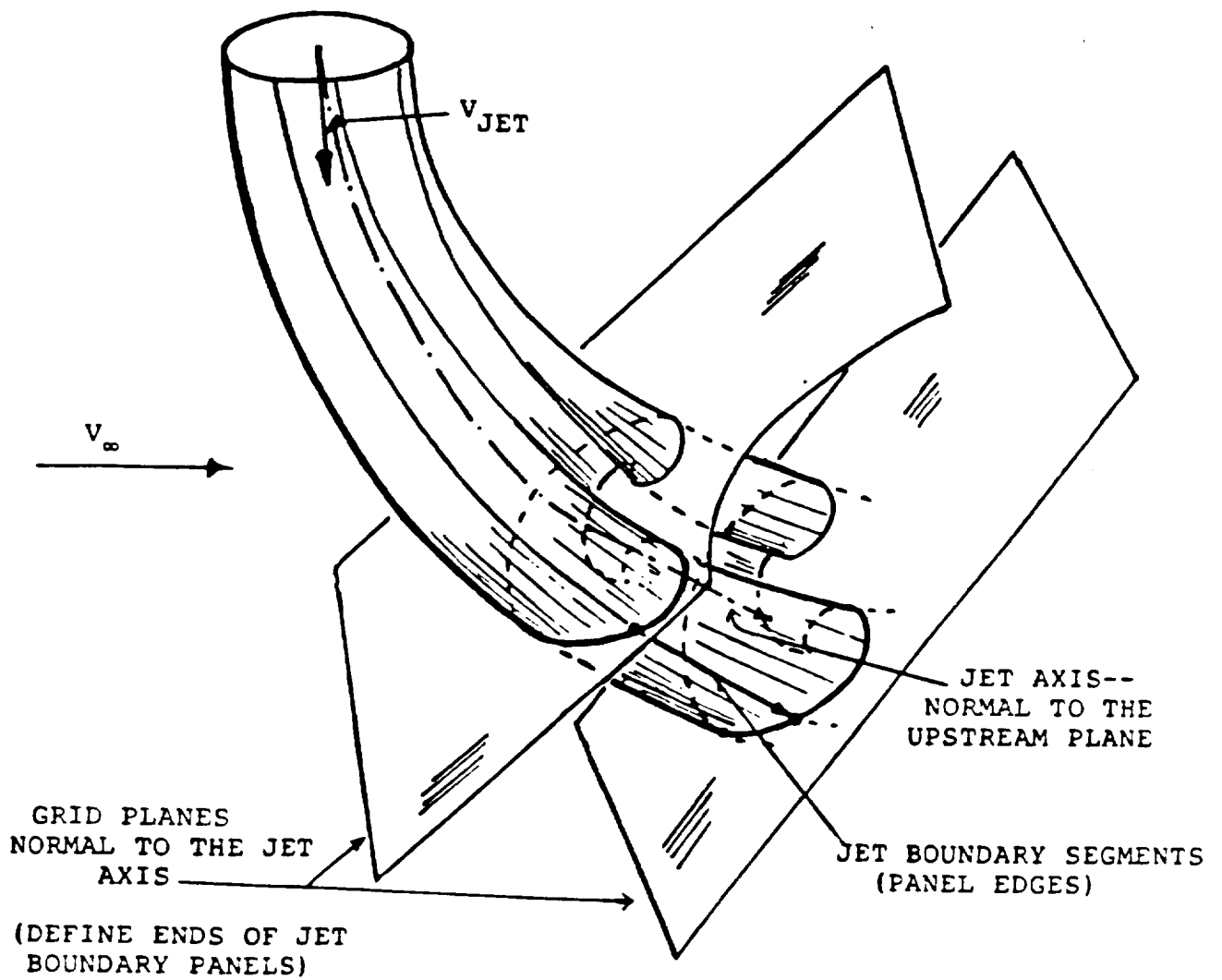
### 2.1 Inviscid Model (VSAERO)

The VSAERO program (2) is a surface singularity panel method employing quadrilateral panels of uniform source and doublet. The source values are set by the external Neumann boundary condition of nonzero normal velocity representing boundary layer growth; the doublet values are solved after applying the Dirichlet boundary condition of zero perturbation potential at an internal control point at the center of each panel. The method includes a coupled iterative calculation for viscous effects using integral boundary layer methods and an inner iterative "wake relaxation" loop to compute the strength and location of free vortex sheets representing the jet and wake boundaries (9), (10).

Under earlier contracts (NAS2-11169 and NAS2-11727), the basic capabilities of VSAERO, i.e., its capacity to deal with arbitrary shapes, its coupled iterative schemes for wake relaxation and boundary layer effects, and also its simple vortex tube modeling of jet boundaries, had been evaluated on a number of VSTOL configurations (8). During these evaluations, certain deficiencies in the jet model were identified: these relate to the modeling of entrainment and to the jet boundary relaxation when treating large jet deflection angles. Under a Phase I SBIR contract a new jet model was installed to alleviate these difficulties (11). This new jet model uses a set of grid planes constructed normal to the local jet axis shown in Figure 1(a) and the jet reference plane contains the initial jet velocity vector,  $V_{jet}$ , constructed normal to the jet exit plane, Figure 1(b). Also, a local coordinate system is generated within each grid plane, Figure 1(c). In this scheme relaxation calculations proceed along the jet axis in a series of steps as before, but now a normal grid plane is constructed at each step. The first pass of the trajectory geometry is generated using Margason's equation (12). The work under Contract NAS2-11944 was partly concerned with evaluating the new model for the jets issuing at 90° to the onset flow (13). The scope of this evaluation covered the relaxation of the jet boundaries, simple modeling of entrainment, and the effects of the boundary layer on the surface through which the jet issues. The jet model is basically similar to that of Shollenberger (14) except that here panels representing the jet boundaries have a linear doublet distribution (i.e., constant vorticity) in the local streamwise direction.

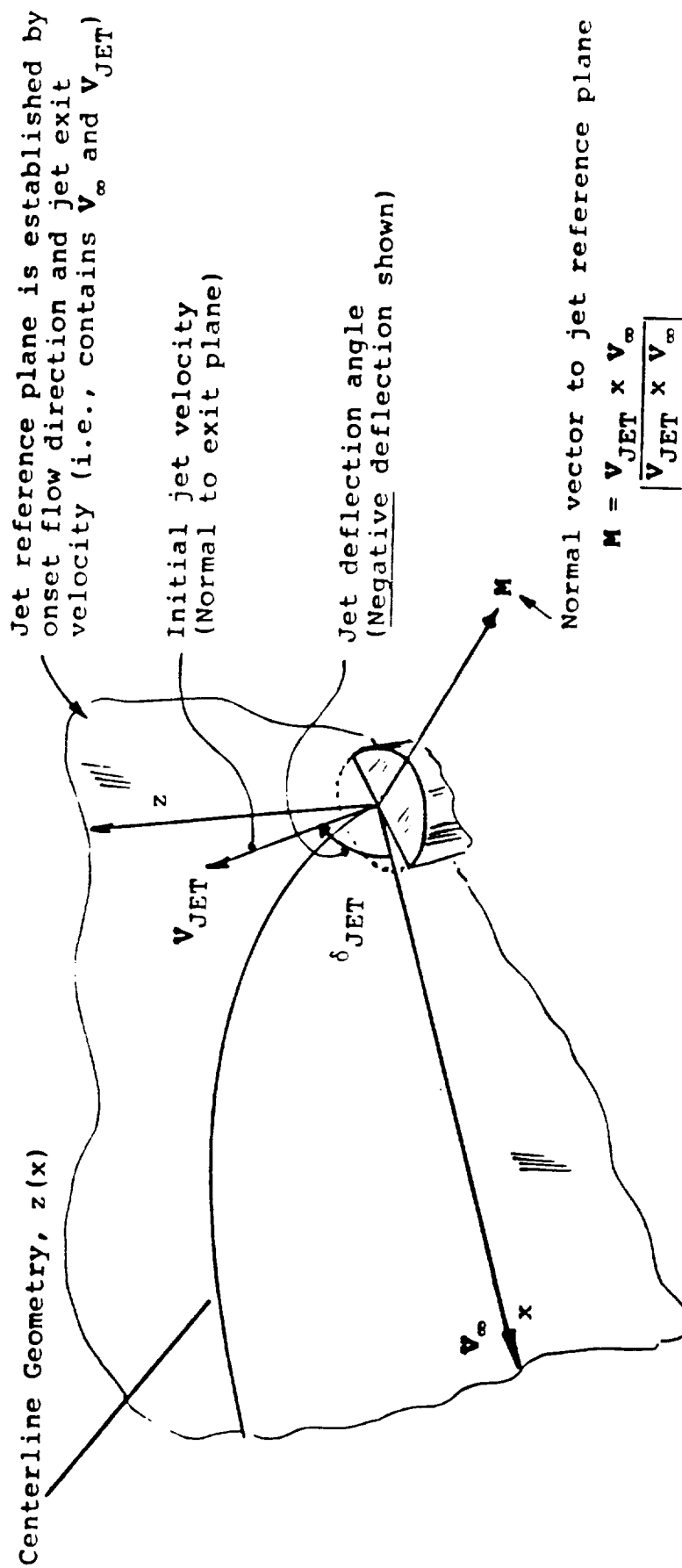
### 2.2 Viscous Model (APPL)

A PNS code (6), APPL, developed by AMTEC Engineering for a particular class of three-dimensional compressible viscous flows, was applied to the calculation of the jet flow field. A parabolic assumption was made that the flow has a predominant flow direction along which the viscous and turbulent diffusion may be neglected and no massive separation occurs. This neglect of elliptic terms along the flow direction enables a PNS code to march downstream. Numerous internal and external flows ranging from complex three-dimensional flows to three-dimensional jets mixing with the free stream are known to be parabolic. The RANS equations with suitable closure for turbulent flows are acknowledged as being sufficient for analyzing complex viscous flow fields. When the parabolic approximations are implemented, the



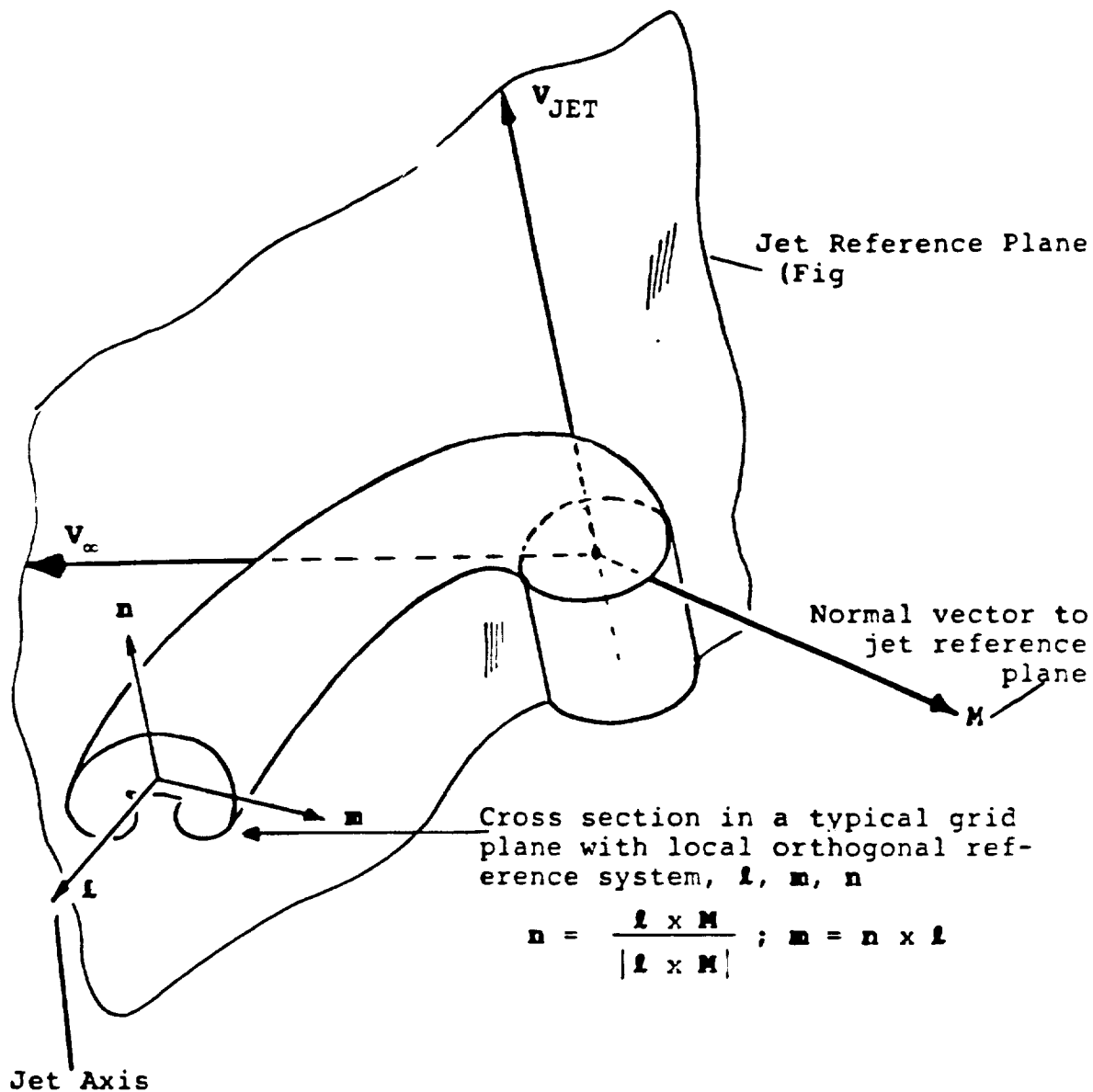
(a) New Jet Grid Plane Scheme

Figure 1. New Jet Model.



(b) Jet Reference Plane

Figure 1. Continued.



(General case shown, i.e., jet is deflected out of its reference plane by interaction with vehicle surface, etc.)

(c) Local Coordinate System in Grid Plane

Figure 1. Concluded.

resulting equations are simplified for practical solution in a design oriented computer program. The streamwise pressure gradient is assumed to be uniform at each cross-sectional station. In the PNS code a simple marching solution procedure was implemented which eliminates the communication with the downstream flow while marching the PNS equations.

This code uses a two-equation turbulence model with compressibility and axisymmetric flow corrections for the purpose of closure. The governing equations are transformed into a boundary fitted coordinate system. A marching technique is used and pressure is solved for at each plane. Boundary conditions are explicitly provided for by an external source which is updated during coupling with an inviscid code.

### 2.2.1 Governing Equations

The governing equations that are modeled in the APPL code are the steady three-dimensional compressible parabolized Navier-Stokes equations. In a general non-orthogonal coordinate system these equations can be written as

$$\begin{aligned}
 (\rho U J^{-1})_{\xi} + (\rho V J^{-1})_{\eta} + (\rho W J^{-1})_{\sigma} &= 0 \\
 \rho U u_{\xi} + \rho V u_{\eta} + \rho W u_{\sigma} &= -(P_{\xi} \xi_x + P_{\eta} \eta_x + P_{\sigma} \sigma_x) + DT_u \\
 \rho U v_{\xi} + \rho V v_{\eta} + \rho W v_{\sigma} &= -(P_{\xi} \xi_y + P_{\eta} \eta_y + P_{\sigma} \sigma_y) + DT_v \\
 \rho U w_{\xi} + \rho V w_{\eta} + \rho W w_{\sigma} &= -(P_{\xi} \xi_z + P_{\eta} \eta_z + P_{\sigma} \sigma_z) + DT_w \\
 \rho U (C_p T)_{\xi} + \rho V (C_p T)_{\eta} + \rho W (C_p T)_{\sigma} &= \nabla \cdot (k \nabla T) + \nabla \cdot (\mu \nabla Q) - (\rho U Q_{\xi} + \rho V Q_{\eta} + \rho W Q_{\sigma})
 \end{aligned}$$

where

$$\begin{aligned}
 Q &= \frac{1}{2}(u^2 + v^2 + w^2) \\
 \rho &= \rho(P, T)
 \end{aligned}$$

u, v, and w are the Cartesian velocity components. The quantities, U, V, and W, are the contravariant velocity components in the  $\xi, \eta, \sigma$  coordinate system defined by

$$\begin{aligned}
 U &= \xi_x u + \xi_y v + \xi_z w \\
 V &= \eta_x u + \eta_y v + \eta_z w \\
 W &= \sigma_x u + \sigma_y v + \sigma_z w
 \end{aligned}$$



The quantities,  $\xi_x, \xi_y, \dots, \sigma_z$ , are the components of the metric tensor for the general non-orthogonal coordinate system. The DT terms which appear in the momentum and energy equations are the diffusion terms. Diffusion in the streamwise,  $\xi$ , direction has been neglected, giving the diffusion terms a parabolic character.

For laminar flows the viscosity is calculated using Sutherland's relation. A two-equation turbulence model (Section 2.2.3) is used to calculate the eddy viscosity for turbulent flows.

For supersonic flows, the set of equations is hyperbolic and the domain of dependence at any location lies upstream. Thus, the equations may be numerically integrated by efficient spatial marching.

For subsonic flows (or subsonic regions in the flow field) the set of equations is elliptic, and the flow upstream is affected by downstream conditions. Thus, hyperbolic spatial marching is not suitable for strictly accurate modeling. By imposing an external pressure field, the streamwise pressure gradient becomes a known quantity. This removes the source of upstream influence and makes the equations parabolic. The solution can then be obtained by using the marching procedure. For jet flows the imposed pressure is obtained from the local free stream. This pressure field can only be imposed in subsonic regions. Therefore, in supersonic regions the local calculated pressure is used in the streamwise pressure gradient. In the solution procedure the local Mach number is inspected before the streamwise pressure gradient is calculated.

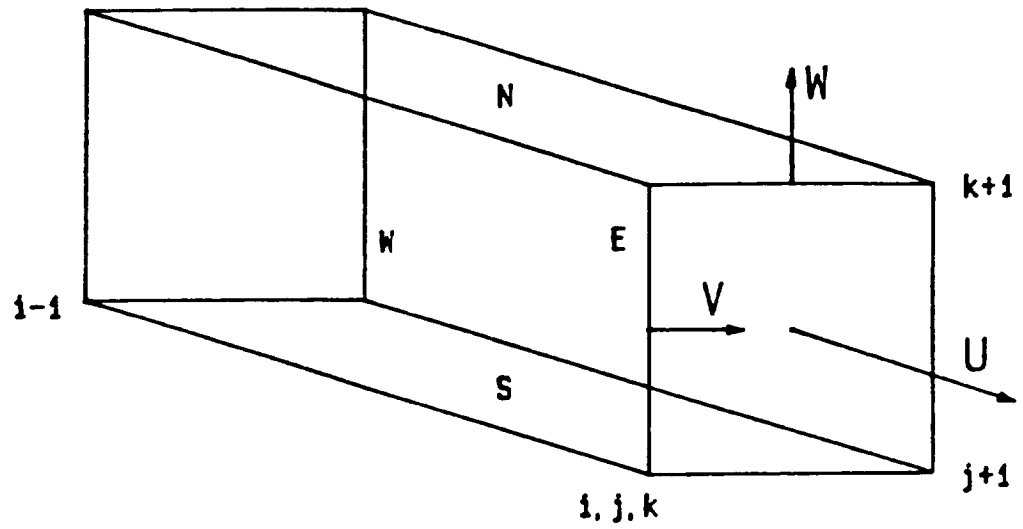
For jets with substantial streamwise curvature, elliptic effects need to be considered. The elliptic effects in the streamwise direction are only transmitted through the pressure field, which results in this type of flow being classified as partially parabolic. Since the pressure field is implicitly governed by the continuity equation, it is possible to couple the momentum and energy equations to a pressure relation in which the local continuity error is used to force a correction on pressure. The derivation of this relationship, although conceptually simple, is tedious algebraically. The important steps in the development of this key relationship are summarized in the next section.

### 2.2.2 Pressure Correction Relation

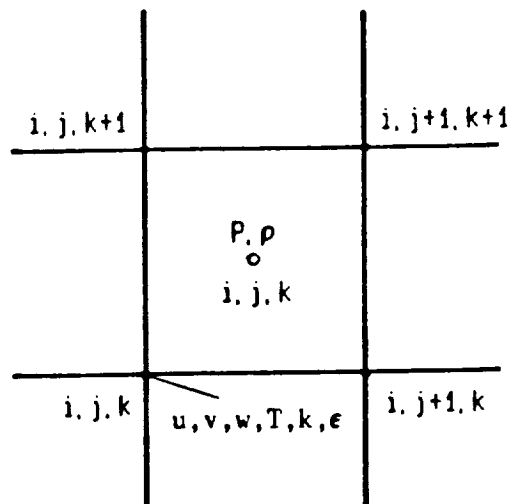
The elliptic pressure correction relation is derived from the discrete forms of the continuity and momentum equations based on the effects of a pressure perturbation,  $P'$ , on the mass balance of a computational cell.

Considering the cell shown in Figure 2, the continuity equation is written as

$$-(\rho VA)_D + (\rho VA)_U + (\rho VA)_W - (\rho VA)_E + (\rho VA)_S - (\rho VA)_N = 0 \quad (1)$$



(a) Computational Cell for Continuity



(b) Indexing Convention and Location for Flow Variables

Figure 2. Computational Cell Model.

where  $\rho$ ,  $V$ , and  $A$  are density, velocity and area, respectively. The subscripts, U, D, E, W, N, and S, refer to quantities on the upstream, downstream, east, west, north, and south faces of the cell. On streamwise faces the densities are the same as cell densities, that is,

$$\rho_D = \rho_{ijk}; \quad \rho'_D = \rho'_{ijk}$$

On the other surfaces, the densities are the averages of the neighboring cells. On the west surface, for example, the density is

$$\rho_W = 1/2 (\rho_{ijk} + \rho_{ij-1k})$$

and

$$\rho'_W = 1/2 (\rho'_{ijk} + \rho'_{ij+k})$$

The ' indicates the change in the quantity due to  $P'$  in the  $i,j,k$  cell.

A pressure perturbation in a cell affects continuity for that cell primarily through its effect on density and velocity. Thus, the local density and velocities respond to a correction to the cell pressure. If the pressure field is three-dimensionally elliptic, the pressure correction has an upstream influence. For strictly PNS flows, the influence can only be elliptic in the cross-stream directions.

The perturbation to the density in a cell is assumed to be isentropically related to the pressure correction for that cell by

$$\rho' = P'/C^2 \quad (2)$$

where  $C$  is the isentropic speed of sound.

The perturbations of the Cartesian velocity components are related to the pressure perturbation through the momentum equation. By neglecting the diffusion and cross-stream convection terms, the perturbation momentum equation takes the form

$$u'_{ijk} = - \frac{[\frac{1}{4}\xi_x + \frac{1}{2}\eta_x + \frac{1}{2}\sigma_x]_{ijk}}{(\rho U)_{ijk}} P'_{ijk} \quad (3)$$

The perturbation of the velocity normal to a surface is calculated from the Cartesian velocity vector and the projection relation. For the streamwise face this takes the form

$$V_D = U_{AVE} * n_1 + V_{AVE} * n_2 + W_{AVE} * n_3$$

where  $n_1$ ,  $n_2$ , and  $n_3$  are the components of the unit normal vector in the  $x$ ,  $y$ , and  $z$  directions, and the subscript, AVE, indicates an average of the corner point values.  $U_{AVE}$ , for example, is

$$U_{AVE} = 1/4 (u_{ijk} + u_{ij+1k} + u_{ijk+1} + u_{ij+1k+1})$$

The corrected density and velocity components have the form

$$\rho = \tilde{\rho} + \rho'$$

$$u = \tilde{u} + u'$$

$$v = \tilde{v} + v'$$

$$w = \tilde{w} + w'$$

where the  $\sim$  represents the old values. Substituting these relations into Eq. (1), using Eqs. (2) and (3) to replace the  $'$  quantities, and neglecting higher-order terms, the following relation for the pressure correction on a given cell is derived.

$$P' = \frac{CON}{MET - DIV/C^2}$$

CON is the continuity error for the  $ijk$  cell based on the current values of density and velocity. Clearly, the continuity error is the driving force that leads to pressure corrections. As the local continuity error approaches zero, so does the pressure correction. MET is a collection of terms that influence continuity through the velocity perturbation. DIV is a collection of terms that influence continuity through density perturbations. One can observe that the denominator has the potential to approach zero, particularly when compressibility is substantial. Since this introduces a source of stiffness to the equations, an under-relaxation coefficient is required in the pressure correction relation.

This derivation of the pressure correction relation is only applicable to a PNS method since it has no upstream influence. However, the extension of this approach to three dimensions is straightforward in the PNS/EP method.

### 2.2.3 Turbulence Model

For turbulent flow the Reynolds-averaged Navier-Stokes (RANS) equations include additional stress terms resulting from the averaging of the unsteady fluctuations in the velocity field. These Reynolds stresses are usually modeled using the Boussinesq approximation in which the stress is replaced by a turbulent eddy viscosity,  $\mu_t$ , times a velocity gradient. The Reynolds stresses are then analogous to the existing stresses for laminar flows. Therefore, for turbulent flows, one simply replaces the viscosity in the diffusion terms with an effective viscosity.

$$\mu_e = \mu + \mu_t$$

An appropriate turbulence model is incorporated into the flow analysis in order to calculate  $\mu_t$ . A fairly general model is the two-equation model developed by Launder and Spalding (15). It is used in the present analysis since it has been reasonably reliable for a wide range of flows.

The two-equation model involves additional differential equations for the transport of the turbulence energy,  $k$ , and the turbulence energy dissipation rate,  $\epsilon$ .

$$\rho U k_{\xi} + \rho V k_{\eta} + \rho W k_{\sigma} = DT_k + S_k \quad (4)$$

$$\rho U \epsilon_{\xi} + \rho V \epsilon_{\eta} + \rho W \epsilon_{\sigma} = DT_{\epsilon} + S_{\epsilon} \quad (5)$$

where the diffusion terms are represented again by  $DT$ , and the source terms are given by

$$S_k = \mu_t ST - \rho \epsilon$$

$$S_{\epsilon} = C_1 \mu_t \frac{\epsilon}{k} ST - C_2 \rho \frac{\epsilon^2}{k}$$

In Cartesian coordinates,  $ST$  is

$$ST = \left( \frac{\partial u_i}{\partial x_k} + \frac{\partial u_k}{\partial x_i} \right) \frac{\partial u_i}{\partial x_k} \\ = 2 \left( u_x^2 + v_y^2 + w_z^2 \right) + \left( u_y + v_x \right)^2 + \left( w_y + v_z \right)^2 + \left( u_z + w_x \right)^2$$

which transforms to the  $\xi, \eta, \sigma$  system using the standard transformation relations.

The source terms include production and dissipation terms. The dissipation terms require special consideration since a marching step size limitation could occur as a result of the minus sign. This is evident by examining the  $k$ -equation (Eq. (4)), and neglecting all terms except streamwise convection and the dissipation term,

$$\rho U k_{\xi} = -\rho \epsilon$$

In differenced form this becomes

$$k_{ijk} = k_{i-1jk} - \frac{\epsilon_{ijk}}{\rho U_{ijk}}$$

Clearly, a situation could evolve in which  $k$  is driven negative, which is non-physical. This possibility is removed by linearizing the dissipation term to make it implicit. Laminarization leads to

$$\epsilon_{ijk} = \left( \epsilon/k \right)_{ijk} k_{ijk}$$

where  $\epsilon/k$  is evaluated using the most recent values. Since the dissipation term is now based on  $k_{ijk}$ , it can be moved to the left side of the differenced equation to yield,

$$\left( \rho U_{ijk} + \frac{\epsilon_{ijk}}{k_{ijk}} \right) k_{ijk} = \rho U_{ijk} k_{i-1jk}$$

A similar approach is followed for the dissipation term in the  $\epsilon$ -equation, Eq. (5).

The  $k$  and  $\epsilon$  equations are solved using the ADI algorithm. the eddy viscosity is then calculated from

$$\mu_t = \rho C_{\mu} (k^2/\epsilon)$$

where  $C_{\mu} = 0.09$ .

#### 2.2.4 Numerical Method

The flow region is divided into a series of mesh planes in the streamwise direction. As a result of the transformation to a body-fitted coordinate system these planes can in general be rotated to remain normal to the dominant jet flow direction. This is important in flow situations where the dominant flow direction (along which the diffusion terms are neglected) is not parallel to one of the Cartesian coordinates. Hence, a deflected jet may be modeled with a nearly orthogonal mesh.

A staggered mesh is used to discretize flow field at each plane. Pressure and density are located at the center of the cell. Velocity and temperature are defined at the nodes (Figure 2(b)).

The governing equations are discretized using first-order upwind differences for derivatives in the streamwise direction. The  $\eta$  and  $\sigma$  derivatives are discretized using central differences.

The differenced form of the governing equations is marched by an ADI method summarized in Section 2.2.4. Updates to the three Cartesian velocity components and temperature are obtained from the discrete form of the momentum and energy equations. The resulting velocity field will not initially satisfy continuity since the density and pressure have not been updated. The local continuity errors are then used to drive the pressure correction relation. The pressure correction procedure uses a relaxation scheme to iteratively calculate  $P'$  and update  $u$ ,  $v$ ,  $w$ ,  $\rho$ ,  $P$ , and  $T$ . After these updates the continuity error is recalculated to begin the next iteration. The iteration continues until continuity is satisfied. This also provides an implicit pressure field for the next iteration of the governing equations. Corrections to the density and velocity fields are made using Eqs. (2) and (3). The corrections to temperature are included by assuming that the local temperature remains constant during the pressure correction procedure. The marching of the momentum and energy equations and the pressure correction relation are coupled by iterating the solution at each plane. This iterative coupling captures the cross-flow elliptic effects in the PNS mode (single marching pass).

In the PNS/EP mode (PNS coupled to the three-dimensional elliptic pressure relation) the solution is initialized by marching through the domain in the PNS mode. The three-dimensional pressure field from this pass is saved as the initial guess for the PNS/EP mode. The solution is then marched with the streamwise pressure gradient discretized using forward differencing to allow an upstream influence. During the marching pass the two-dimensional pressure correction procedure is not used. The continuity errors that result become source terms in the three-dimensional pressure relation. The three-dimensional pressure correction procedure solves the elliptic equation set and updates the pressure field. This sequence of marching through the flow domain followed by an update of the three-dimensional pressure field is iterated until continuity is satisfied.

#### 2.2.4.1 Marching Procedure

An Alternating Direction Implicit (ADI) method is used in marching the momentum and energy equations. In this method the two-dimensional step is factored into two one-dimensional steps, with the formal accuracy unaltered. Each of the one-dimensional steps constitutes a tridiagonal inversion which is simple and efficient. For a variable  $\phi$ , the two steps are:

k-implicit

$$\begin{aligned} & \phi_{ijk}^*(\rho U)_{ijk} + \frac{1}{2}\phi_{ijk+1}^*(\rho W)_{ijk} + \frac{1}{2}\phi_{ijk-1}^*(-\rho W)_{ijk} \\ & = \phi_{i-1jk}(\rho U)_{ijk} - \frac{1}{2}\tilde{\phi}_{i-1j+1k}(\rho V)_{ijk} - \frac{1}{2}\tilde{\phi}_{i-1j-1k}(-\rho V)_{ijk} - PGRAD + DT_{\phi,ijk} \end{aligned}$$

j-implicit

$$\begin{aligned} & \phi_{ijk}(\rho U)_{ijk} + \frac{1}{2}\phi_{ij+1k}(\rho V)_{ijk} + \frac{1}{2}\phi_{ijk-1k}(-\rho V)_{ijk} \\ & = \phi_{ijk}^*(\rho U)_{ijk} + \frac{1}{2}\tilde{\phi}_{i-1j+1k}(\rho V)_{ijk} + \frac{1}{2}\tilde{\phi}_{i-1j-1k}(-\rho V)_{ijk} \end{aligned}$$

The term, PGRAD, represents the pressure gradients in the momentum equations

#### 2.2.4.2 Two-Dimensional Pressure Correction

In the derivation of the pressure correction relation in Section 2.2.2 the velocity perturbations at the cell corners were related only to the pressure perturbation in the cell for simplicity. An efficient line relaxation solution procedure may be implemented when the pressure perturbations in the neighboring cells are included in the perturbation relation. The effect of neighboring cell pressure perturbations on a local velocity perturbation takes the form

$$\begin{aligned} u'_{ijk} = & -\frac{1}{(\rho U)_{ijk}} \left[ \frac{1}{4}\xi_x(P'_{ijk} + P'_{ij-1k} + P'_{ijk-1} + P'_{ij-1k-1}) \right. \\ & + \frac{1}{2}\eta_x(P'_{ijk} + P'_{ijk-1} - P'_{ij-1k} - P'_{ij-1k-1}) \\ & \left. + \frac{1}{2}\sigma_x(P'_{ijk} + P'_{ij-1k} - P'_{ijk-1} - P'_{ij-1k-1}) \right] \end{aligned}$$

The resulting pressure correction equation then becomes:



$$AP'_{ijk} + BP'_{ijk-1} + CP'_{ijk+1} + DP'_{ij-1k} + EP'_{ij-1k-1} + FP'_{ij-1k+1} \\ + GP'_{ij+1k} + HP'_{ij+1k-1} + IP'_{ij+1k+1} = CONT_{ijk}$$

where the coefficients A-J include the effects of pressure perturbations on continuity through density and velocity perturbations.  $CONT_{ijk}$  is the continuity error for cell  $ijk$ .

An iterative line relaxation method is employed to find the solution to the system of equations. This method consists of two steps that treat the correction along one of the directions implicitly and the other known direction as calculated from the previous iteration level. In this case the step would be:

k-implicit

$$AP'_{ijk} + BP'_{ijk-1} + CP'_{ijk+1} = CONT_{ijk} \\ -(DP'_{ij-1k} + GP'_{ij+1k}) \\ -(EP'_{ij-1k-1} + FP'_{ij-1k+1}) \\ + HP'_{ij+1k-1} + IP'_{ij+1k+1}$$

j-implicit

$$AP'_{ijk} + DP'_{ij-1k} + GP'_{ij+1k} = CONT_{ijk} \\ -(BP'_{ijk} + CP'_{ijk+1}) \\ -(EP'_{ij-1k} + FP'_{ij-1k+1}) \\ + HP'_{ij+1k-1} + IP'_{ij+1k+1}$$

#### 2.2.4.3 Boundary Conditions

The marching solution procedure in APPL requires an initial plane for which the flow field is completely known. Typically, this plane is coincident with the nozzle exit plane. APPL will generate an initial solution plane, or it may be supplied from some other source. The free stream portion of the initial plane is obtained from VSAERO when the coupling option is activated.

The only boundary conditions that need to be supplied to APPL are the free stream or external flow field properties on the outer boundary. For a supersonic external flow velocity, temperature, and pressure are fixed at the boundary to define the flow. When the external flow is subsonic, the total pressure and total temperature at the boundary points are assumed to be constant at the free stream values. Therefore, only the velocity components need to be specified along the boundary. Entrainment is allowed for

subsonic boundaries. This is accomplished by adjusting the normal velocity component at the boundary in response to pressure perturbations.

#### 2.2.4.4 Numerical Damping

Differencing schemes that are second or higher order are susceptible to the occurrence of computational noise, the non-physical oscillations or wiggles in the numerical solution of the field variables. The convection terms, which are centrally differenced, are the source of this noise. Therefore, when the diffusion terms dominate, noise is not a problem. This is often not the case for high Reynolds number flows since the physical viscosity and the artificial viscosity inherent to the differencing scheme are not sufficient to maintain a noise-free solution. In these situations additional numerical damping terms are required to provide smoothing. Since the differencing scheme incorporated in APPL is second order for the cross stream convection terms, a standard method for adding numerical smoothing has been included to control noise.

A reasonable choice for a damping term is another diffusion term in which the viscosity has been adjusted to prevent noise. Similarly, the physical viscosity in the existing diffusion terms can be incremented by an artificial viscosity. This allows the artificial viscosity to be included in the implicit part of the algorithm. The artificial viscosity needs to be scaled such that it is only significant where it is needed. Since changes in gradients are associated with noise generation, a scaling function based on the second difference of a field variable such as pressure or velocity is qualitatively a good choice. Using pressure the scaled artificial viscosity in the  $\eta$ -direction is

$$\mu_{\alpha} = A_{\mu} \frac{P_{j+1k} - 2P_{jk} + P_{j-1k}}{\bar{P}}$$

where  $\bar{P}$  is the average of the three pressures and  $A_{\mu}$  is an input coefficient that needs to be turned to the particular flow field. A similar expression is used for the  $\sigma$ -direction. Then the effective viscosity is

$$\mu_e = \mu + \mu_{\alpha}$$

The APPL code includes the option of basing this damping term on pressure or velocity.

An option feature has been included in APPL to provide damping. First order upwind differencing tends to smooth steep gradients. By weighting the differencing scheme of the convection terms between upwind and central, this smoothing effect can be used to control noise. The weighting used in APPL is designed to maximize the upwinding where second derivatives are the largest. The minimum and maximum levels of upwinding are user controlled.

#### 2.2.4.5 Mesh Generation

To simplify the use of the APPL code a mesh generator has been included such that just a few parameters can be specified to create a mesh that evolves as the solution is marched downstream. The mesh generator is relatively simple. The center point and radius of the circular boundary are specified by routines that monitor the position and growth of the plume. The circle is oriented to be perpendicular to the plume centerline trajectory. The outer boundary mesh points are spaced at equal angle increments along the circumference of the circle. The  $j=2$  and  $j=MAX$  points are coincident as are the points at  $j=1$  and  $j=MAX-1$ . This forms a periodic boundary. Alternatively, the outer boundary points from a previous run can be used when coupling with VSAERO. The interior mesh points are generated along straight lines connecting the center point ( $k=1$ ) to the outer boundary points ( $k=KMAX$ ). Stretching is used to concentrate the mesh near a particular region. The mesh stretching is based on a geometric progression in which the spacing between points grows by a constant factor.

The stretch factor is linearly decreased from an initial value to approach unity at a specified station. This forces the mesh to redistribute as the plume develops downstream. Initially, the gradients in the plume are likely to be large near the plume edge. Mesh stretching is required to provide a fine mesh in that region without the use of an excessively large number of mesh points. As the plume develops the gradients diminish and spread. By forcing the stretch factor to unity, a uniformly distributed mesh is generated, which more adequately resolves the flow field. The change in the stretch factor occurs smoothly to avoid any sudden distortions in the mesh from plane to plane.

#### 2.2.4.6 Plume Expansion and Trajectory

The spreading and trajectory of the plume are strongly influenced by the local surrounding flow field. Generating a mesh that encompasses the plume requires information about its position and rate of expansion. Since this cannot be accurately known a priori, the code obtains the information by monitoring the plume solution. To satisfy this requirement routines have been incorporated to determine the trajectory of the plume and to track the edge of the plume.

APPL has two options for determining the plume trajectory. The first method is based on the empirical relation developed by Margason (12) for jets deflected at large angles relative to the free stream.

$$\frac{r}{D} = -\frac{V_c^2}{4\sin^2\alpha_j} \left(\frac{z}{D}\right)^3 - \frac{z}{D} \cot\alpha_j,$$

where

$D$  - Initial jet diameter

$\alpha_j$  - Jet deflection angle below the x-y plane

$V_e$  - Effective velocity ratio,  $\sqrt{\frac{\rho_\infty V_\infty^2}{\rho_j V_j^2}}$

$V_\infty$  - Free stream velocity

$V_j$  - Initial jet velocity

This relation is used to calculate the path that is followed by the centerline of the jet. Before a step is taken to the next solution plane, the step size is determined, and the trajectory relation is solved iteratively to obtain values of  $x$  and  $z$  that simultaneously satisfy the step size. By knowing the upstream and downstream centerline positions, the local angle of the centerline trajectory can be calculated. This information is then used to orient the downstream plane which is forced to be perpendicular to the centerline.

The second method for calculating the trajectory is based on monitoring the plume solution at each plane. The set of points obtained by locating the point of maximum vorticity along each mesh ray is assumed to circumscribe the plume shear layer. The center of this set of points approximates the center of the plume. The goal of the method is to position the center of the mesh at that point. This prevents the plume from getting close to the boundary mesh. At each new plane the mesh center is obtained by extrapolating from the plume centers of the two previous planes. While this will not hit the exact center of the plume at the new plane, the method is self-correcting and tends to closely track the actual plume trajectory.

The rate at which the mesh expands for each downstream plane is determined by the development of the plume. As the plume grows the mesh expands to contain the viscous effects within its boundaries. By controlling the mesh to only expand with the plume, the available mesh is used more efficiently. The development of the plume is monitored by tracking the plume edge. Since the external flow is irrotational by definition, the edge of the plume is the point at which the vorticity reaches zero or some specified limit. The vorticity reaches a maximum in the plume shear layer and decreases rapidly as the edge is approached. The total vorticity magnitude is calculated at each mesh point from

$$\omega = [(w_y - v_z)^2 + (u_z - w_x)^2 + (v_x - u_y)^2]^{1/2}$$

The condition for allowing the mesh to expand occurs when the vorticity at any mesh point next to a user defined mesh ring is greater than ten percent of the maximum value of vorticity. This limit is somewhat arbitrary, but it has been found to be reasonably effective. When the mesh does expand, the rate of expansion is determined by input parameters. These expansion factors specify the slope of the mesh boundary relative to the plume centerline. Three factors can be specified to allow the mesh to expand at different rates as the solution is marched downstream.

The choice of expansion factors can influence the accuracy of the solution. A large factor would result in occasional sudden expansions of the mesh. This can have a non-physical effect on the solution. It can generate noise and cause an instability. When coupling with VSAERO, abrupt expansions of the plume mesh may diminish the accuracy of the VSAERO solution and reduce the chances for convergence of the coupled analysis. An optimal expansion factor would allow the mesh to grow continuously and smoothly while maintaining a sufficient clearance between the edge of the plume and the outer boundary.

### 2.3 Coupling Procedure

The interactions between the jet plume and the surrounding flow field are simulated by the coupling of the component analyses. It is not sufficient to run each code once in its separate zone. The code must interact in such a manner that the solution for the entire field is convergent and unique within the limits allowed by the algebra incorporated in the codes. Each code must provide information to the other code that adequately describes the physical processes being modeled in that zone. The PNS code, which calculates the jet plume development, must provide VSAERO with the effects of entrainment at the plume boundary. VSAERO must use this information and other aerodynamic effects of the aircraft to calculate the potential flow field and in turn provide boundary conditions for the PNS code. The basic procedure developed for coupling VSAERO and APPL is discussed below.

The domain in which the flow field is to be calculated is divided into computational zones for the individual codes. The inviscid zone is oriented to include all regions which can be adequately modeled by the VSAERO potential flow solution. The viscous zone is positioned to surround the jet plume where the viscous interactions are predicted by the PNS code. The location of the boundaries for these zones is a significant aspect of the coupling procedure.

Abutting the zones such that the boundaries are coincident does not provide the necessary flow of information for a convergent coupled analysis. Since both codes, in effect, solve boundary value problems, a specification of boundary conditions on coincident boundaries would lead to unique solutions in each zone that are functions of those boundary conditions. Unless a prior knowledge of flow properties on the boundaries was available, the flow predicted in each zone would not necessarily bear any resemblance to the physical flow. New information that could be used to update boundary conditions would not be available since the solutions are dependent upon

boundary condition and their boundary conditions are identical. Iteration is useless without new information. Hence, coincident boundaries lead to a coupled analysis that does not allow the codes to interact and exchange information and yields an iteration procedure that will not be reliably convergent.

Therefore, the proper coupling between these codes requires that the boundaries of the computational zones not be coincident. Furthermore, the boundaries of each zone should be arranged such that the boundary conditions are dependent upon the solution in the neighborhood zone. This allows the necessary transfer of information from one zone to another. In the present coupling procedure, this is accomplished by overlapping zonal boundaries (see Figure 3).

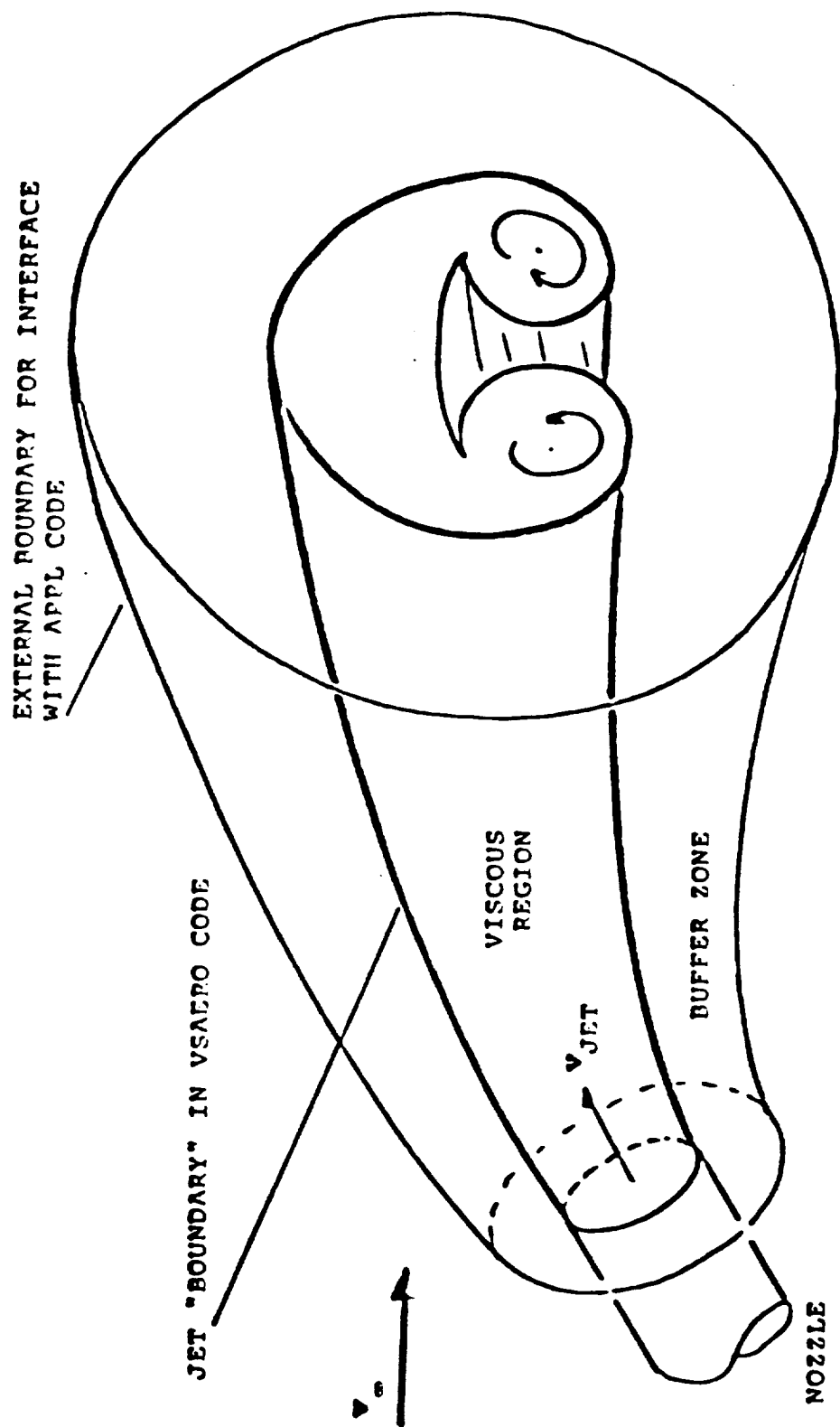


Figure 3. Illustration of the Overlap Region in the VSAERO/APPL Coupling.

### 3.0 NEW PROCEDURES

#### 3.1 Coupling

The initial approach to coupling VSAERO with APPL has been based on an overlap between the viscous and inviscid regions, Figure 3. On the first pass, these boundaries are generated by the VSAERO code following the jet boundary relaxation calculation; subsequently, APPL provides these boundaries. In the present work emphasis has been placed on creating a more automatic treatment of the coupling procedure.

The basic steps in a coupled run are as follows:

1. Perform the VSAERO calculation using the vortex tube model of the jet, jet efflux plane and jet boundary relaxation (11), see Figure 4(a). The calculation starts with a trajectory given by Margason's equation.
2. Generate the external boundary, Figure 3.
3. Compute the velocities at the external boundary points and form a file of X, Y, Z, VX, VY, VZ, V, CP.
4. Transfer the file from step 3 to the APPL code.
5. Perform the APPL calculation.
6. The APPL code creates two files (refer to Appendix A for file handling) for the return to VSAERO.

- (i) The boundary of the viscous region together with the velocity vectors. Each record contains

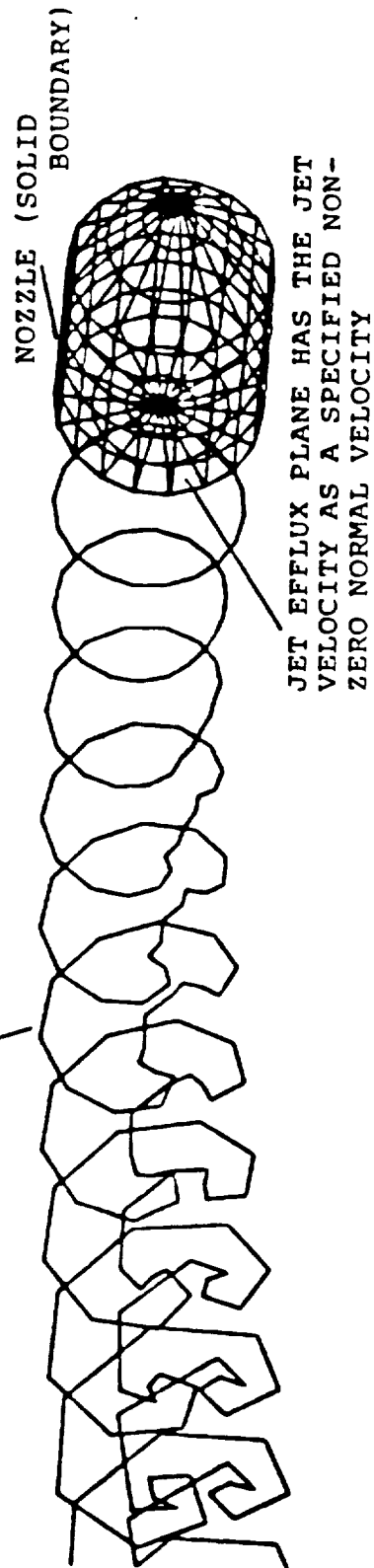
X, Y, Z, VX, VY, VZ

This information is arranged as a series of points around a section with the sections proceeding along the jet axis. This will define the jet boundary for the VSAERO calculation.

- (ii) The boundary of the outer region, Figure 3, giving an adequate "buffer" zone beyond the viscous boundary. This is just a file of points (X,Y,Z) at which VSAERO will compute the velocities for the next phase.
7. The VSAERO code performs a calculation with the inner boundary paneled and with non-zero normal velocities, Figure 4(b). The jet exit plane and the vortex tube jet boundary model have been removed from the Step 1 model.
  8. Return to Step 3 for another iteration but use the boundary file from Step 6(ii).

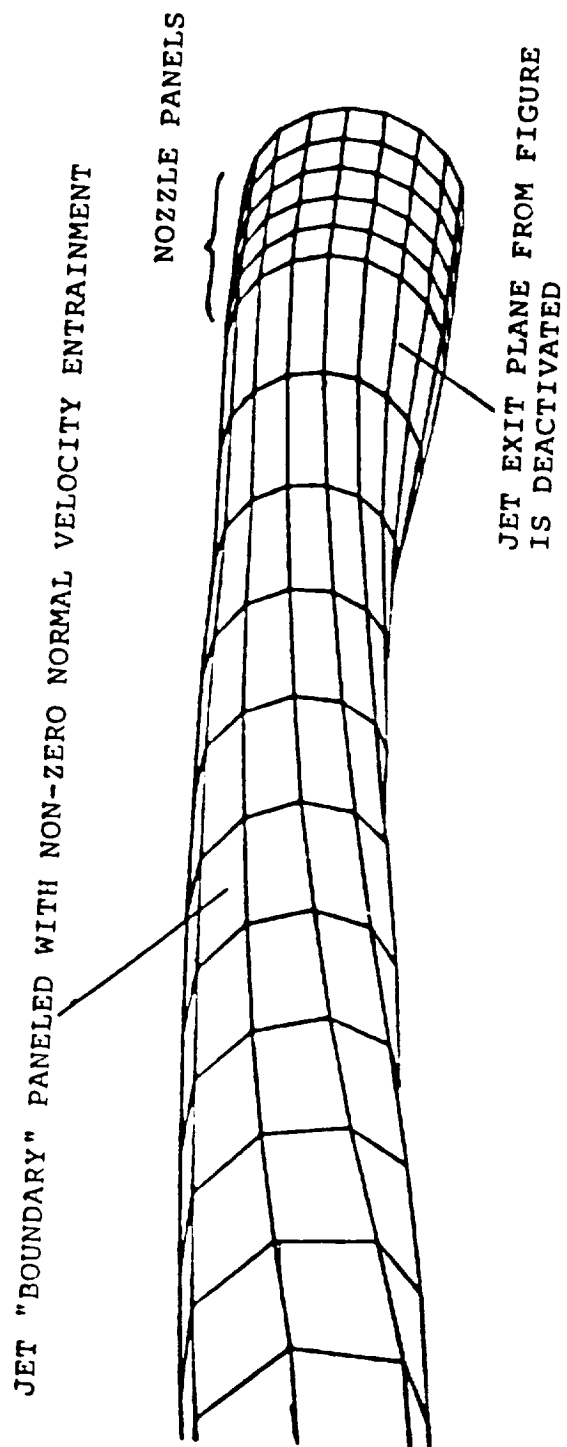


VORTEX TUBE MODEL (ONLY THE CROSS SECTIONS  
ARE SHOWN HERE)



(a) Initial Model

Figure 4. VSAERO Calculation.



(b) Second and Subsequent Models

Figure 4. Concluded.

While the above approach, i.e., a "solid" boundary treatment of the jet boundary in VSAERO together with the entrainment model, should adequately represent the jet plume effects on nearby surfaces that are external to the jet boundary, details of the inner flow are only present in the PNS calculation. Details of the flow about a body immersed in the jet plume (turning vanes, for example) would therefore be lost unless a more complicated PNS treatment were installed to include the body surface in the calculation.

### 3.2 VSAERO Modification

The jet model in the VSAERO code was refined to improve the stability of boundary relaxation and also to maintain a boundary shape. Regarding refinements in the jet boundary relaxation procedure, the basic vortex tube model for jet boundary representation in VSAERO was considerably enhanced under Phase I by including self-generated grid planes normal to the mean axis of the jet (11), (13). Using in-plane velocity components rather than complete velocity vectors gave a significant improvement in the stability of the relaxation calculation (i.e., the velocity at each boundary point was separated into an axial transport component and a "distortion" component in each normal plane). However, a scheme to amalgamate streamwise boundary lines in the intensive roll-up region of the vortex pair essentially lost all definition of the jet "boundary" after only a few steps along the axis; only the vortex pair remained. (This could still be a useful model for initial calculations, particularly if coupled with a line sink to represent the turbulent mixing terms.) For the present objectives, the amalgamation scheme was modified to allow the jet cross-section shape to be "frozen" after a few steps of development of the kidney shape. From that point on the frozen shape is located in each normal grid plane according to the average of the computed cross-flow velocities.

As a primary Phase II task, the interface of coupling in VSAERO is also added. At Step 2 in the coupling, the trajectory of the jet centerline has been computed in the presence of the rest of the configuration. The first external boundary (Figure 3) is then generated as a series of circles progressing along the jet axis with centers located on the jet axis. The circle radius increases with distance along the axis; the rate of increase is controlled in two zones using input parameters. Default values are available for these parameters to keep the growth of this boundary as small as possible but of sufficient size so as to contain the APPL viscous calculation. The density of points around the boundary and in the axial direction are input parameters at this time. Again, reasonable default values are available in order to minimize the user's task.

The complete set of points on the external boundary is now assembled into files. A velocity scan subroutine called JSCAN has therefore been modified to either accept files of points for multiple numbers of jets or to use the previous approach of generating each point and calculating the velocity on it immediately. With this addition the velocity scan procedure in JSCAN can readily switch over to read the file of external boundary points supplied by the APPL code (see Step 6(ii) above) on subsequent passes and to write the file containing the current velocities. The file created by the velocity scan procedure has the following format

\* M, N                    (The number of stations and number of  
points per station, respectively)

followed by N x M records,

*	X	Y	Z	VX	VY	VZ	V	Cp
.	.	.	.	.	.	.	.	.
.	.	.	.	.	.	.	.	.
.	.	.	.	.	.	.	.	.

This file is then transferred to the APPL code.

At Step 7 (see Section 3.1), the VSAERO code accepts the file from Step 6(i) containing a set of points defining the boundary of the viscous region in the APPL calculation, together with their velocity vectors; i.e., an R, V file. The next and all subsequent VSAERO calculations are then performed with the jet surfaces paneled as "solid" but with each panel having a non-zero normal velocity, Figure 4. Compared with the first calculation, therefore, each jet boundary vortex tube (Type 3 wake) has been replaced with a solid (Type 2 patch) surface and the jet exit plane on which the jet velocity was specified has been removed.

The geometry input routine in VSAERO has now been modified to accept the above R, V, file as patch data under a new MODE option. The information is treated in the same way as "basic points" on "defined sections" of a patch so that the data can be converted automatically to a more convenient paneling scheme if required. At the same time, the interpolation scheme has been extended so as to treat the velocity information in the same way. Thus, each panel corner point, whether generated or taken directly from the file, also has the local velocity vector. When the parameters are being formed for a panel we now compute the dot product between the panel normal and the average of its four corner velocity vectors. This non-zero entrainment becomes a source term in the boundary condition equations and thereby influences the solution on nearby surfaces.

### 3.3 APPL Modification

To achieve a simultaneous solution of the overall flow field, the APPL and VSAERO codes must be coupled such that their interzonal boundary conditions interact by passing useful information between zones. Hence, the boundary conditions for VSAERO are obtained from within the APPL zone at a position adjacent to the plume. Similarly, the APPL boundary conditions are obtained from inside the VSAERO zone. The interzonal boundary conditions are updated after each iteration of the zonal solutions. The overall solution converges when these boundary conditions converge.

The transfer of the boundary condition data is accomplished by generating files that are input and output from the codes at the appropriate times. The APPL code has been modified under TASK 1 to include routines to input the boundary conditions provided by VSAERO. One routine is called during the initialization of the first solution plane at the nozzle exit to

input the velocity components at the mesh points that extend into the VSAERO domain. Temperature and pressure are calculated by assuming constant total thermodynamic conditions, which is consistent with potential flow theory. The routine could be modified to accept an external boundary layer. The turbulence quantities at these points are initialized with the free stream values. As the APPL solution is marched downstream, similar boundary condition data from the VSAERO zone are input through a second routine for the outer boundary. This routine also reads the coordinates of the boundary mesh points. If the solution plane does not coincide with a boundary condition plane, interpolation is used. Since the initial boundary is provided by VSAERO without interaction with APPL, the outer boundary position may not be adequate. In this case an option may be selected to allow APPL to determine its own boundary. The VSAERO boundary conditions are still used as an initial guess.

As the APPL code marches the solution downstream, an output routine is called to generate a file defining the plume edge boundary conditions for VSAERO. At each solution plane, the routine writes out the coordinates and velocity components for a string of mesh points that surrounds the plume. To ensure that these points do not lie within the plume, APPL monitors the vorticity of each point. The coordinate and velocity data are then used to generate the plume panels and the normal velocity components that represent the influence of the plume on the surrounding flow. APPL also appends to this file the coordinates defining the new outer boundary position. VSAERO uses these coordinates to provide the boundary conditions for the next iteration of APPL.

The mesh generator inside the APPL code has been rewritten to accommodate the coupling with VSAERO. Since the interzonal boundaries overlap, the mesh is structured to maintain a given number of mesh cells between the plume edge and the outer boundary. A vorticity monitoring scheme is used to locate the plume edge. The vorticity distribution along each mesh ray is calculated to obtain the peak value. Then moving outwards along a ray the plume edge is defined as the point at which the vorticity falls below a given level. This approach works very effectively for controlling the growth rate of the mesh as the plume spreads. The vorticity monitor also can track the centerline trajectory of deflected jets. The center of the locus of points defining the vorticity maxima on the mesh rays is used to define the center of the jet. The centers calculated for two adjacent planes are then linearly extrapolated to determine the mesh center point for the next solution plane. The plume tracking procedure keeps the plume away from the outer boundary of the mesh even when the deflection angles are large.

APPL is a PNS code and, therefore, is limited by the parabolic approximations which assume that no upstream influence exists. This restricts the pressure field to being elliptic in just the cross stream direction for subsonic flows. For modestly deflected plumes the parabolic approximation for the pressure field should be reasonable. At large deflection angles the curvature of the plume trajectory may be significant, making the pressure elliptic in all directions.

In the two-dimensional pressure correction equation only the pressure perturbations at the  $i^{th}$  plane were allowed to influence the mass fluxes through the surfaces enclosing any of the  $ijk$  cells. This is consistent with the PNS assumption of negligible upstream influence. To capture three-dimensional elliptic effects (PNS/EP), however, the influence of pressure corrections at adjacent planes on cell continuity must be included. Since the streamwise pressure gradient term is the only term that allows upstream propagation, it is approximated by a forward difference. Thus, the effects of pressure corrections on the  $u$  component of velocity, for example, takes the form

$$u'_{ijk} = -\frac{1}{(\rho u)_{ijk}} \left\{ \frac{1}{4} \xi_z [(P'_{i+1,j,k} + P'_{i+1,j-1,k} + P'_{i+1,j,k-1} + P'_{i+1,j-1,k-1}) - (P'_{ij,k} + P'_{ij-1,k} + P'_{ij,k-1} + P'_{ij-1,k-1})] \right. \\ \left. + \frac{1}{2} \eta_z (P'_{ij,k} + P'_{ij,k-1} - P'_{ij-1,k} - P'_{ij-1,k-1}) \right. \\ \left. + \frac{1}{2} \sigma_z (P'_{ij,k} + P'_{ij-1,k} - P'_{ij,k-1} - P'_{ij-1,k-1}) \right\}$$

The Cartesian components of velocity at  $i-1$  are also used in the calculation of the error in continuity for the  $ijk$  cell. These velocity components are related to pressure perturbations at the  $i$  and  $i-1$  stations through a similar relation as above. Thus, the resulting pressure correction equation, which relates pressure corrections at station  $i-1$ , and  $i+1$ , has the form

$$\sum_{l=-1}^1 \sum_{m=-1}^1 \sum_{n=-1}^1 a_{i+l,j+m,k+n} P'_{i+l,j+m,k+n} = CONT_{ijk}$$

The triple summation represents 27 pressure corrections affecting the continuity error for the  $ijk$  cell. The coefficients include the effects of the pressure corrections on continuity through the density and velocity perturbations in the manner demonstrated in Section 2.2.2.

An iterative line relaxation method similar to the one employed in the two-dimensional case is used to find the solution of the system of equations. A third step is added which treats the  $i$ -direction implicitly. Due to the nature of the formulation the tridiagonal matrices that result in each sweep are diagonally dominant, and the inversions are stable.

## 4.0 RESULTS AND DISCUSSION

Several test cases have been run to validate and demonstrate a coupling capability between the APPL code and the VSAERO code. These cases range from a simple circular jet on a plate to double jets of a V/STOL configuration (16). Experimental data, where available, were compared with calculations and it was noted that these data were not corrected by the blockage effect of the wind tunnel.

Simple laminar and turbulent jet flows were used to validate the numerical model incorporated in the APPL code. Analytical asymptotic solutions for laminar two-dimensional and circular jets in a quiescent free stream are available (17). To model these flow fields the jets were initialized with a small streamwise component in the free stream to avoid stability problems that can occur in PNS method when the cross-flow velocity becomes greater than the streamwise velocity. The APPL solutions were marched downstream until a self-similar solution evolved which could be compared with the analytical results. Analytically, the jet centerline velocity for the two-dimensional and circular jets is proportional to  $X^{-1/3}$  and  $X^{-1}$ , respectively. When the APPL solutions were terminated, the centerline velocities were proportional to  $X^{-.315}$  and  $X^{-.98}$ , respectively. This good agreement indicates that the code is correctly modeling the flow field.

A turbulent axisymmetric jet in a co-flowing stream was run to test the turbulence model. The jet to free stream velocity was 2.17. Experimental data (18) for the centerline velocity decay was available to provide a comparison with calculated results. An axisymmetric jet correction to the turbulence model (15) was used to provide an optimal solution. A comparison with the experimental data is provided in Figure 5. The favorable agreement suggests that the turbulence model is reasonably accurate. The sensitivity of the solution to the initial turbulence levels was briefly examined. Small changes had a minimal effect. Large changes noticeably affected the streamwise location at which the core disappeared. After that, the turbulence production in the shear layer dominated the solution.

### 4.1 A Jet on a Plate

Calculations were made for the nozzle using only geometry with 60° angle of attack with reference to the oncoming free stream flow. The effective velocity ratio of jet velocity over that of the free stream is 8.000. In the APPL code, a two-dimensional pressure equation was employed in this computation. The jet centerline trajectory was calculated internally using the vorticity monitor. In the VSAERO code, a jet wake calculation was initiated along a trajectory by Margason (12). From the second iteration onwards, jet wake grids are replaced by 16 x 44 solid jet surface panels subject to a Neumann boundary condition of entrainment. Up to 5 iterations were performed between the VSAERO and APPL codes. VSAERO calculations were made on a MicroVAX at AMI, and required about an hour of CPU time per iteration, while APPL calculations made on a Cray X-MP 48 at NASA Ames Research Center required less than 10 minutes of CPU time per iteration.

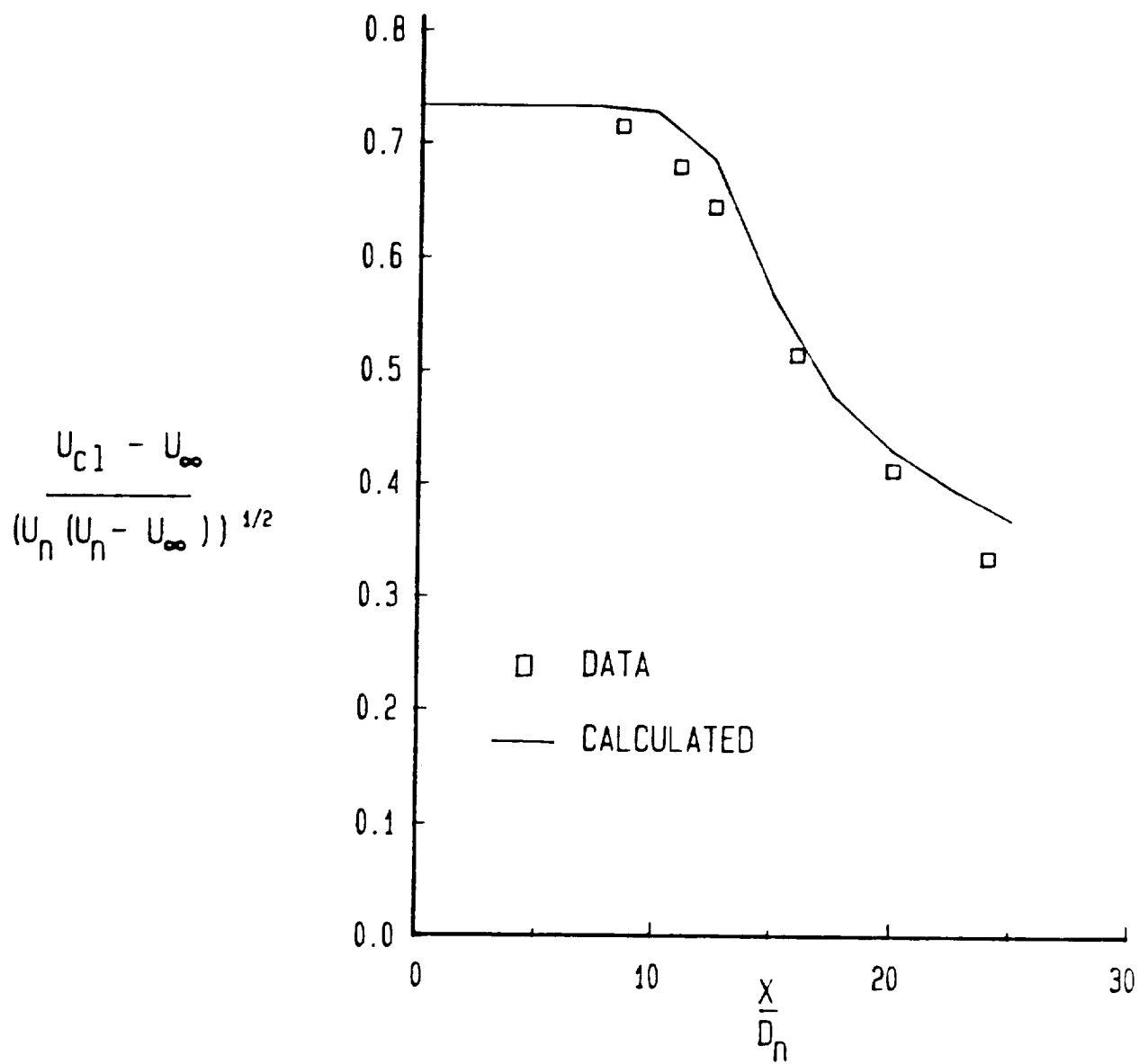


Figure 5. Centerline Velocity Decay for Turbulent Jet in a Coflowing Stream.



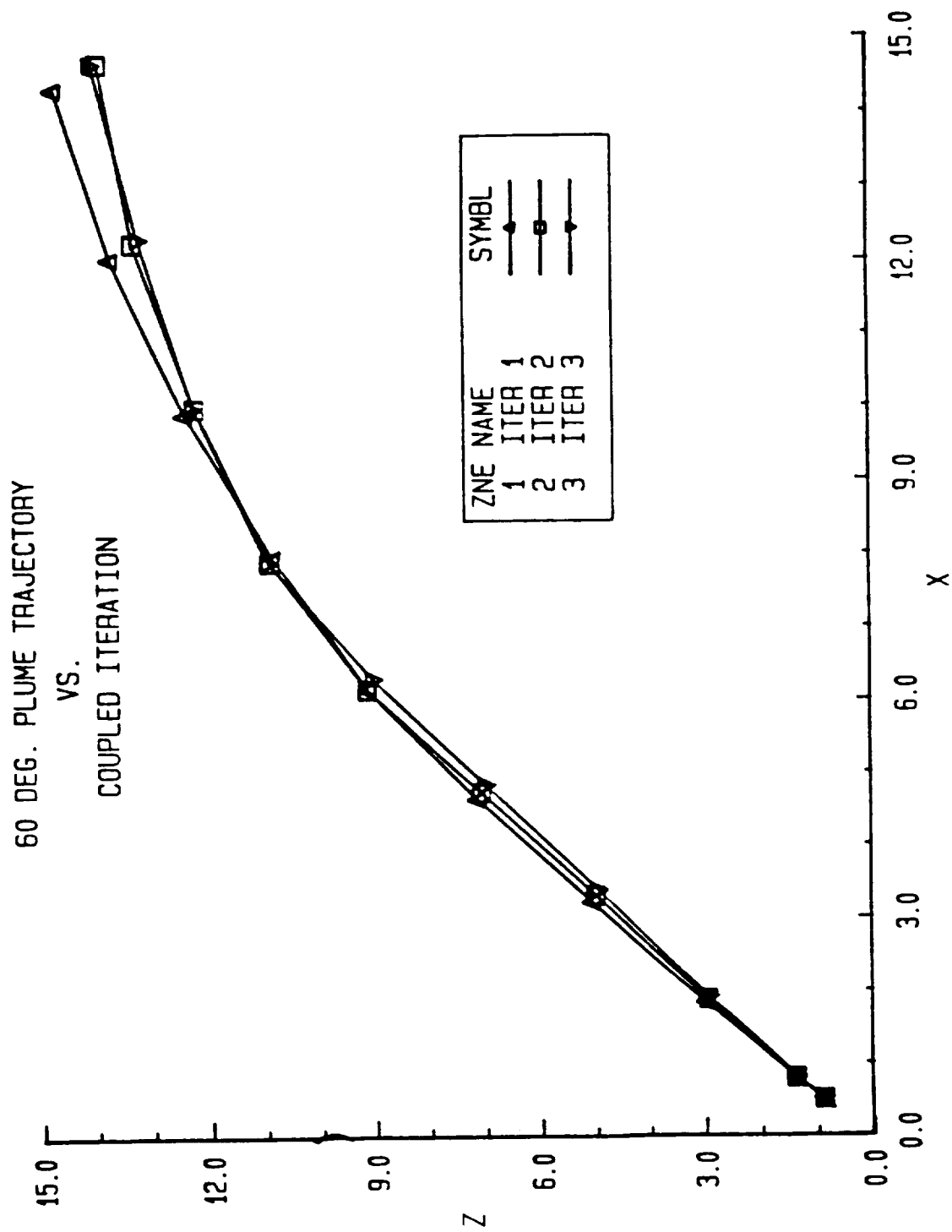
The results for a 60° deflection of the nozzle-only geometry are shown in Figures 6(a) through (n). Good convergence characteristics are observed; details are as follows. Figure 6(a) provides a convergence history for the jet trajectory versus the iterations of the coupled analysis. After the second iteration the trajectory is acceptably converged and the jet mesh could be frozen. The convergence rate is likely to be case-dependent, particularly as the complexity of the VSAERO flow field increases. The stream-wise velocity contours and cross-flow vectors clearly indicate the roll-up of the jet and the pair of counter-rotating vortices, Figures 6(b) and (c). Figures 6(d) and (e) show the convergence history of VNORM which, in fact, is a boundary condition on entrainment. The convergence history of velocity components along the x and z directions is shown in Figures 6(f) and (g). Figures 6(h) through (j) show the characteristics of the symmetry around the y = 0 plane in the velocity components. Figures 6(k) through (n) show the convergence of the boundary condition for the APPL code. In Figures 6(k) and (l), the velocity component in the x direction for the upper and lower surfaces, respectively, is plotted for the 4th iteration versus the 5th one, whereas velocity along the z direction is compared for each iteration in Figures 6(m) and (n). This test case gives a good indication that this approach will work for a real aircraft configuration.

#### 4.2 A No-Jet Model

A model geometry was taken from Mineck and Margason (16) in which numerous experimental data were found available. About 700 body panels were used to construct this geometry. The entire aircraft configuration in Figure 7(a) without lift jet was tested for 10° angle of attack to see how the paneling conformed to the model geometry. Figure 7(b) shows a front vectored-thrust configuration showing each cut of the wing on the fuselage section. Data from these section cuts are compared throughout this report. A VSAERO calculation for this geometry was made on the CRAY X-MP 48 at NASA Ames Research Center, and required less than a minute of CPU time. The aerodynamic data from this calculation were compared with the experimental data in Ref. 16. Figures 8(a), (b) and (c) show  $C_p$  distributions at the bottom of the fuselage and Figures 8(d) through (g) show  $C_p$  comparisons at 4 different spanwise locations on the wing. These results are in excellent agreement with the experimental data.

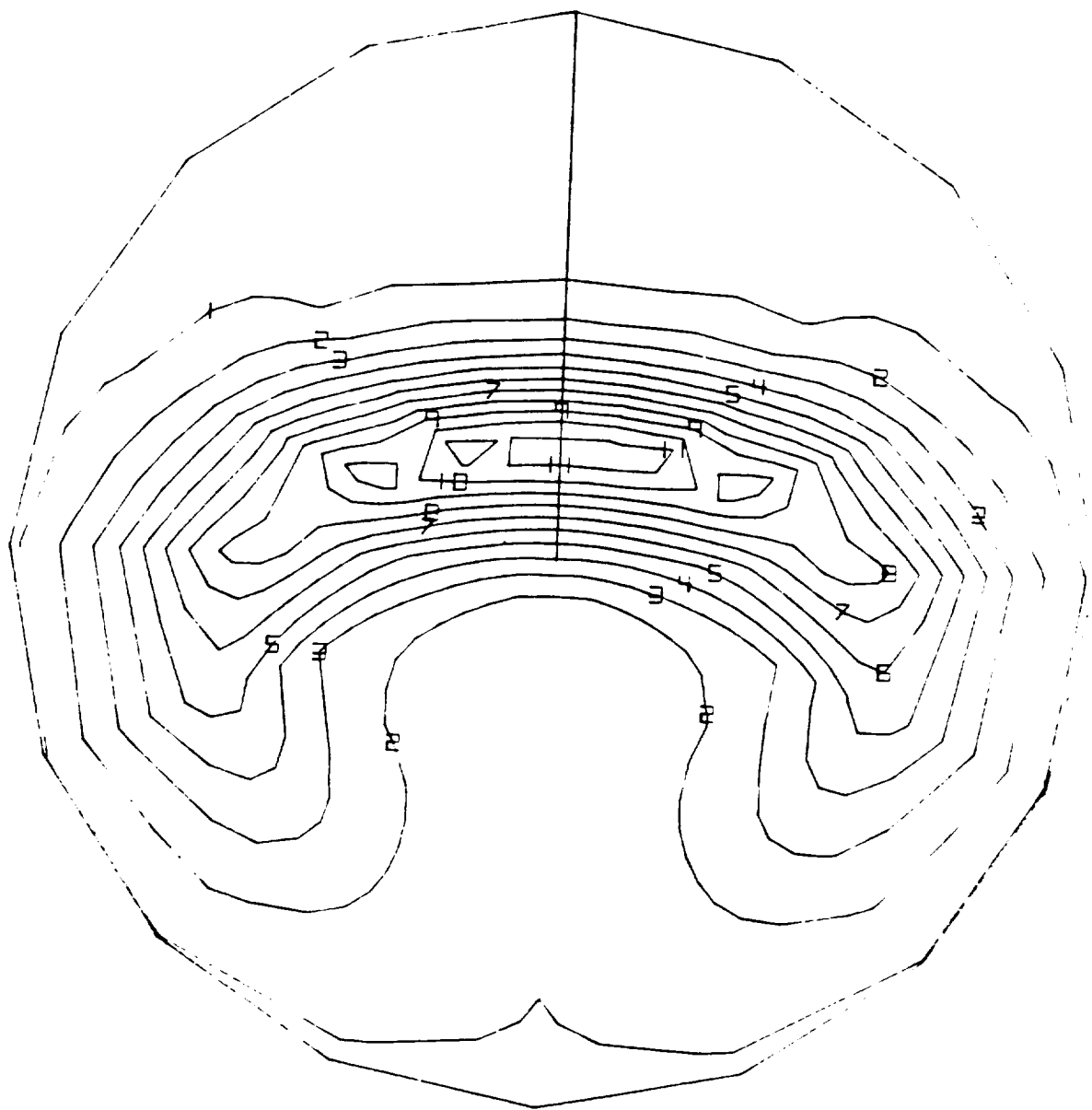
#### 4.3 A Lift-Jet-Only Model

Here, the lift-jet-only case with an effective velocity ratio,  $V_j/V_o = 4.878$ , and the jet-off case with a ratio of  $V_j/V_o = 0$  for zero angle of attack are investigated for the same aircraft configuration. The paneling for this geometry is shown in Figure 9(a), with the jet wake trajectory and the regular plane wake. The symmetry option,  $RSYM = 0$ , describing only the right-hand side geometry is used. 588 panels were used for this aircraft configuration and 264(8 x 33) panels were used for the jet surface at subsequent iterations. Figure 9(b) shows the solid jet surface substituted for the jet wake from the lift jet. It is possible to attach regular wakes to the exit plane of the jet column in order to increase accuracy which will present the jet downstream effect to infinity. As seen from Figures 9(a) and (b), the geometry is very crude in the fuselage area. This resulted



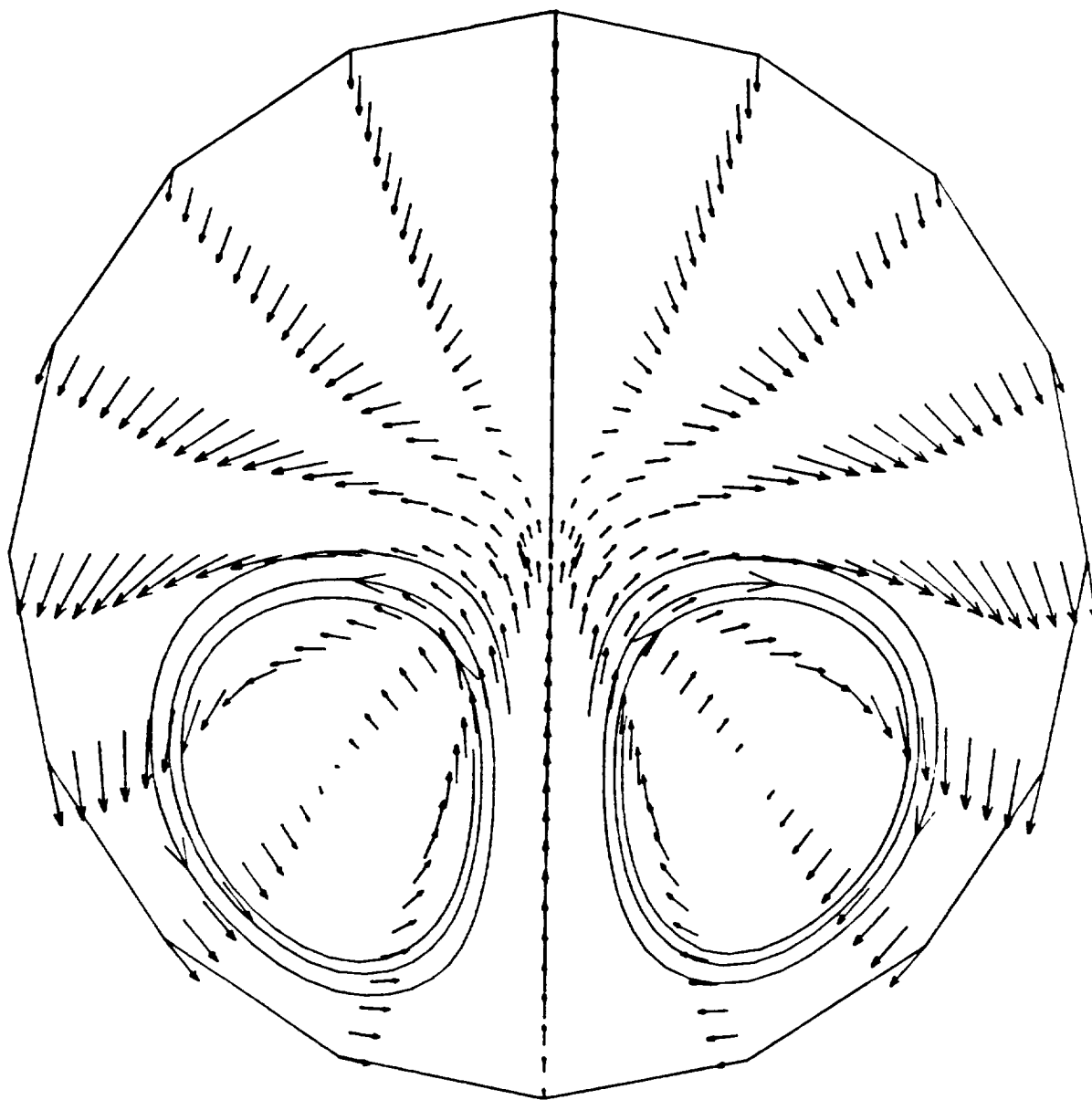
(a) Convergence of Jet Trajectory

Figure 6. Jet at 60° Incidence.



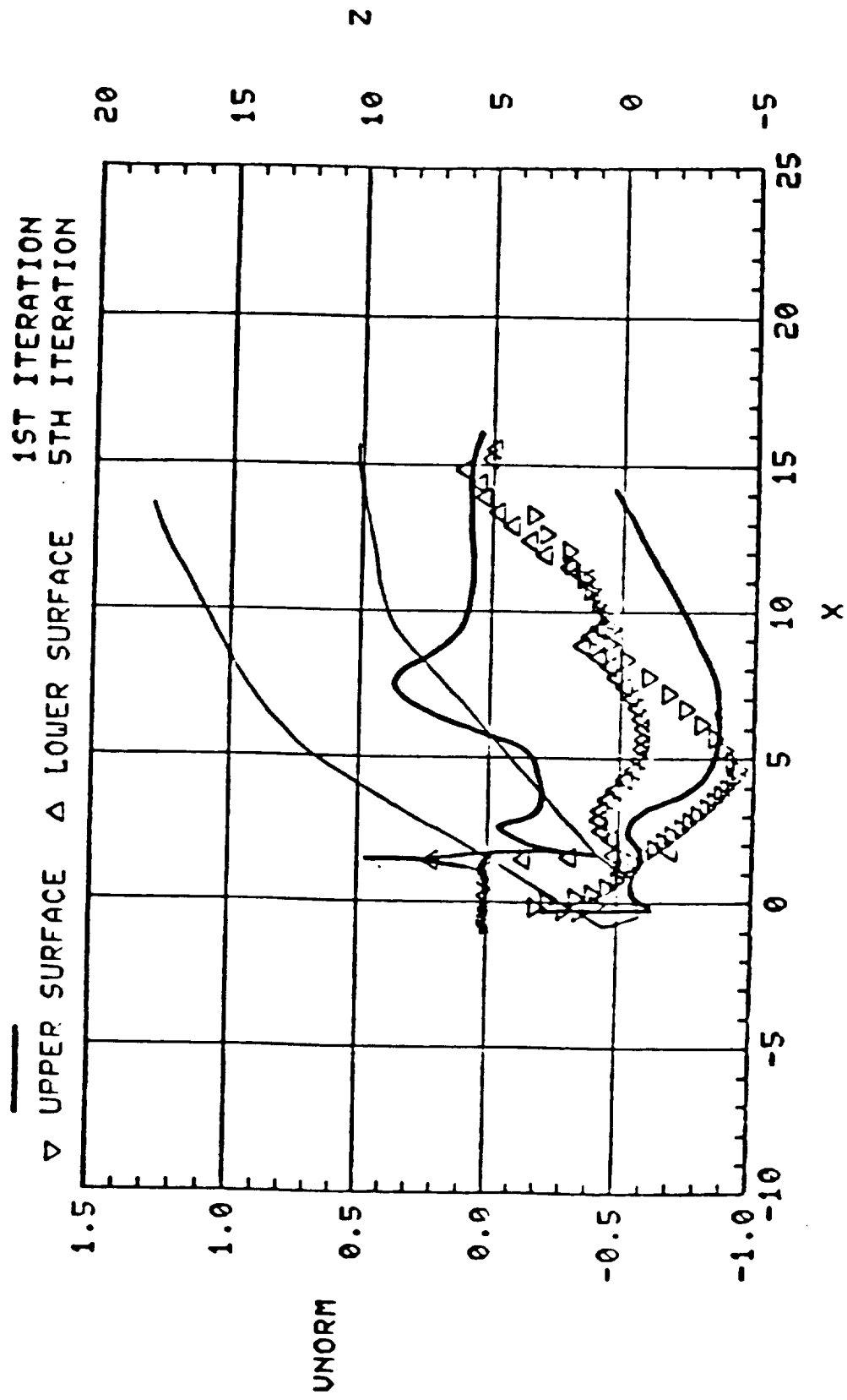
(b) Streamwise Velocity Contours at Several Diameters Downstream from the Nozzle Exit

Figure 6. Continued.



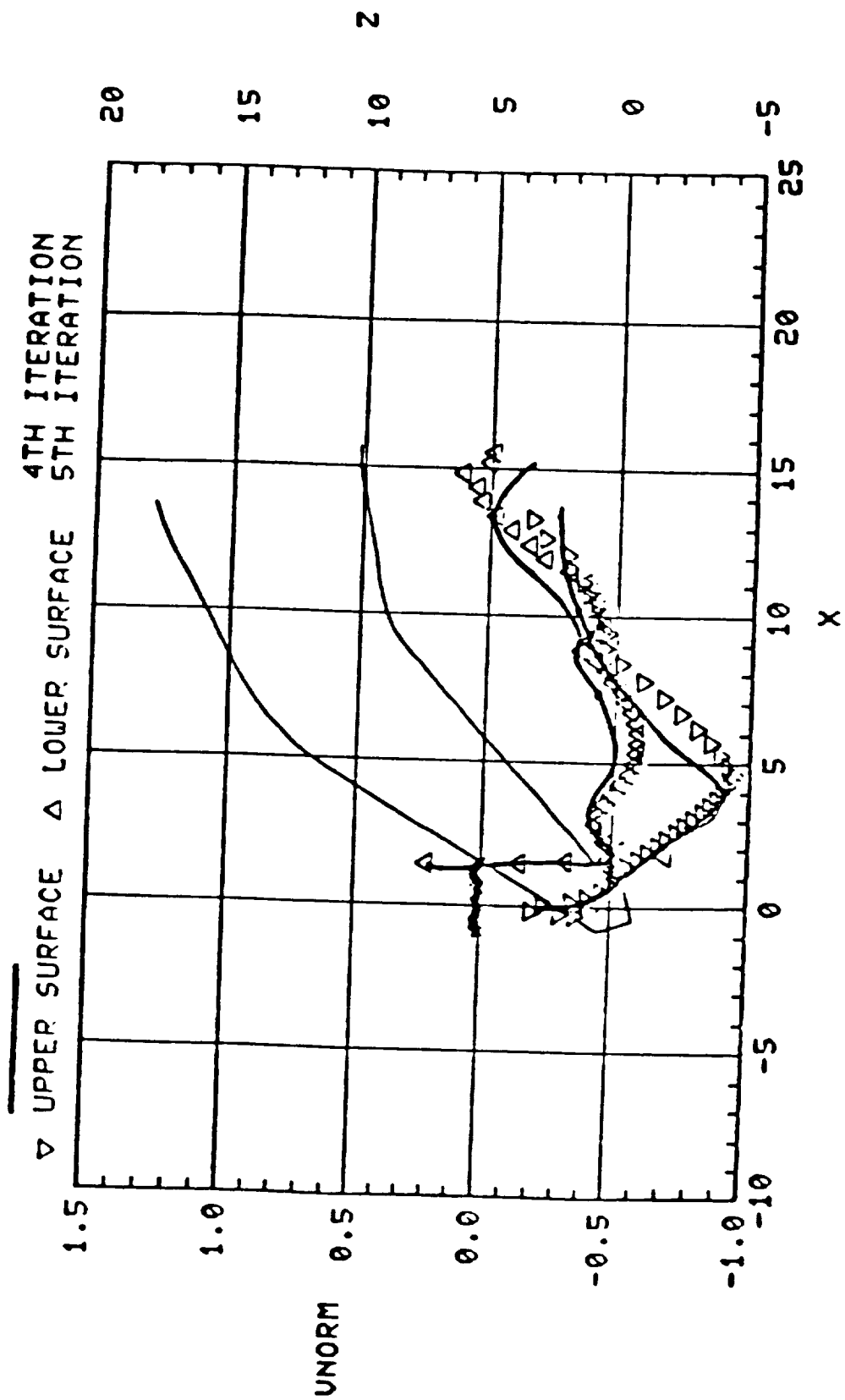
(c) Cross-Flow Velocity Vectors at Several Diameters Downstream from the Nozzle Exit

Figure 6. Continued.



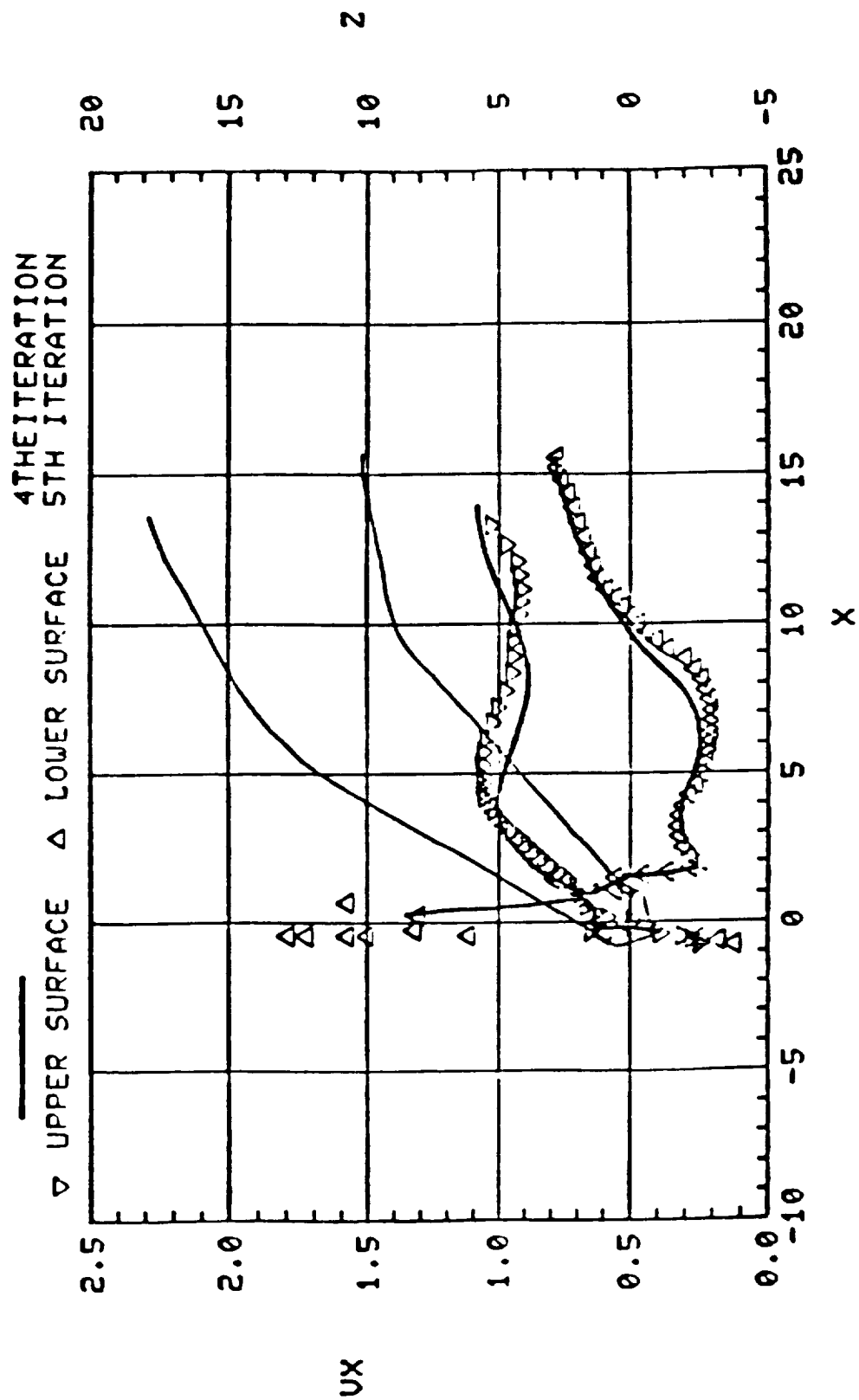
(d) Convergence History (VNORM) at  $Y = 0.0$ ; First and Fifth Iterations

Figure 6. Continued.



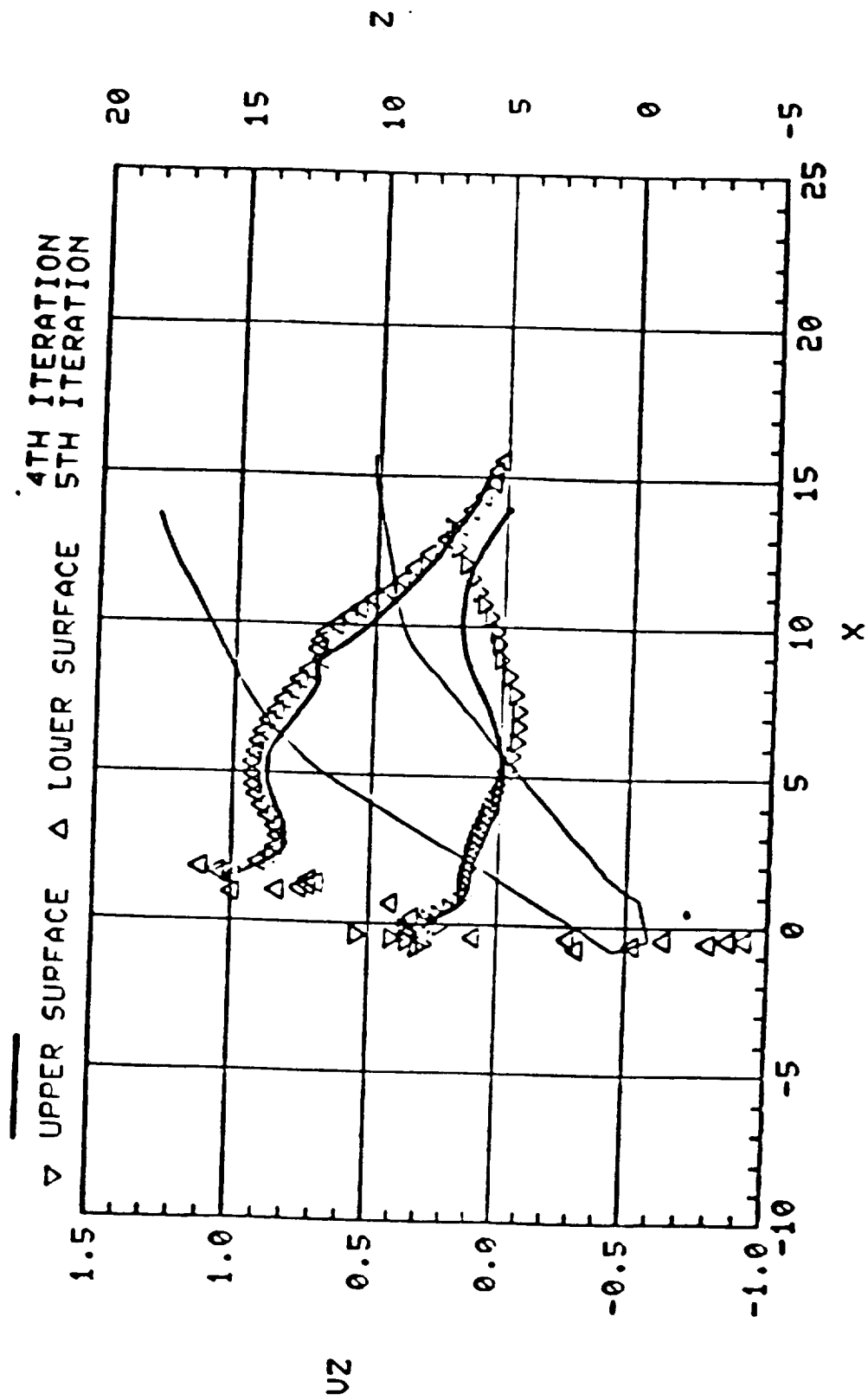
(e) Convergence History (VNORM) at  $Y = 0.0$ ; Fourth and Fifth Iterations

Figure 6. Continued.



(f) Convergence History (VX) at  $Y = 0.0$

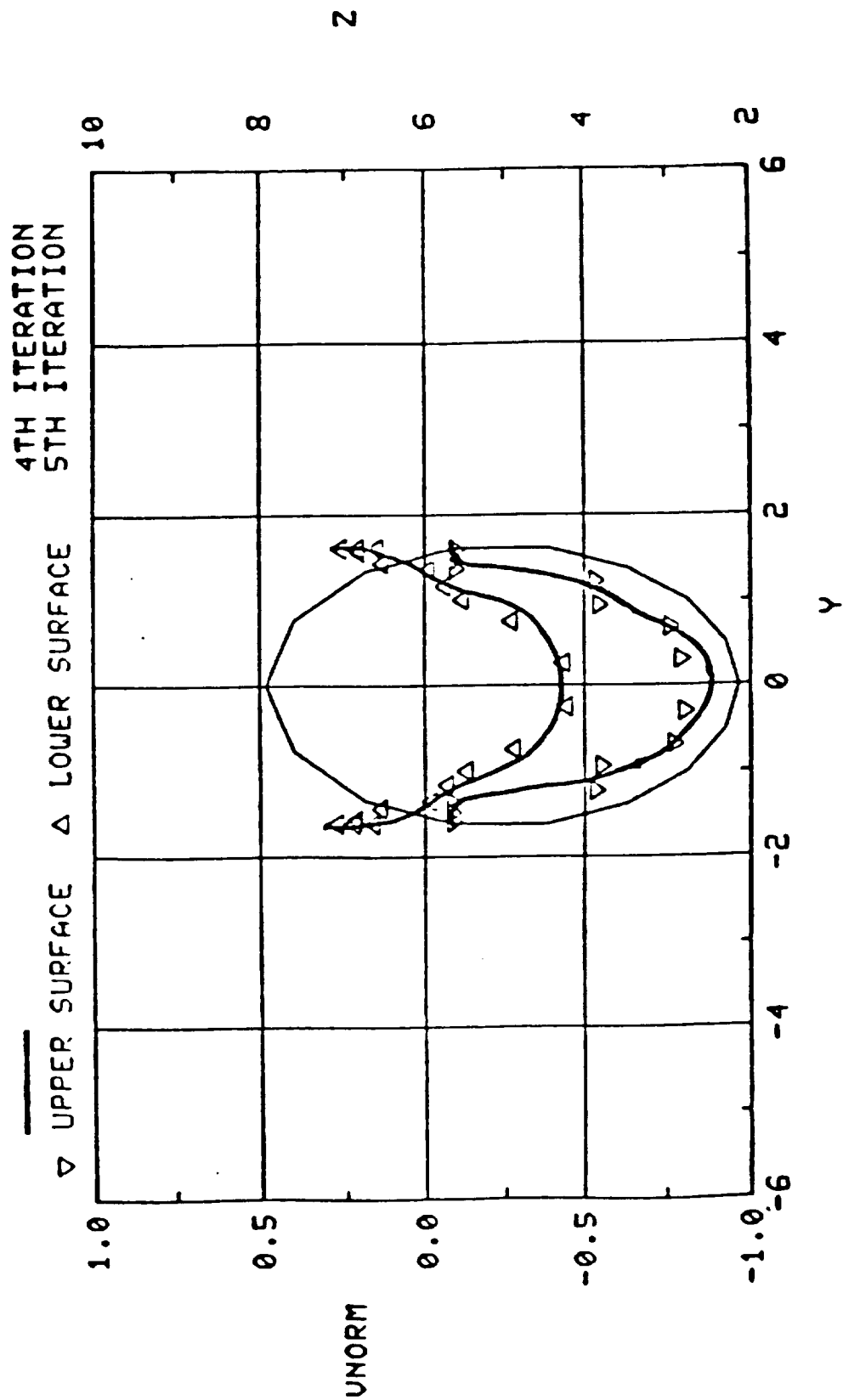
Figure 6. Continued.



(g) Convergence History (VZ) at  $Y = 0.0$

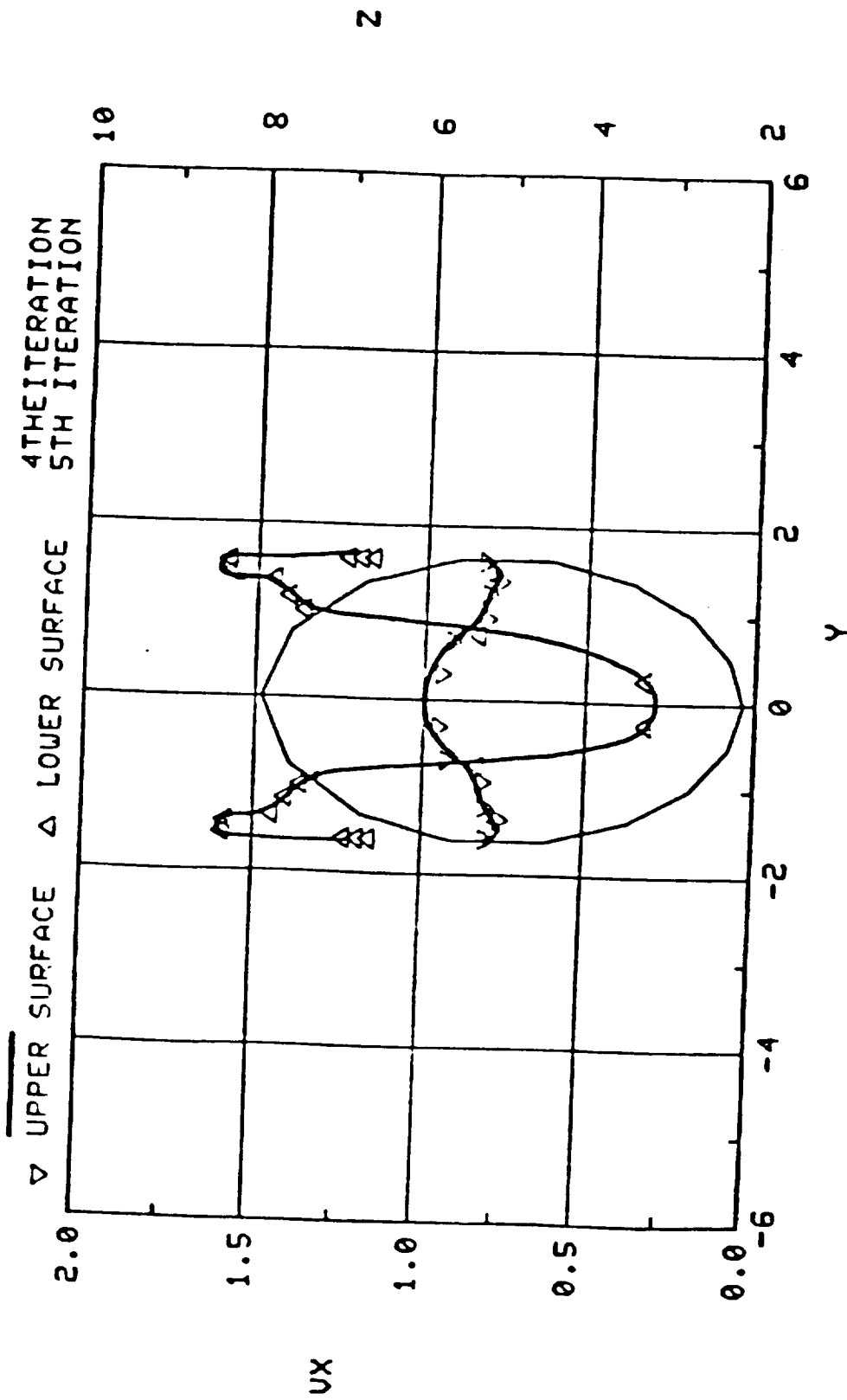
Figure 6. Continued.





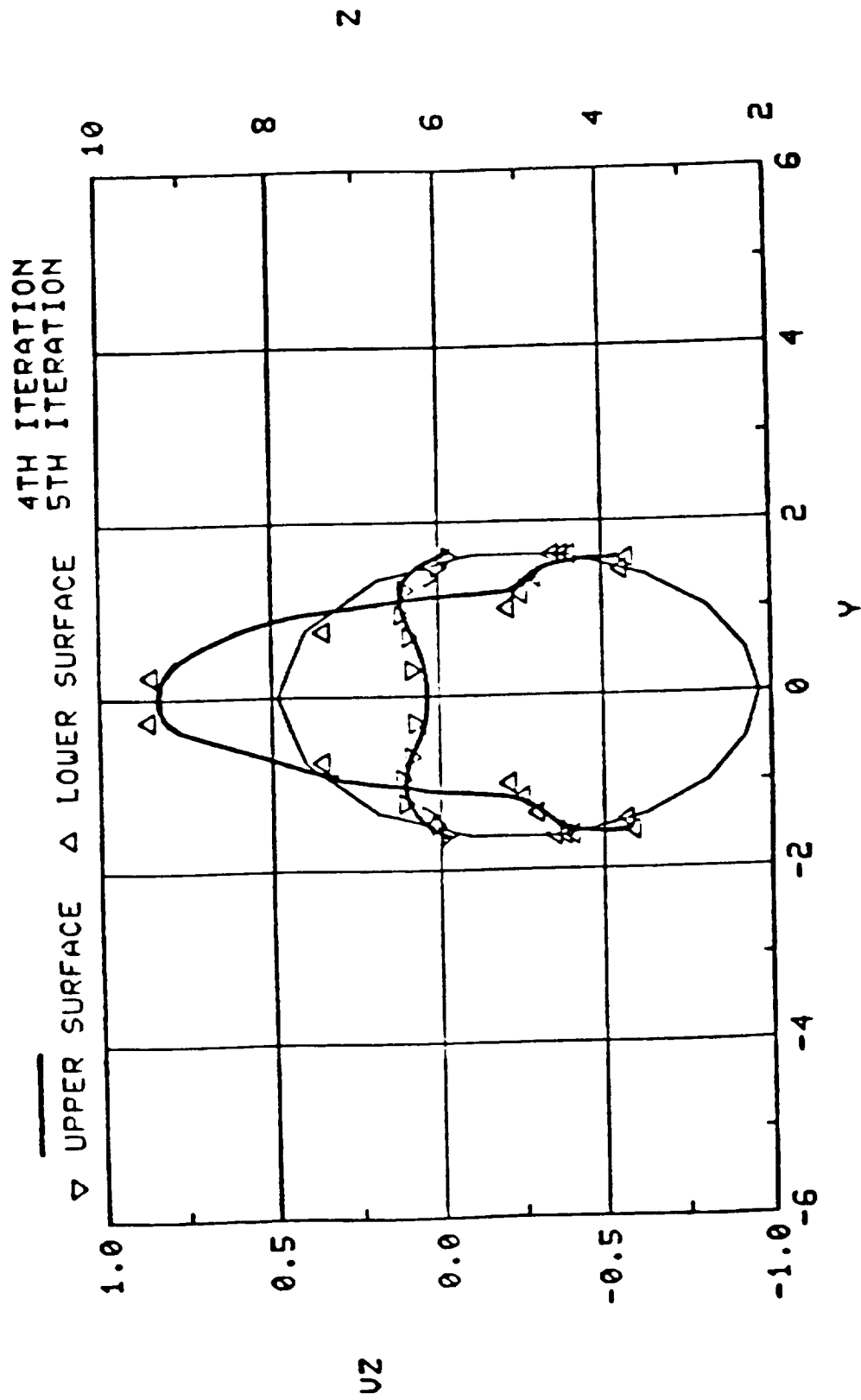
(h) Symmetry in Convergence History (VNORM) at  $X = 3.0$

Figure 6. Continued.



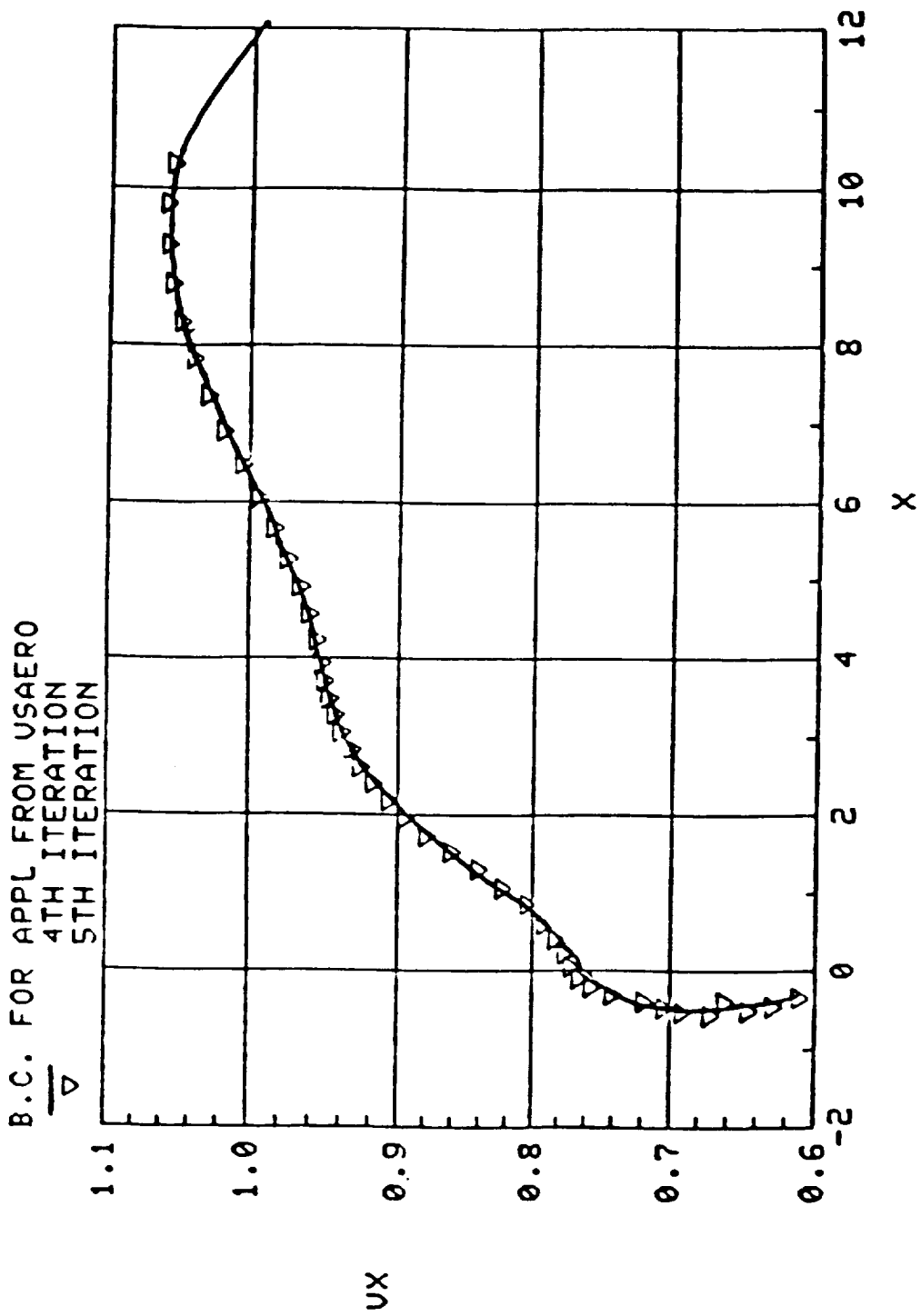
(1) Symmetry in Convergence History (VX) at  $X = 3.0$

Figure 6. Continued.



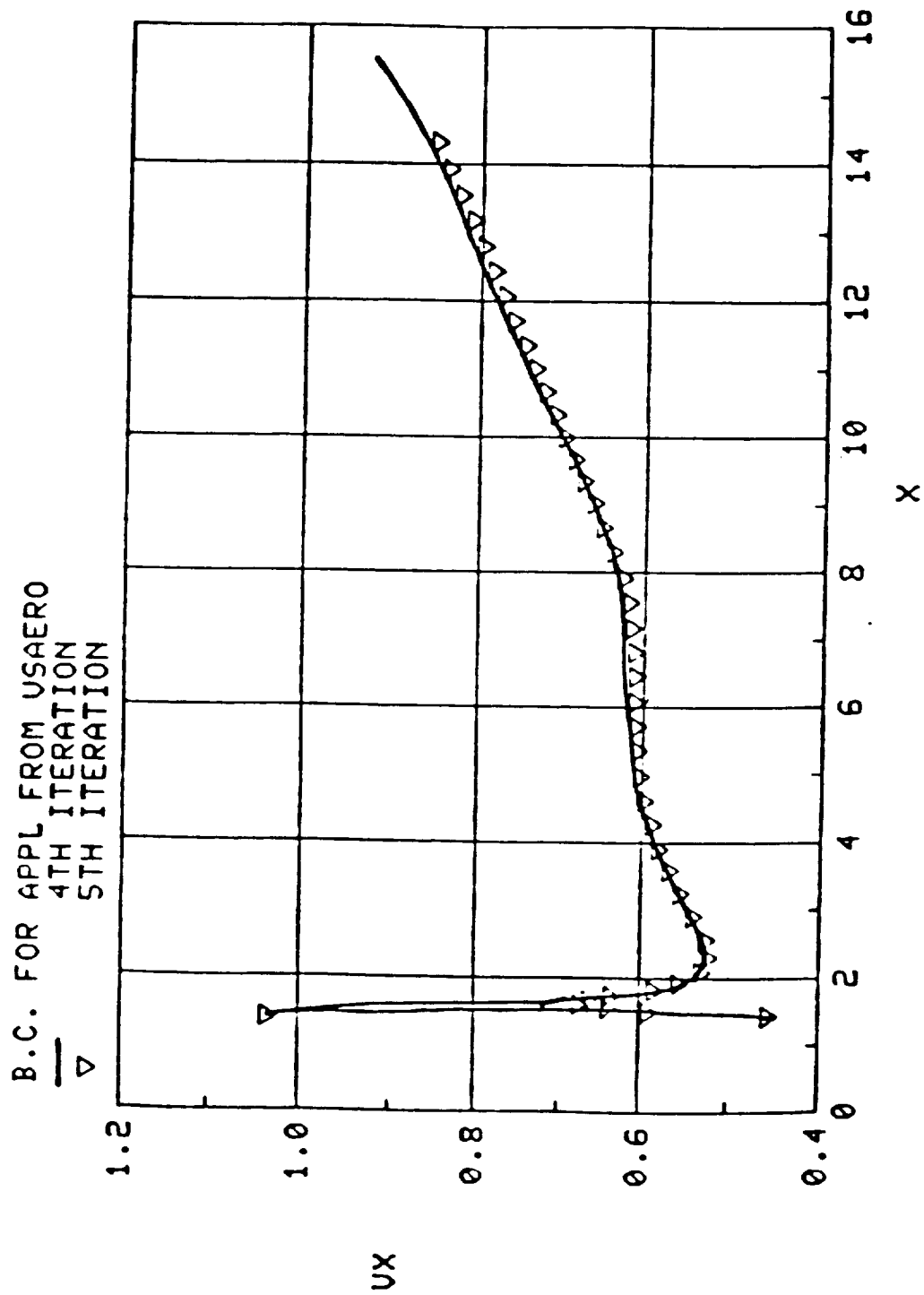
(j) Symmetry in Convergence History (VZ) at  $X = 3.0$

Figure 6. Continued.



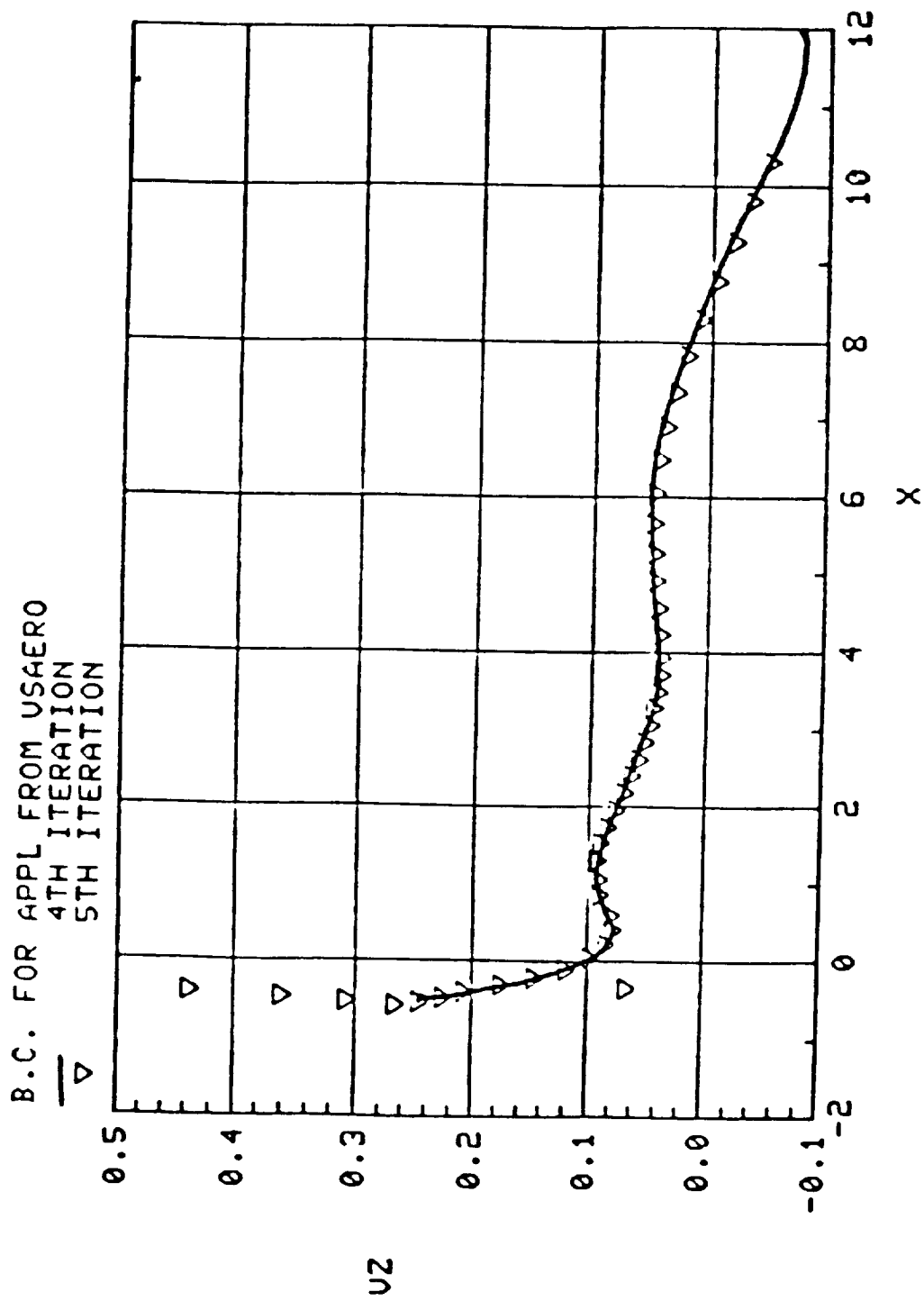
(k) Boundary Condition for APPL from VSAERO (Upper VX) at  $Y = 0.0$

Figure 6. Continued.



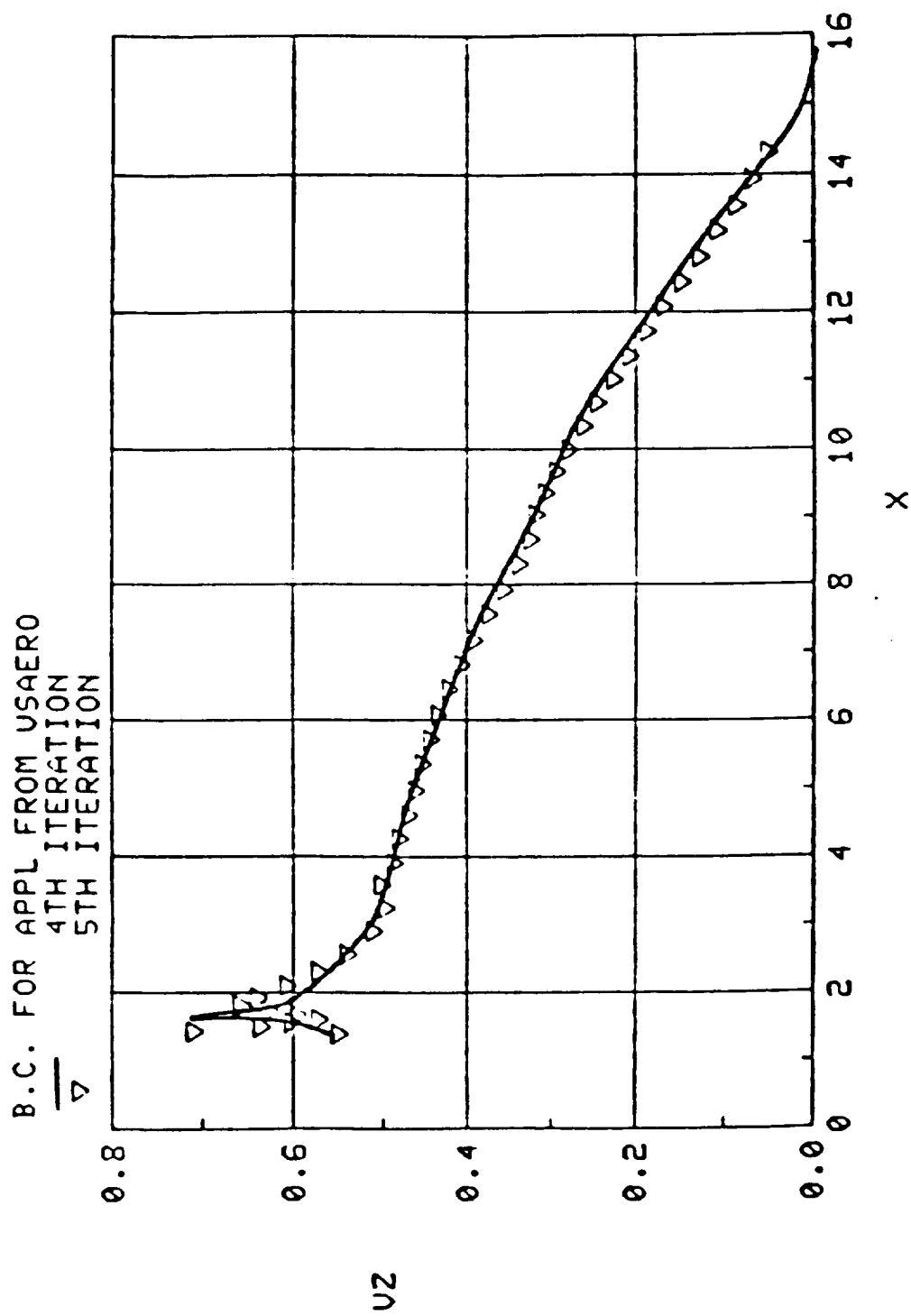
(1) Boundary Condition for APPL from USAERO (Lower VX) at  $Y = 0.0$

Figure 6. Continued.



(m) Boundary Condition for APPL from USAERO (Upper VZ) at  $Y = 0.0$

Figure 6. Continued.



(n) Boundary Condition for APPL from VSAERO (Lower VZ) at  $Y = 0.0$

Figure 6. Concluded.



(a) Lift-Jet Configuration in the V/STOL Tunnel

Figure 7. A V/STOL Configuration.



# GEOMETRY

Wing:

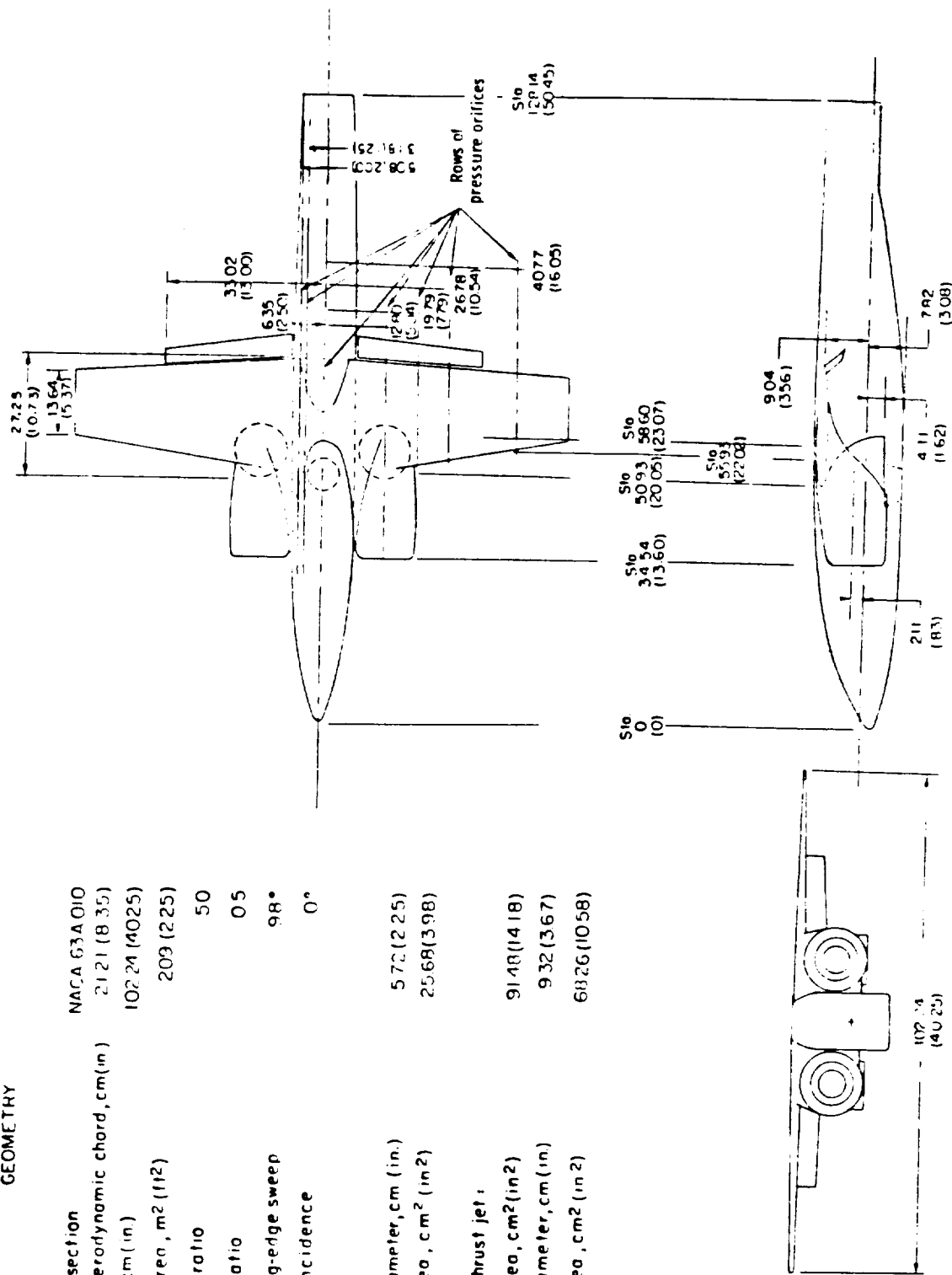
Airfoil section	NACA 63A 010
Mean aerodynamic chord, cm (in)	2121 (8.35)
Span, cm (in)	10224 (402.5)
Wing area, m <sup>2</sup> (ft <sup>2</sup> )	209 (22.5)
Aspect ratio	50
Taper ratio	0.5
Leading-edge sweep	98°
Wing incidence	0°

Luff jet:

Exit diameter, cm (in.)	572 (22.5)
Exit area, cm <sup>2</sup> (in <sup>2</sup> )	2568 (398)

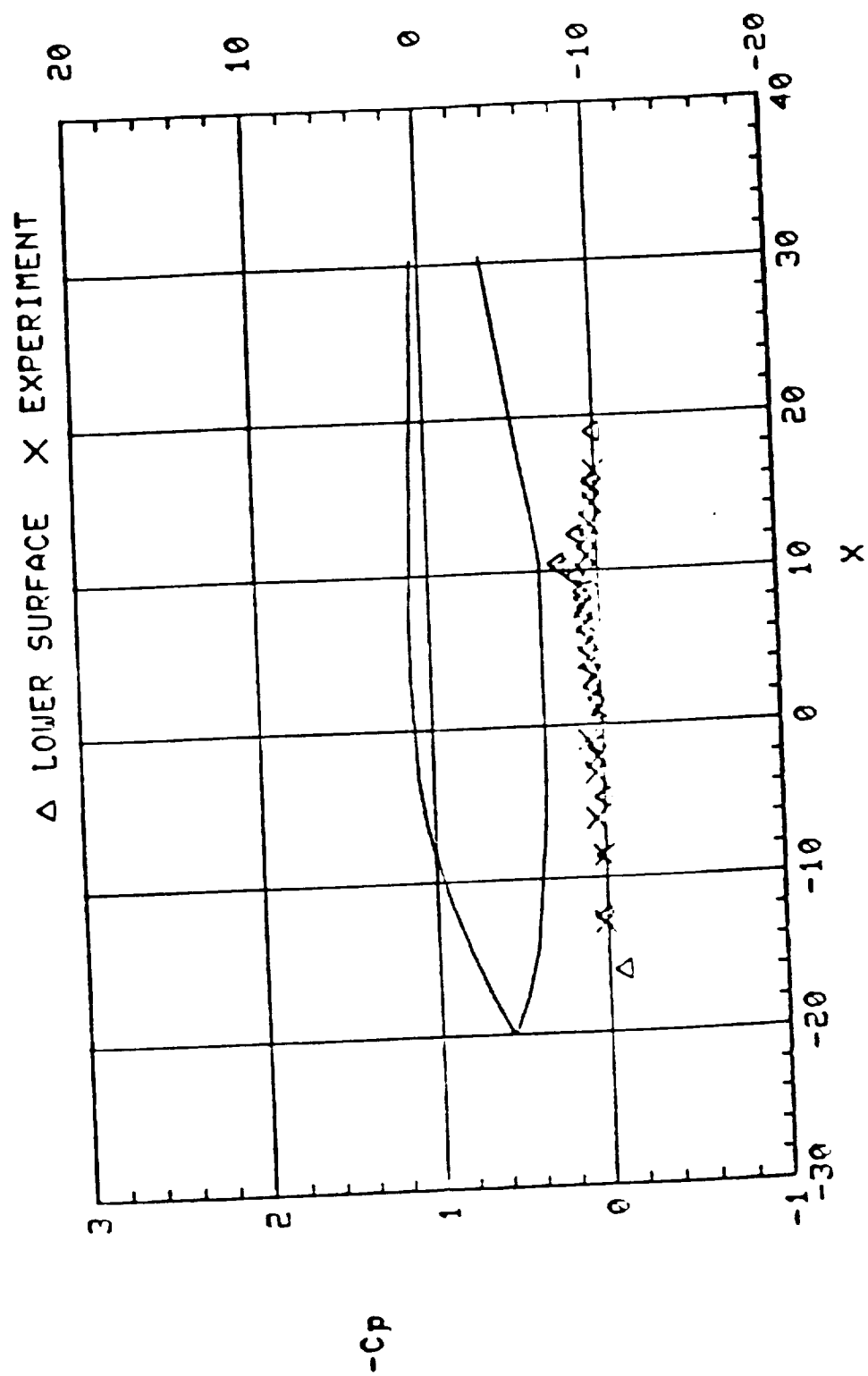
**Vec-tored thrust jet:**

Inlet area, cm <sup>2</sup> (in <sup>2</sup> )	91.48 (14.18)
Exit diameter, cm (in)	9.32 (3.67)
Exit area, cm <sup>2</sup> (in <sup>2</sup> )	68.26 (10.58)



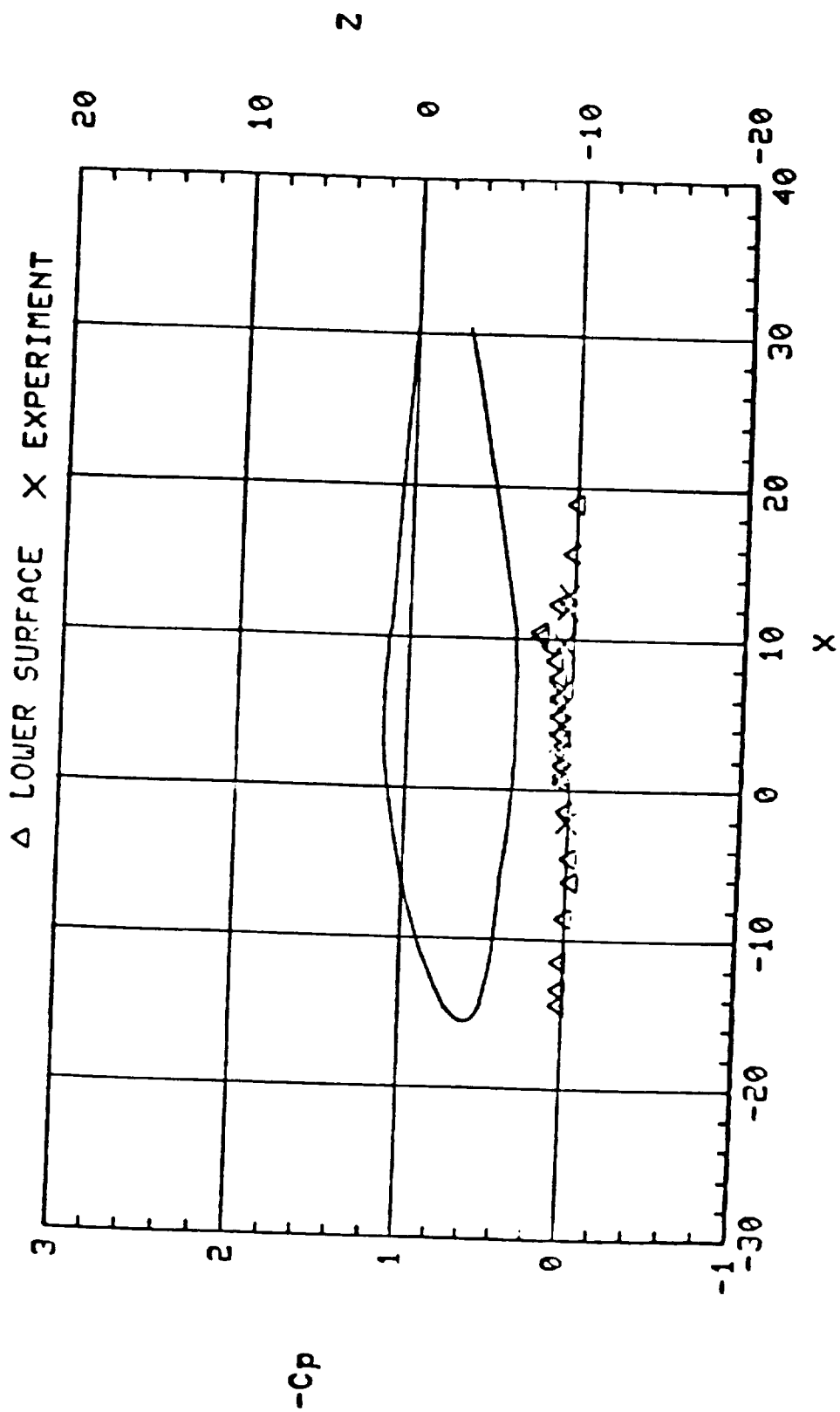
(b) Front Vectored-Thrust Configuration Showing Each Cut on Both Wing and Fuselage Sections

Figure 7. Concluded.



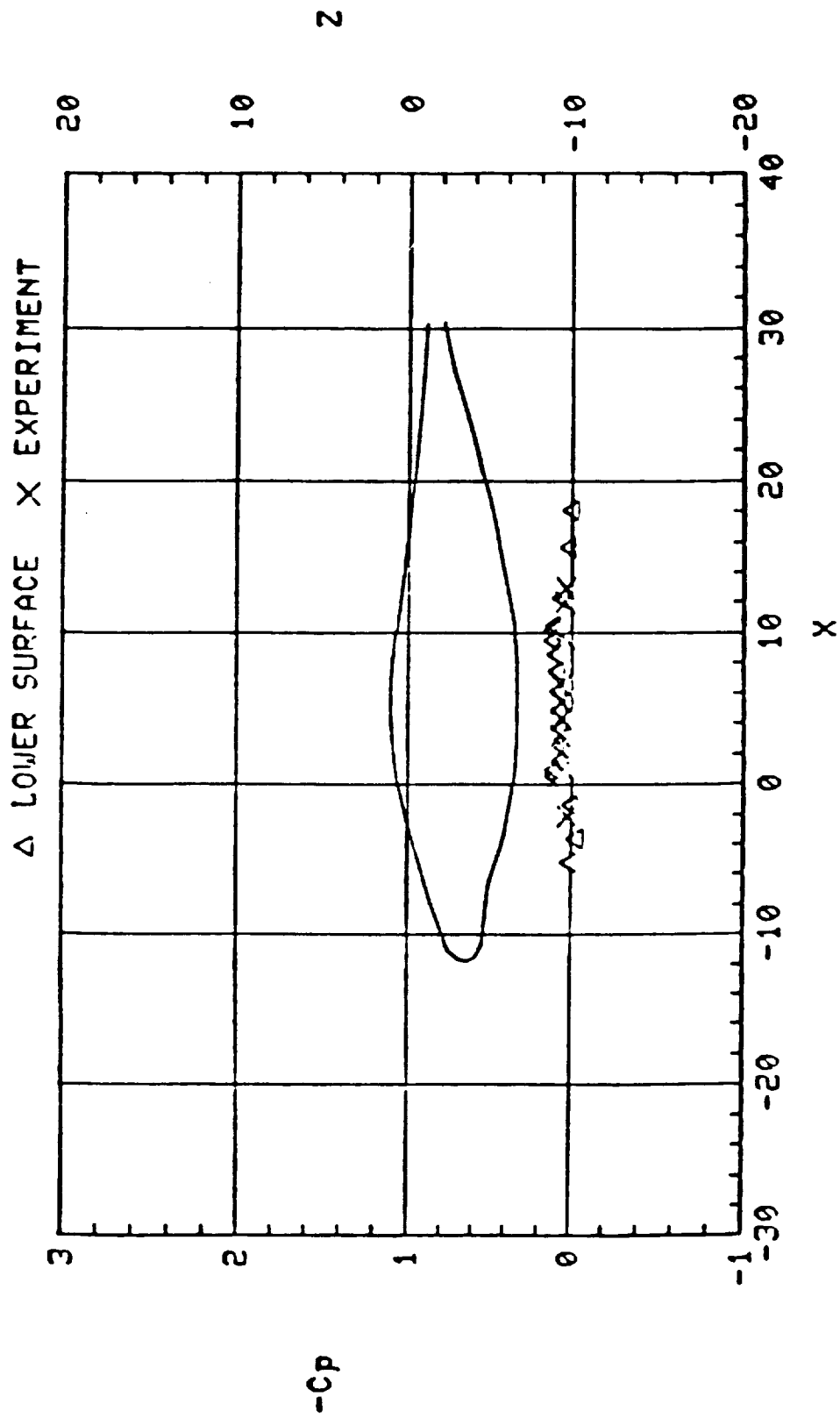
(a)  $C_p$  of Fuselage Bottom at  $Y = 0$

Figure 8. A No-Jet Nozzle Model.



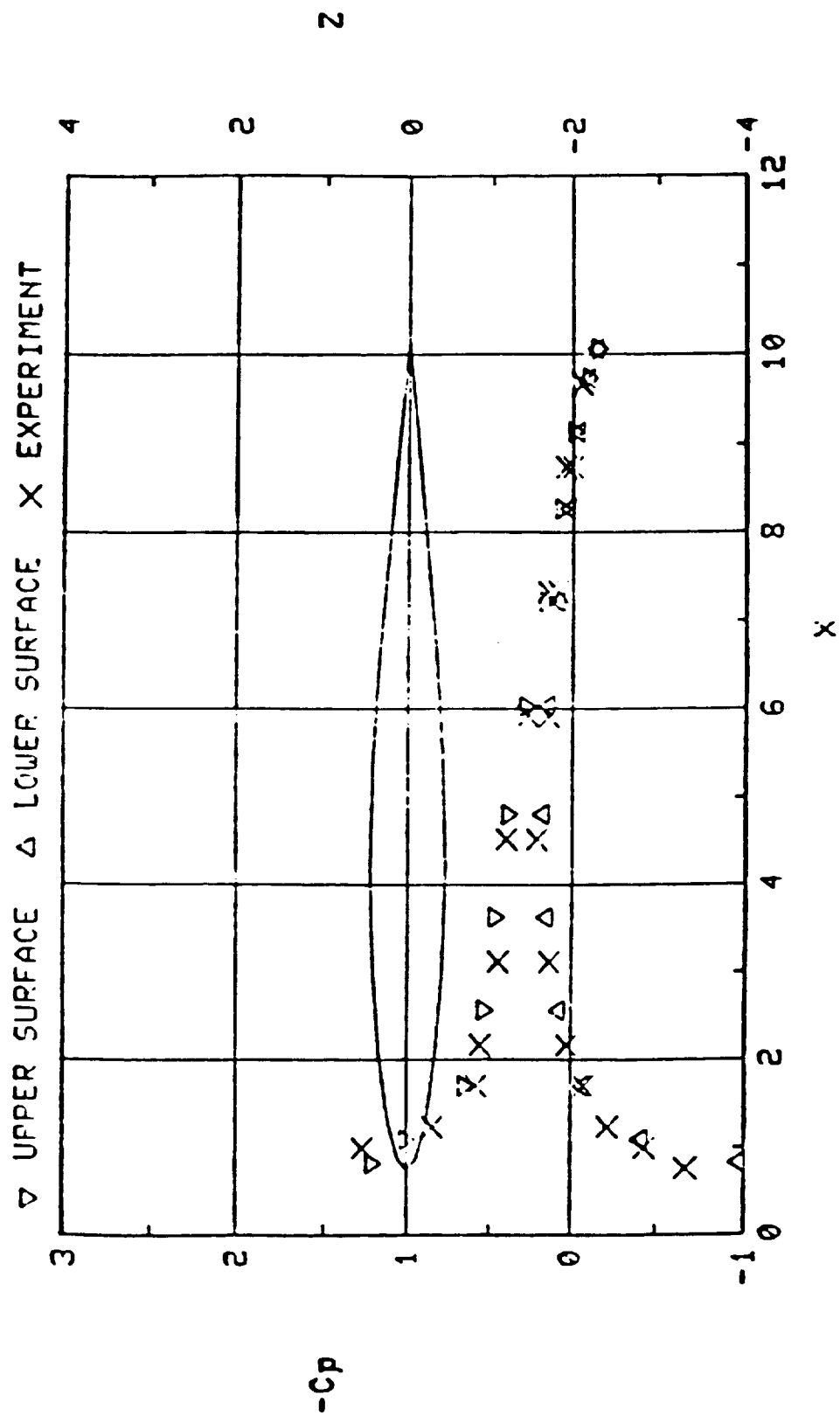
(b)  $C_p$  of Fuselage Bottom at  $Y = 1.25$

Figure 8. Continued.



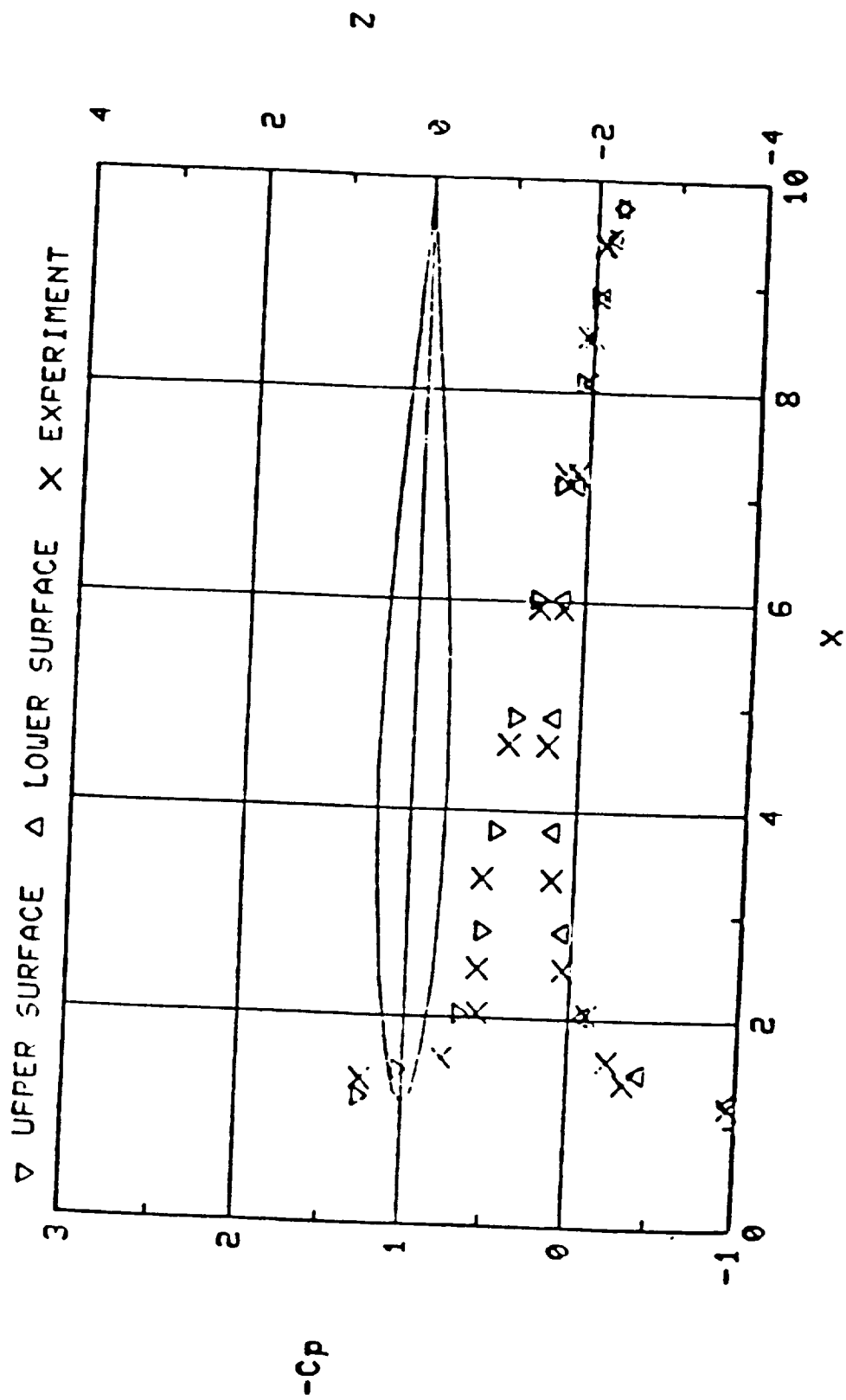
(c)  $C_p$  of Fuselage Bottom at  $Y = 2.0$

Figure 8. Continued.



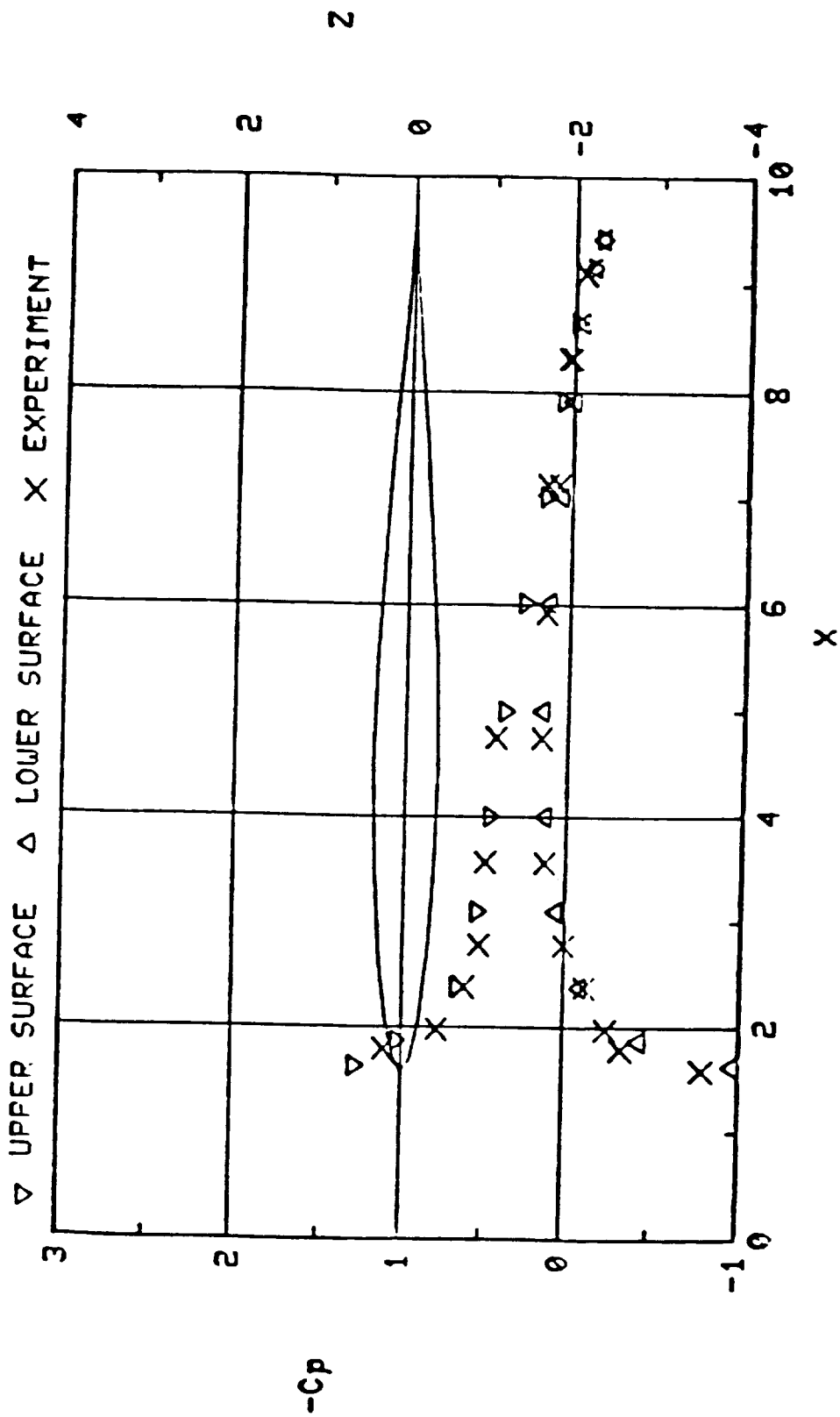
(d)  $C_p$  of Wing Section at  $Y = 5.04$

Figure 8. Continued.



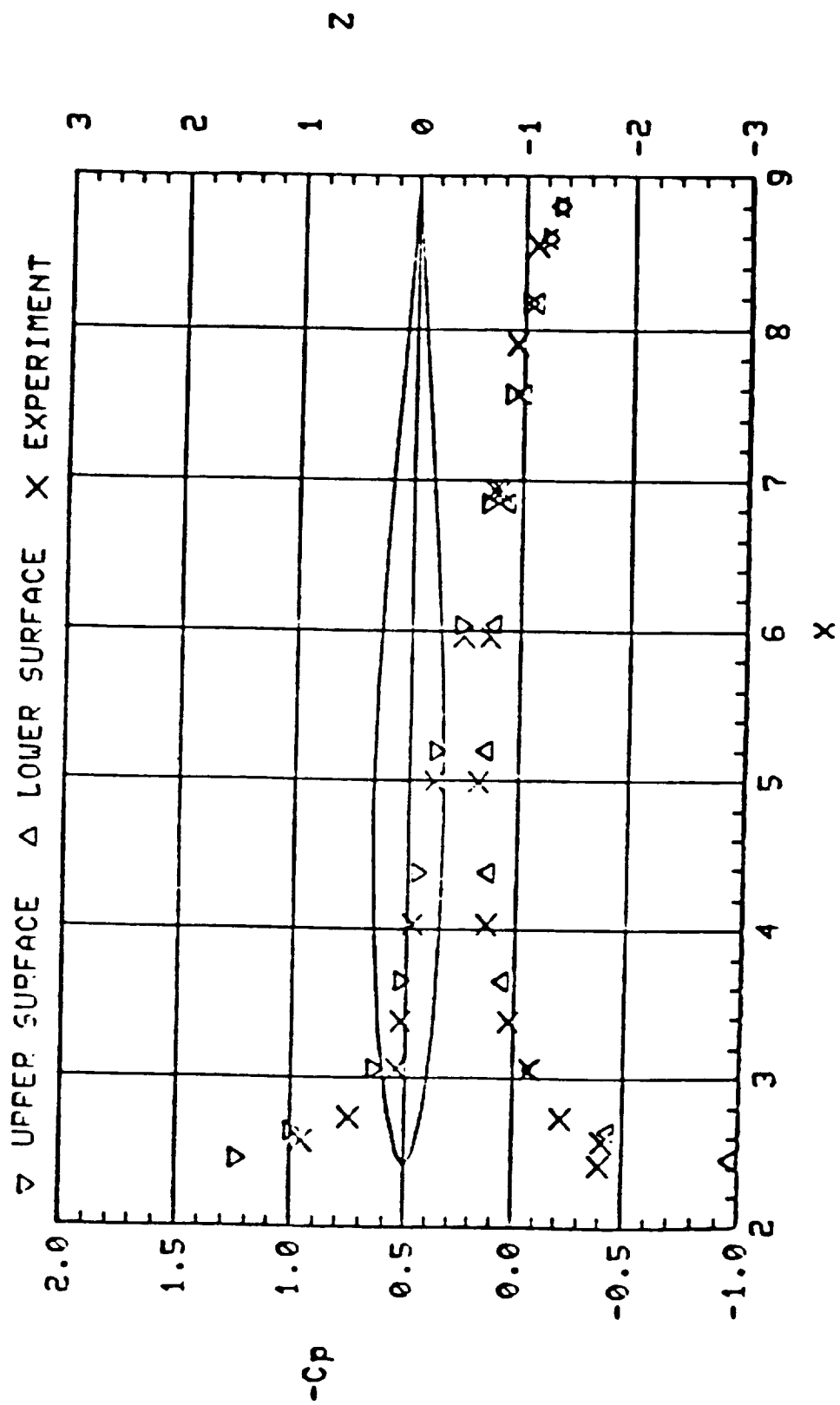
(e)  $C_p$  of Wing Section at  $Y = 7.79$

Figure 8. Continued.



(f)  $C_p$  of Wing Section at  $Y = 10.55$

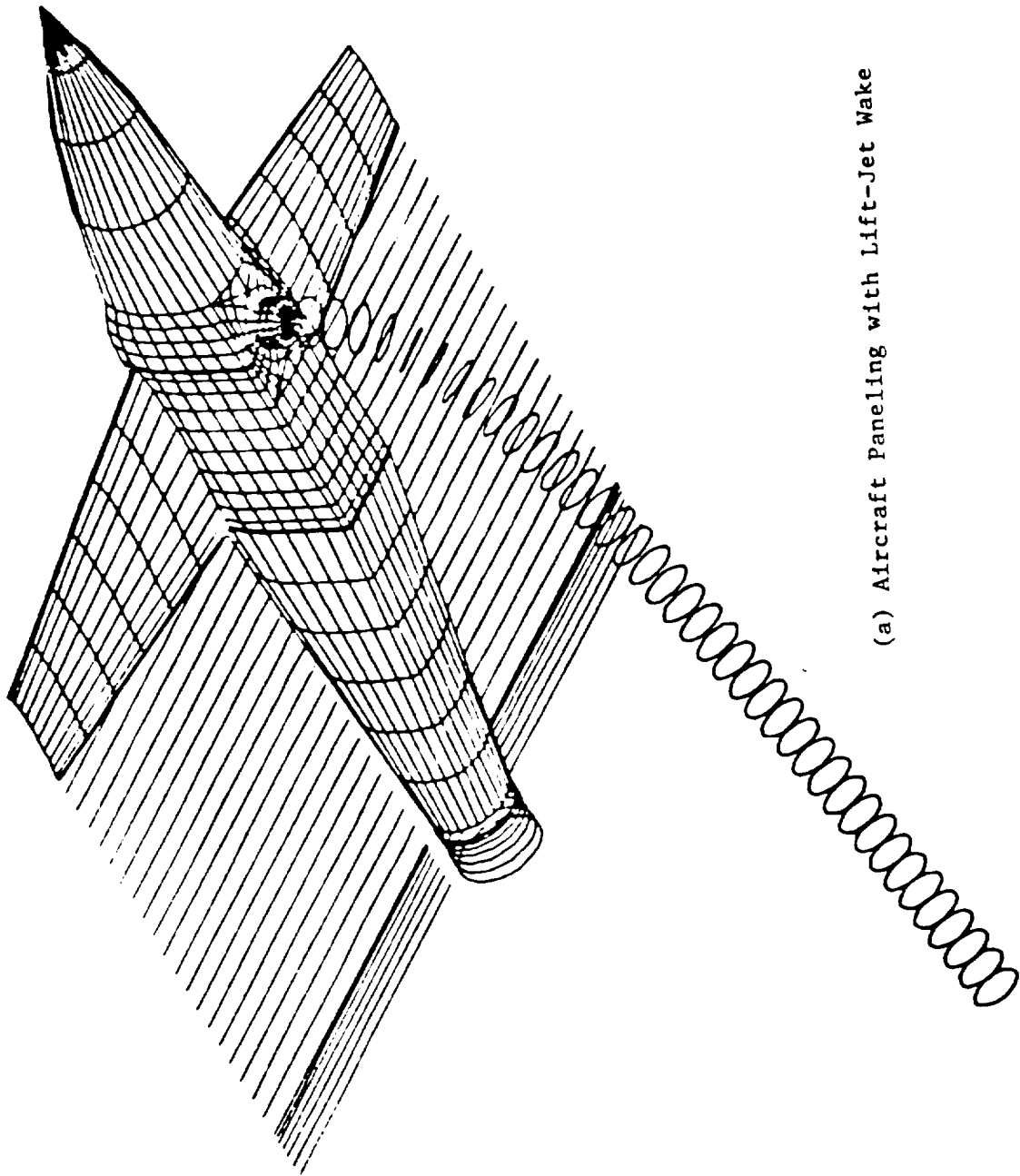
Figure 8. Continued.



(g)  $C_p$  of Wing Section at  $Y = 16.05$

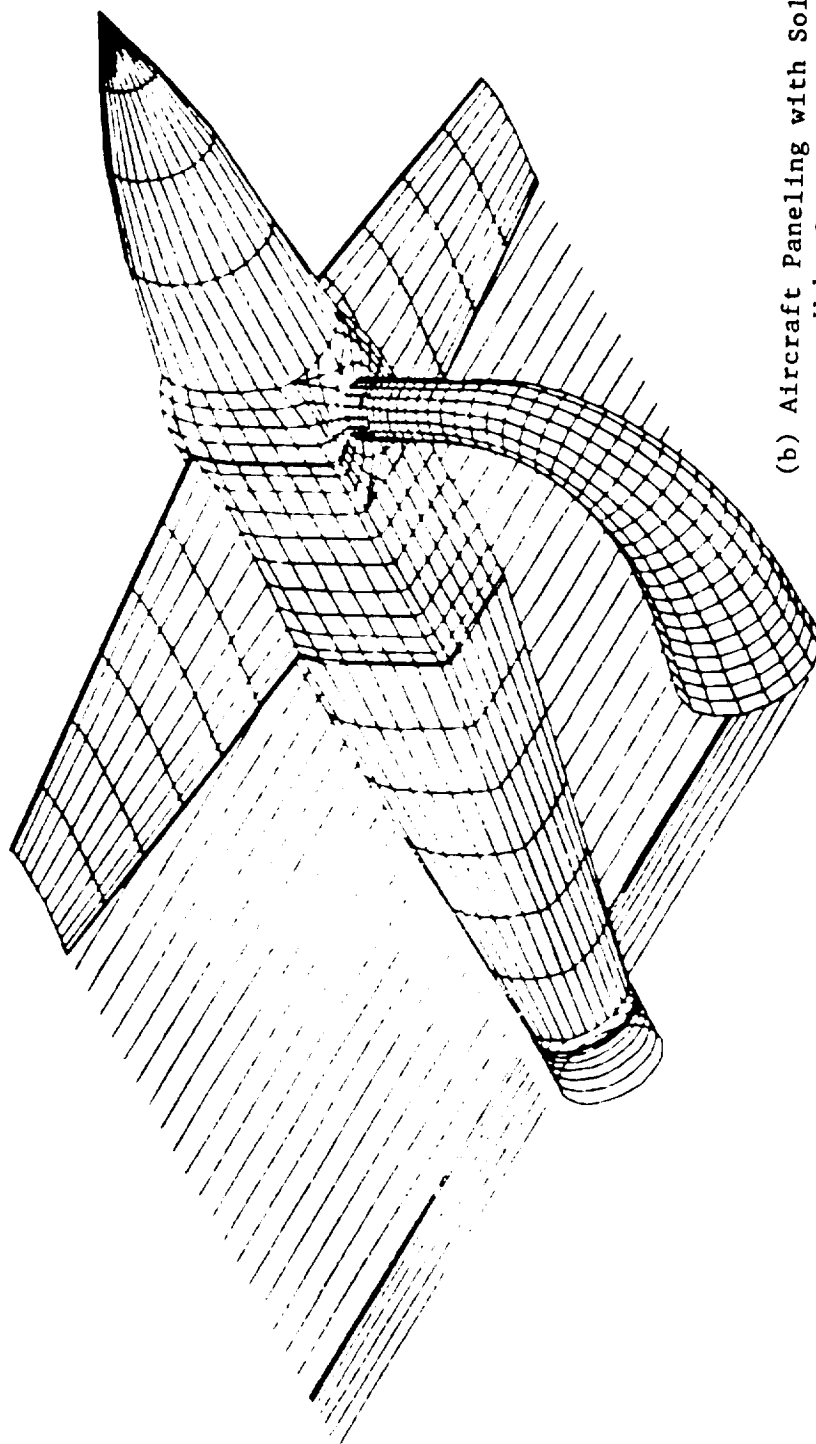
Figure 8. Concluded.





(a) Aircraft Paneling with Lift-Jet Wake

Figure 9. Paneling of Lift-Jet Model.



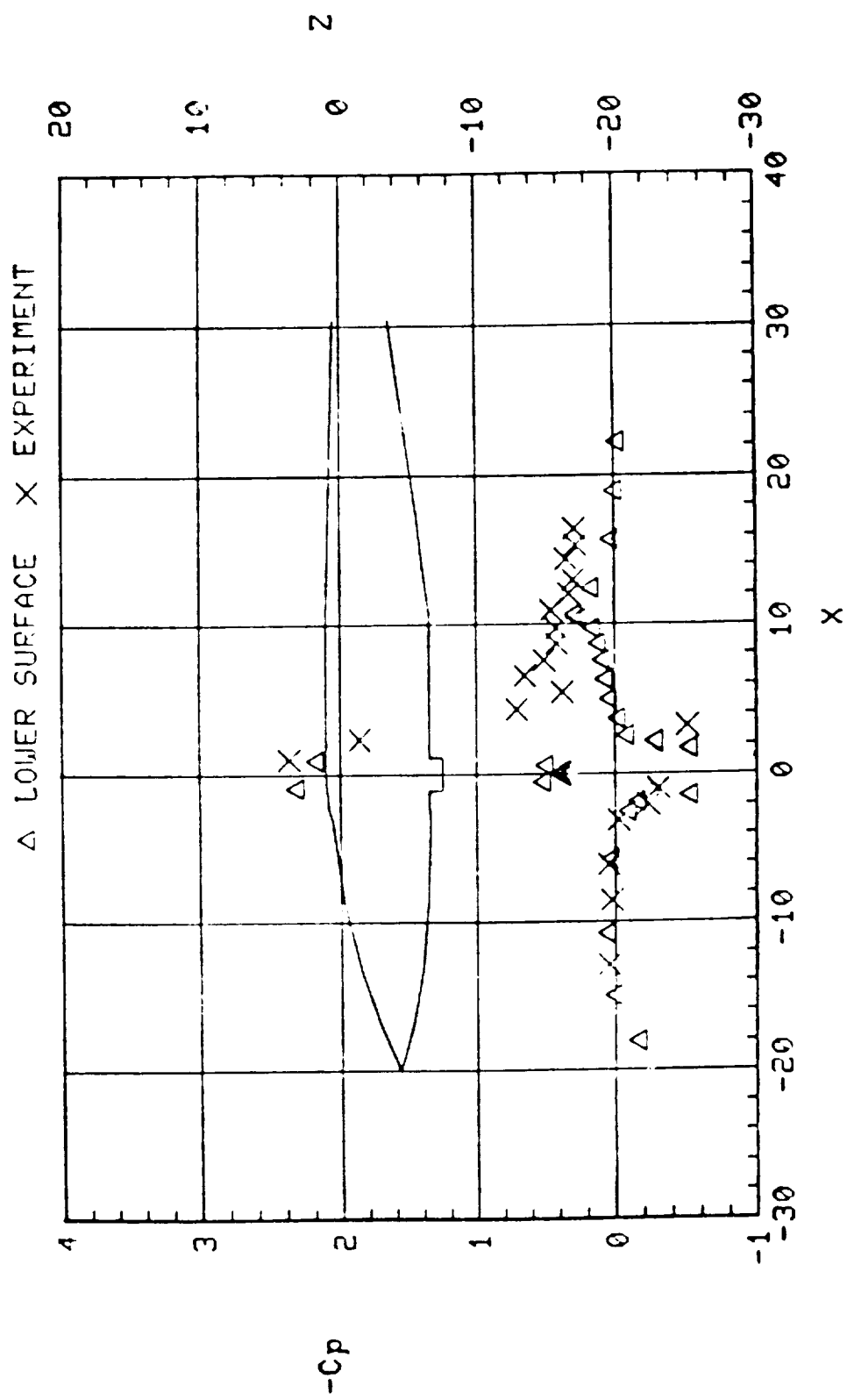
(b) Aircraft Paneling with Solid  
Wake-Jet Surface

Figure 9. Concluded.

from the fact that the configuration taken from the figure shown in Ref. 16 lacks the dimensional details for this purpose. A small extension piece was attached downstream from the jet nozzle to generate a smooth velocity profile around the nozzle. Although some surface pressure disturbances are indicated, a better initial profile at the inlet boundary for the APPL code could be set up. Since the parabolic code, APPL, is marching downstream, it is important to have a good inlet profile to start with.

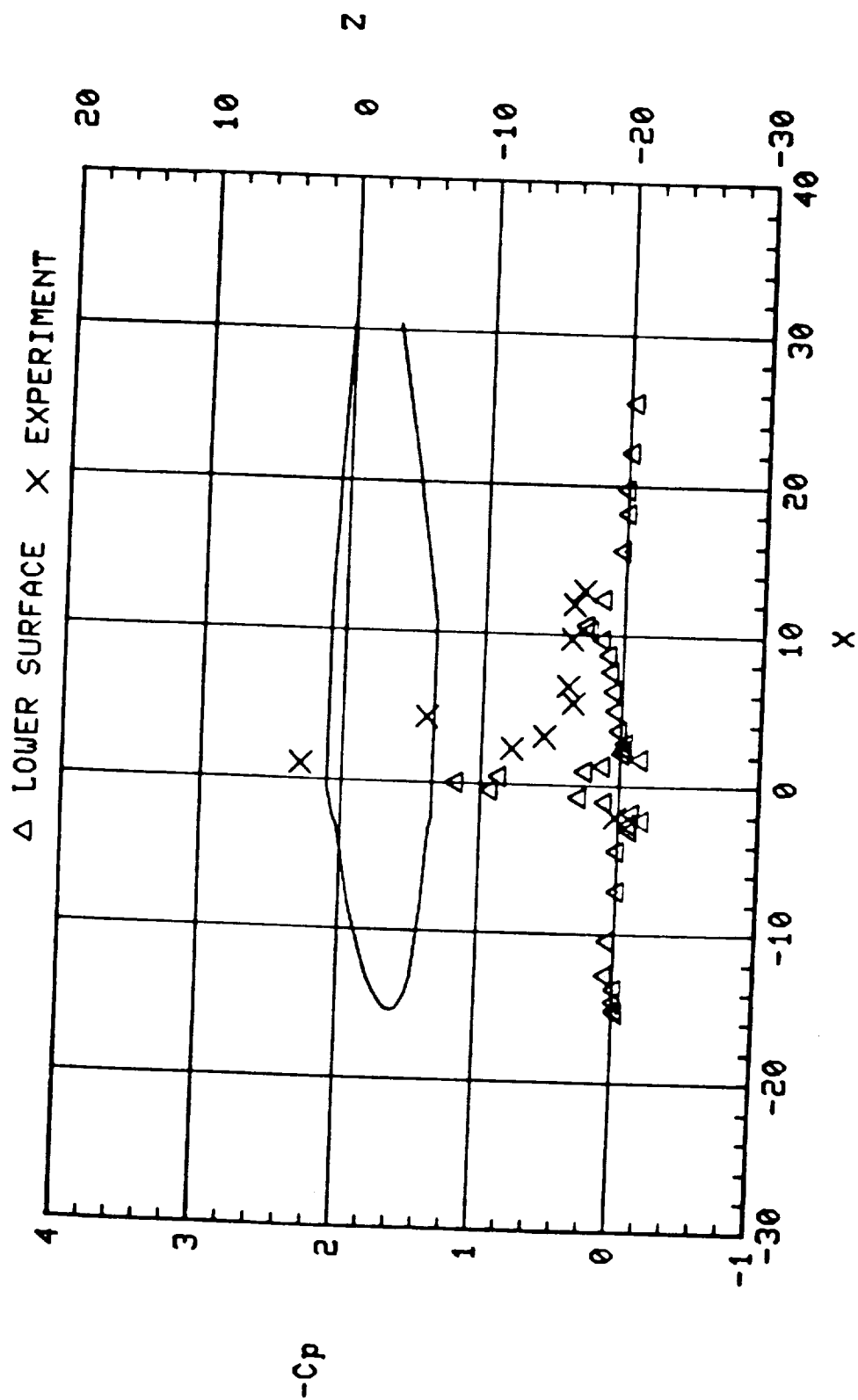
First, a jet-off case with this geometry was run to test the panel distribution and compared with the  $C_p$  data for the jet-on case in Figures 10(a) through (g). This VSAERO-only solution took about 30 seconds of CPU time on the CRAY X-MP 48 at the NASA Ames Research Center. Disturbances are noticeable around the jet nozzle area and rear fuselage in Figures 10(a), (b) and (c). In Figures 10(d) through (g) for wing sections in the spanwise direction, comparison of  $C_p$  data on the surface is excellent due to the use of an exact geometry, the NACA 63A010 airfoil. As expected, the results on the wing sections farther away from the fuselage give better agreement; i.e., less disturbance is felt.

Then the lift-jet case for  $V_j/V_o = 4.878$  was run with approximately one minute of CPU time per iteration for the VSAERO calculation and with 10 minutes of CPU time per iteration for the APPL calculation. Three iterations between the VSAERO and APPL codes were performed but no discernible change in the boundary conditions of either VSAERO or the APPL codes or the predicted aerodynamic data at the experimental points was observed beyond the second iteration. The jet at  $90^\circ$  presented a significant problem to the APPL marching solution procedure since the initial plane did not have a free stream velocity component pointing in the same direction as the jet velocity. This was remedied by overriding the w-component with a small negative value. It was then possible to march the solution downstream until the jet centerline was parallel to the free stream, where the run was terminated. The coupled solution was essentially converged after three iterations. It seems that no more than 2 iterations are necessary between two codes in this class of problems. From Figures 11(a) through (i) the comparison between computation and experiment for the lift-jet-only case is shown. Figure 11(a) shows  $C_p$  distributions along the centerline. Results on the fore fuselage show better agreement than on the rear fuselage, where jet entrainment plays a more important role; i.e., on the leeward side of the jet. Figures 11(b) and (c) show  $C_p$  at  $y = 1.25$  and  $y = 2.00$ , respectively. Suction pressure at the bottom of the fuselage is overpredicted, which may be partly attributable to the sparsity of geometry definition in the forebody and nacelle area; i.e., panel modeling is approximate in these areas. Figures 11(d) through (g) show  $C_p$  distributions on 4 different wing sections and the same order of accuracy as in Figures 8(d) through (g) is presented. Major discrepancies for  $C_p$  on the wing sections lie at the very leading edge where  $C_p$  is sensitive to the paneling density. The streamwise velocity contours at the last station are shown in Figure 11(h). The roll-up of the jet is more substantial than the  $60^\circ$  case. A strong vortex pair is indicated by the cross-flow vector field in Figure 11(i).



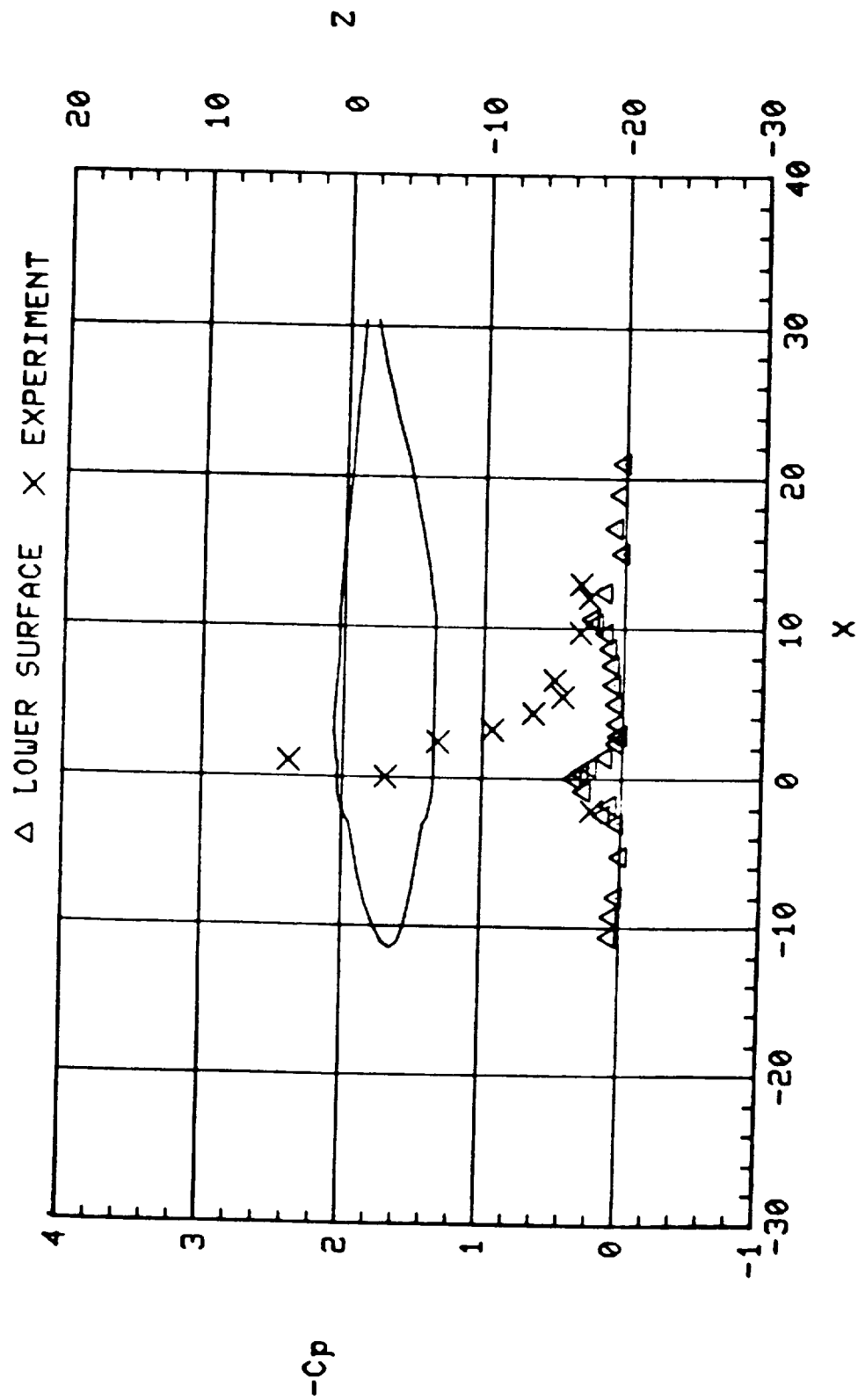
(a)  $C_p$  of Fuselage Bottom at  $Y = 0.0$

Figure 10. Jet-Off Case.



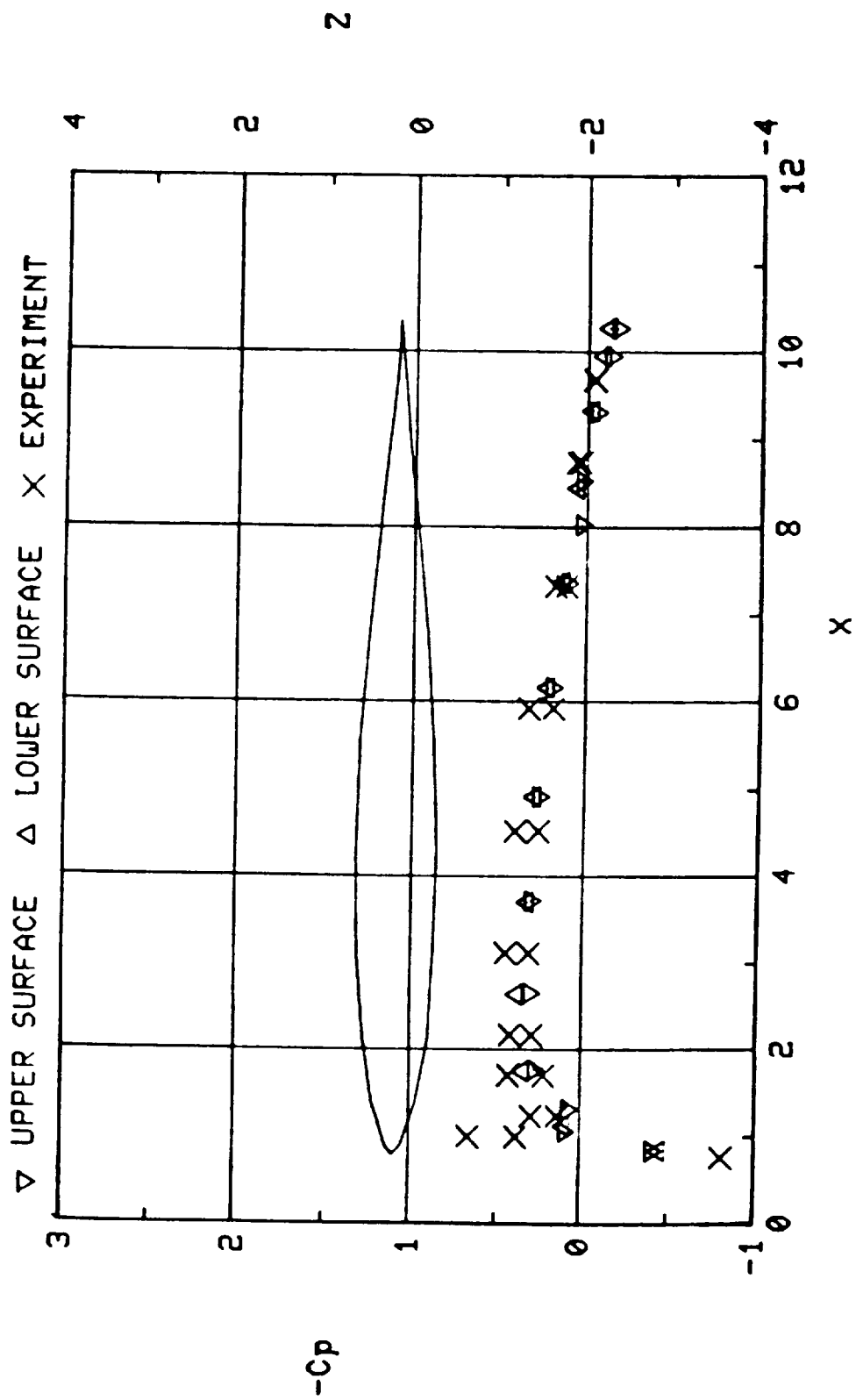
(b)  $C_p$  of Fuselage Bottom at  $Y = 1.25$

Figure 10. Continued.



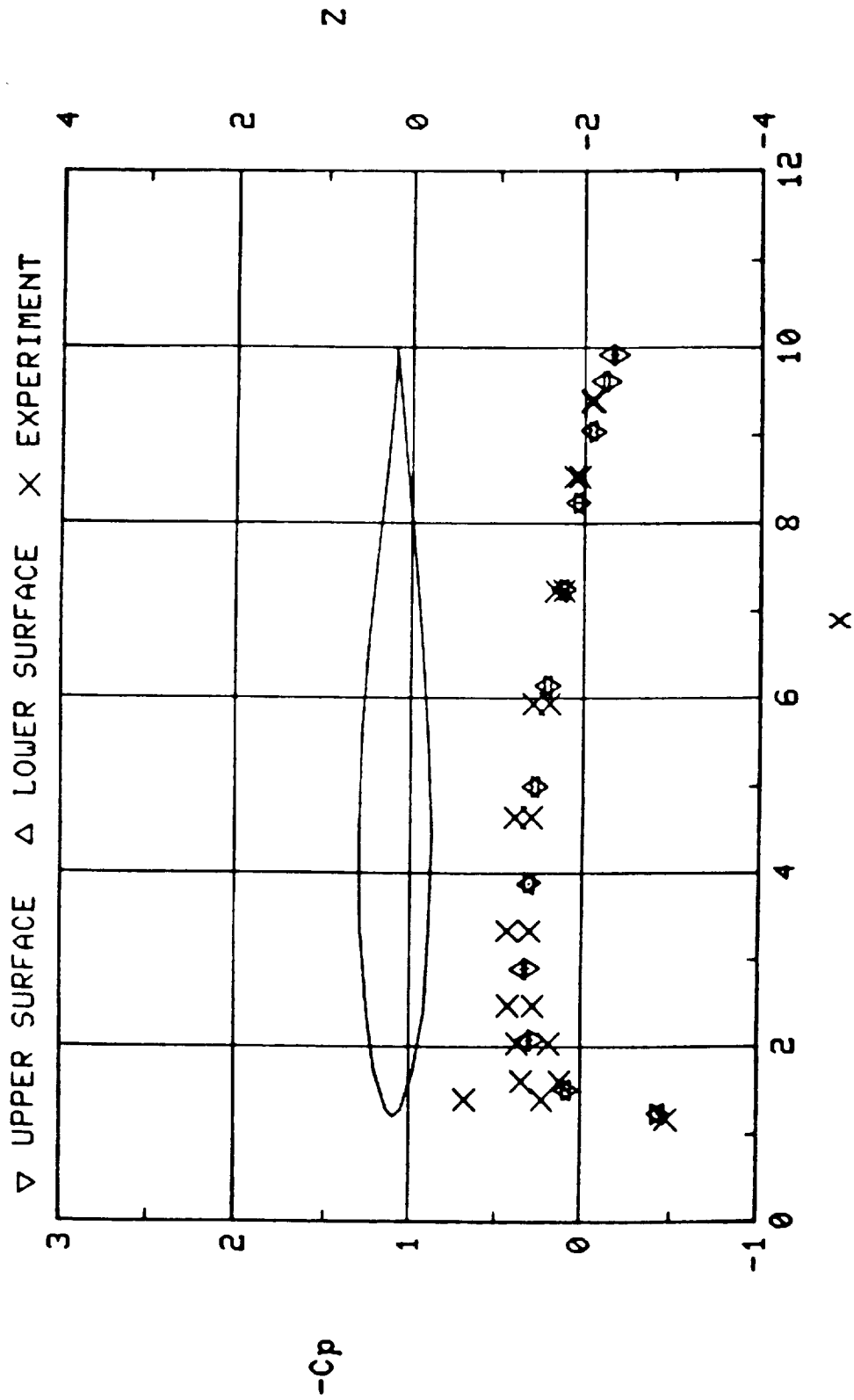
(c)  $C_p$  of Fuselage Bottom at  $Y = 2.0$

Figure 10. Continued.



(d)  $C_p$  of Wing Section at  $Y = 5.04$

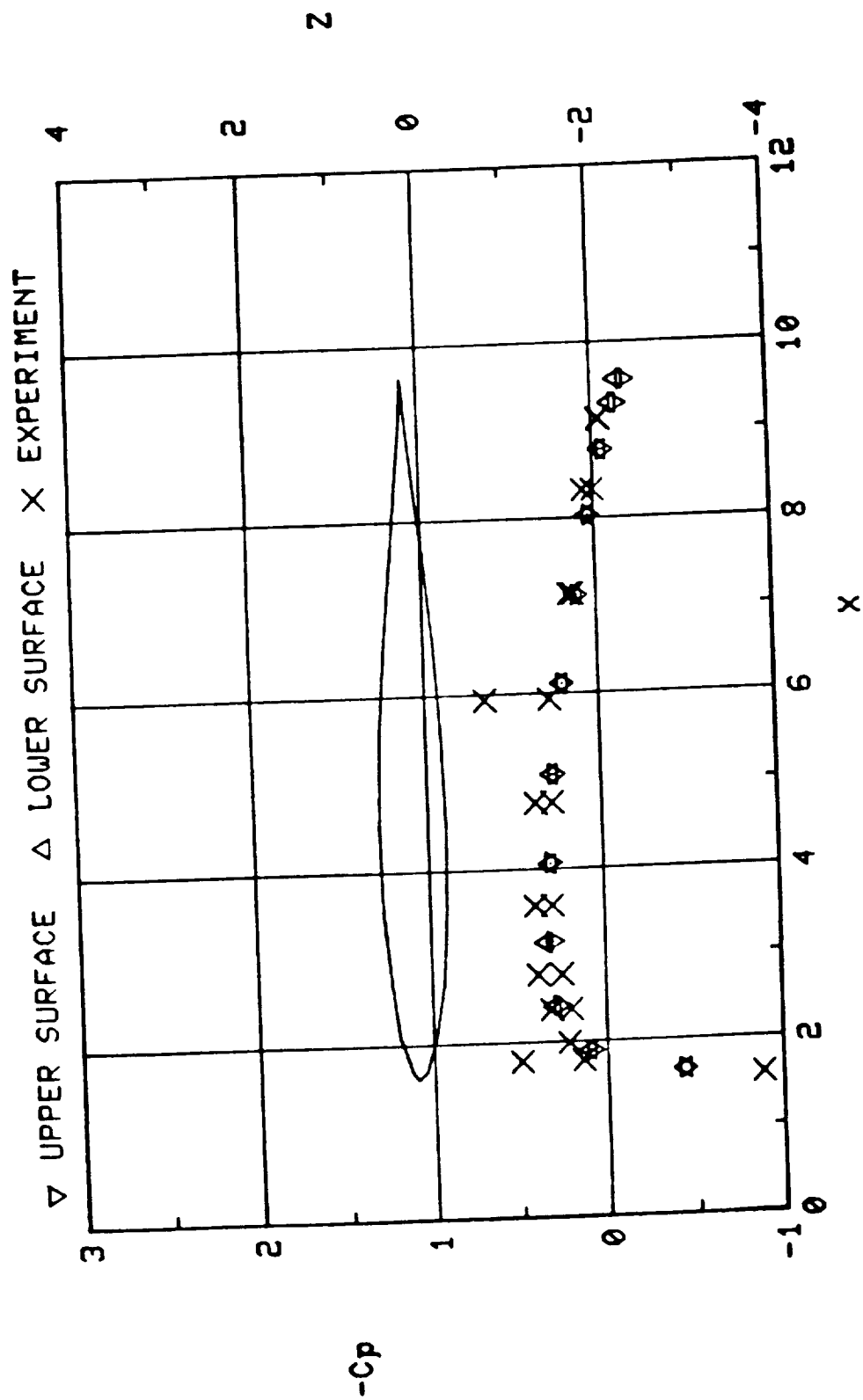
Figure 10. Continued.



(e)  $C_p$  of Wing Section at  $Y = 7.79$

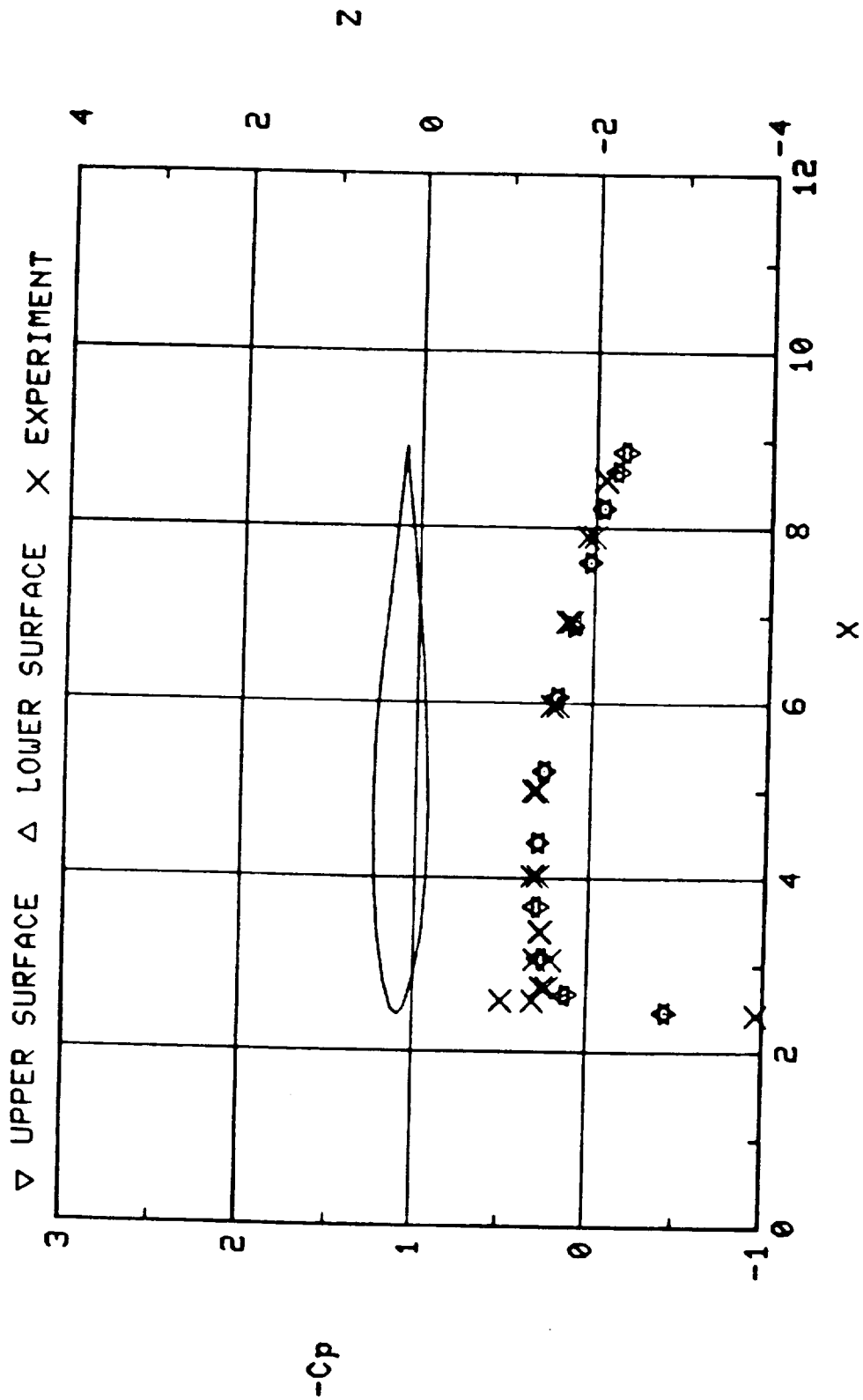
Figure 10. Continued.





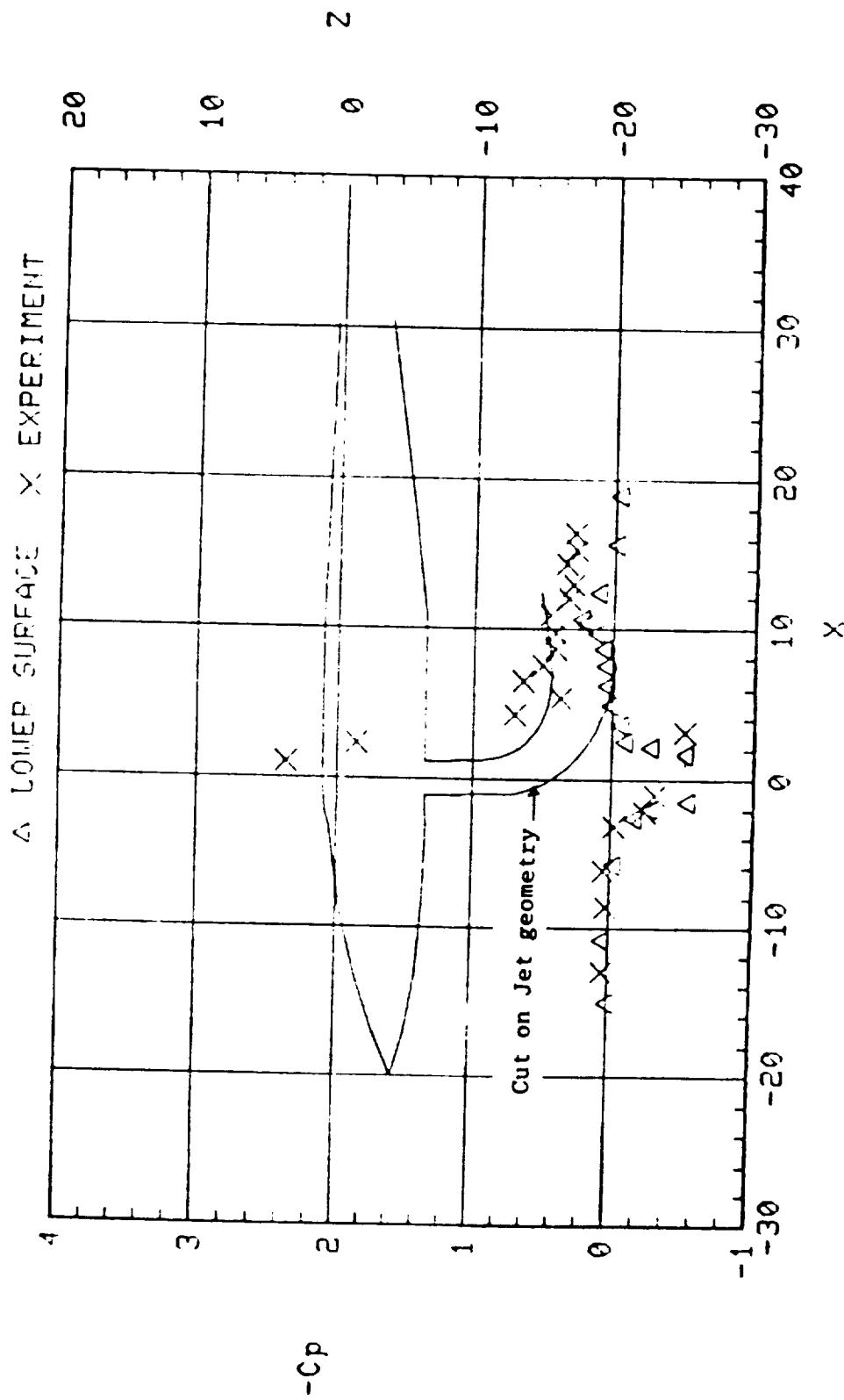
(f)  $C_p$  of Wing Section at  $Y = 10.55$

Figure 10. Continued.



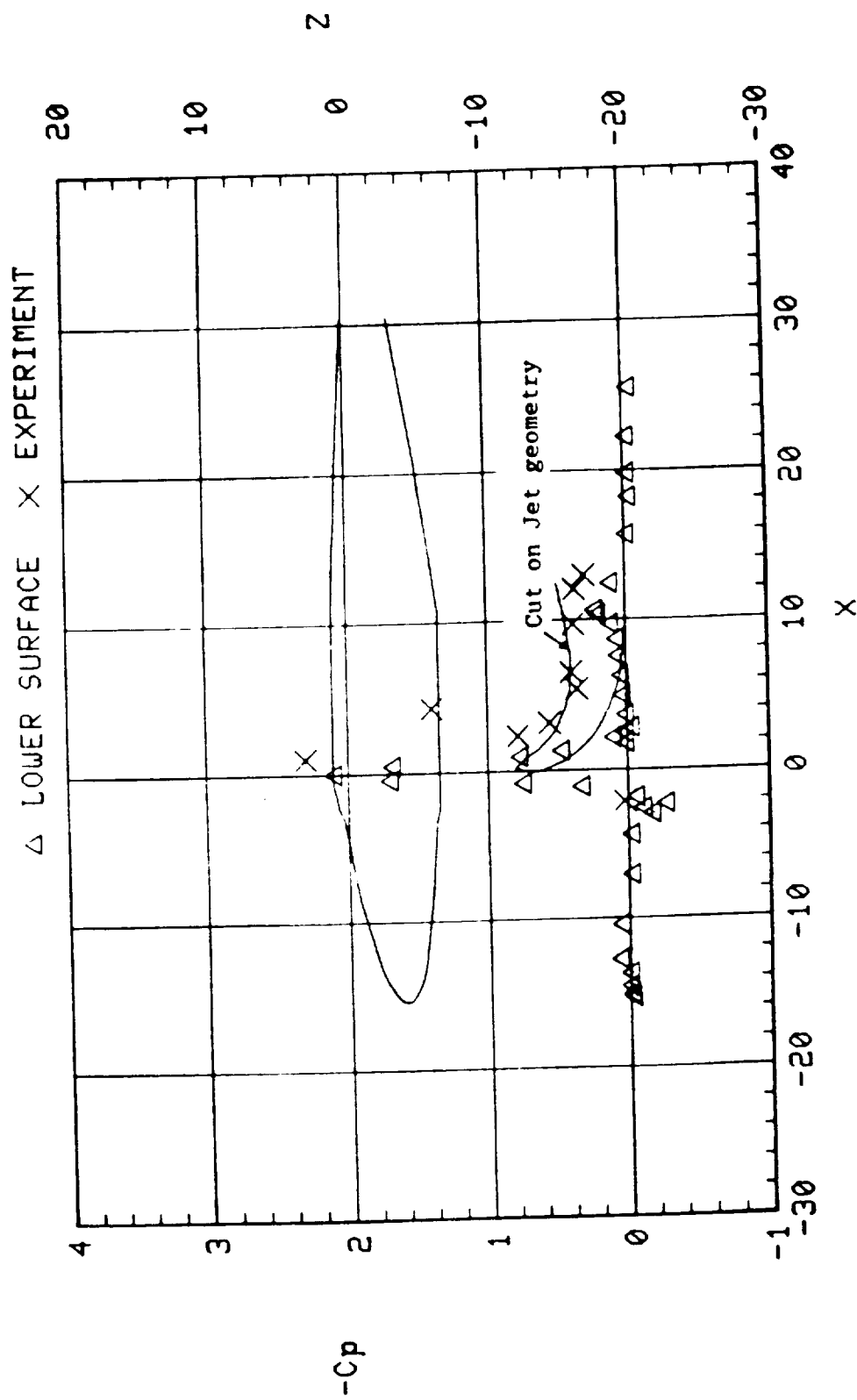
(g)  $C_p$  of Wing Section at  $Y = 16.05$

Figure 10. Concluded.



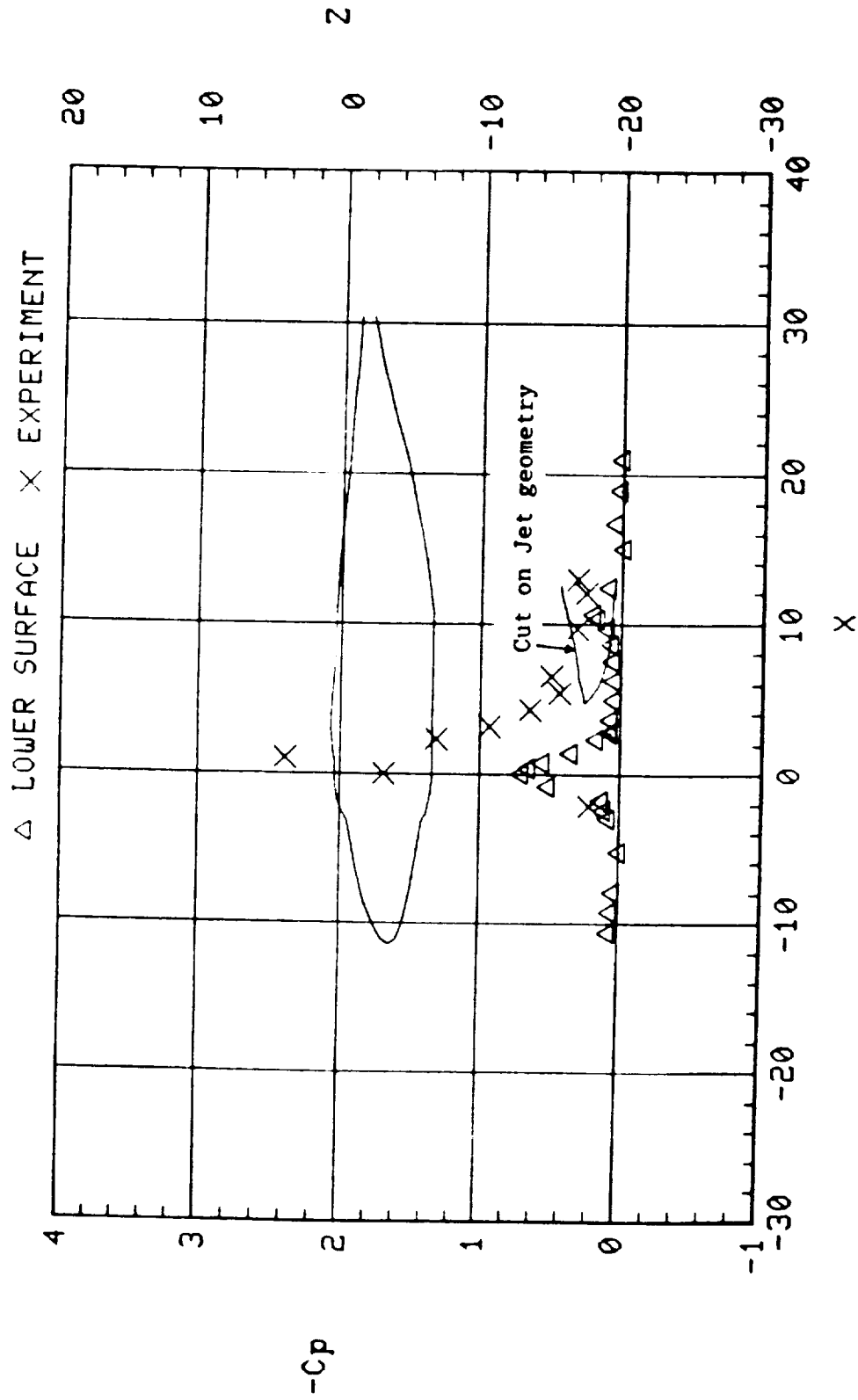
(a)  $C_p$  of Fuselage Bottom at  $Y = 0.0$

Figure 11. A Lift-Jet-On Case:  $V_j/V_o = 4.878$ .



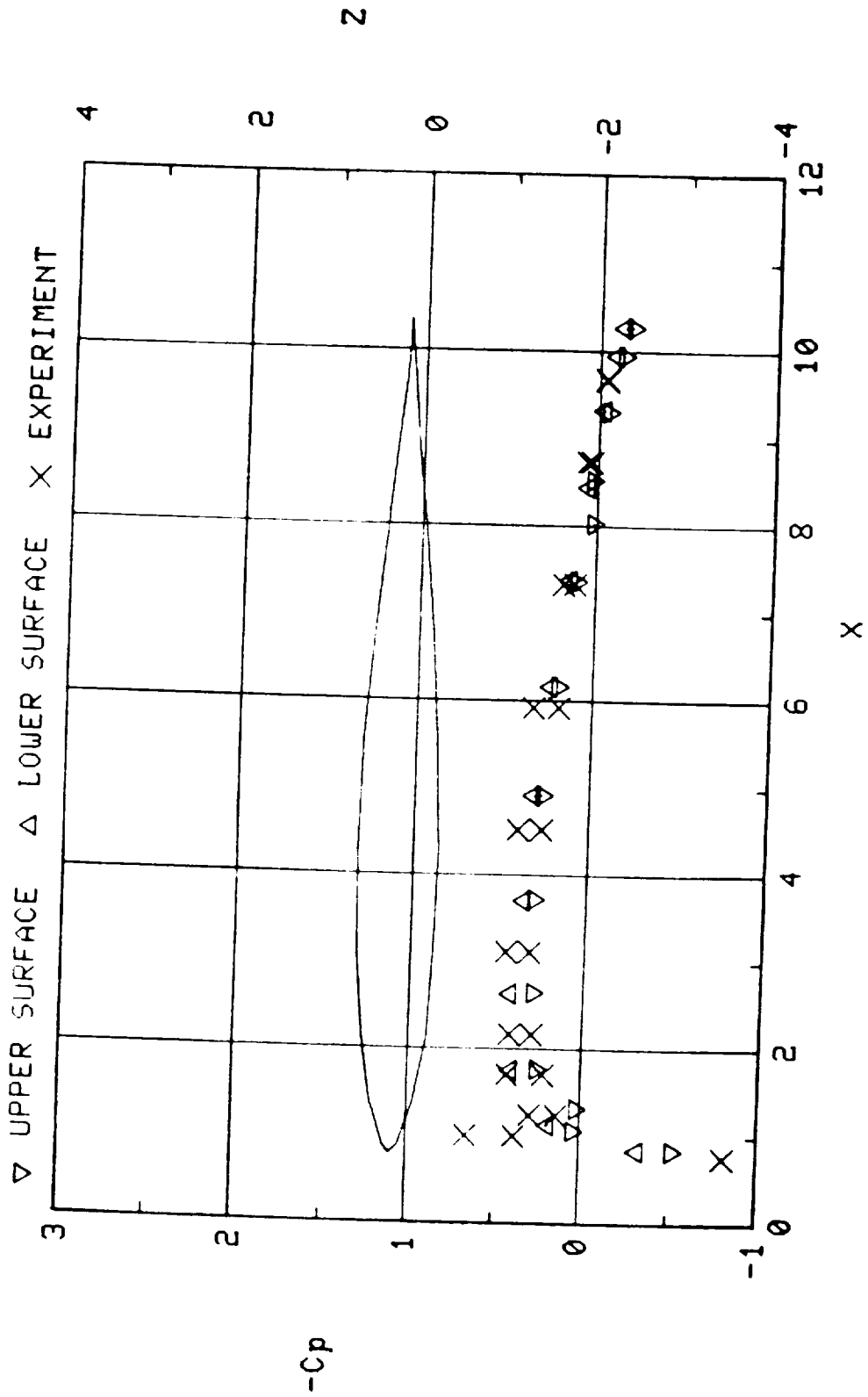
(b)  $C_p$  of Fuselage Bottom at  $Y = 1.25$

Figure 11. Continued.



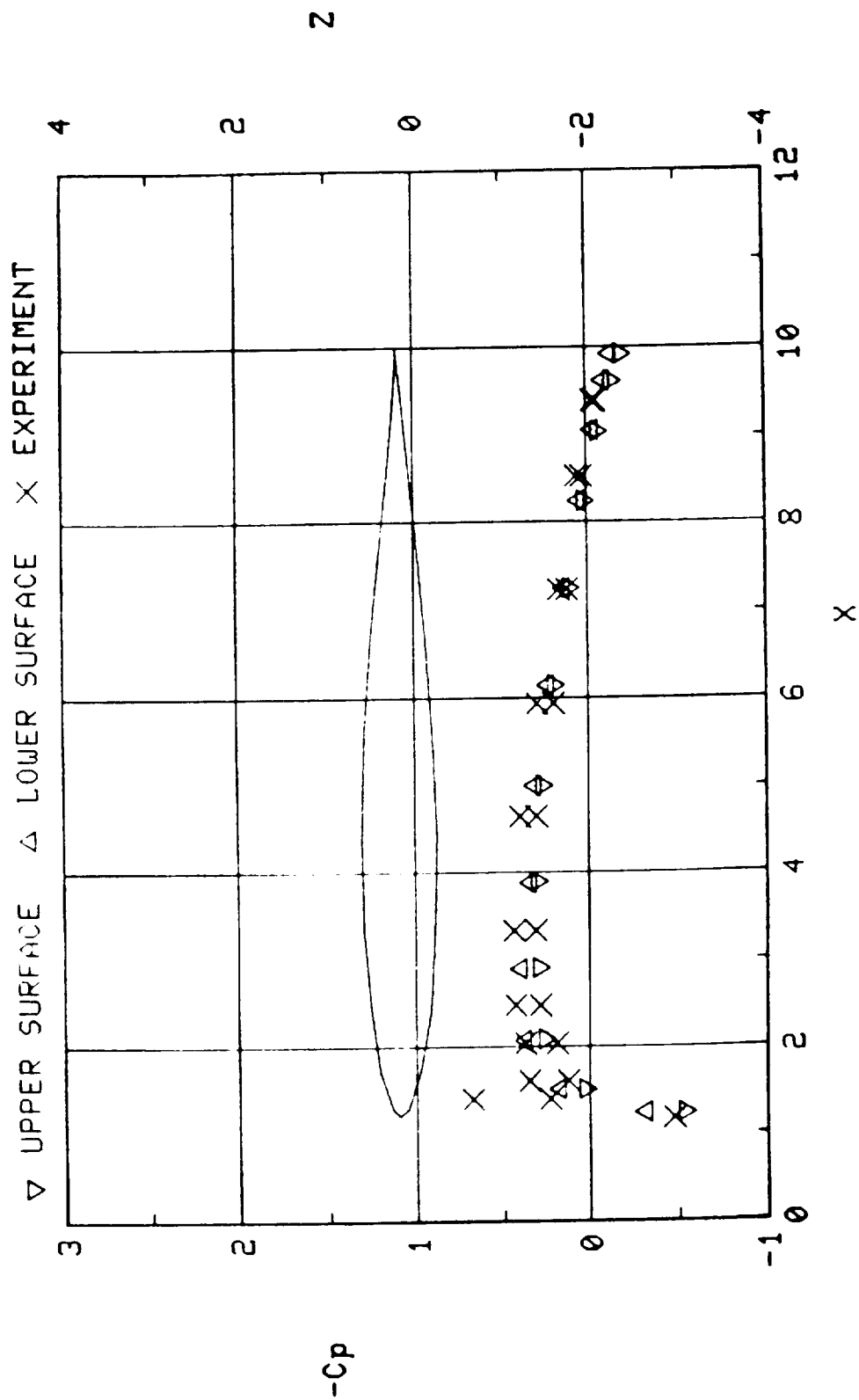
(c)  $C_p$  of Fuselage Bottom at  $Y = 2.0$

Figure 11. Continued.



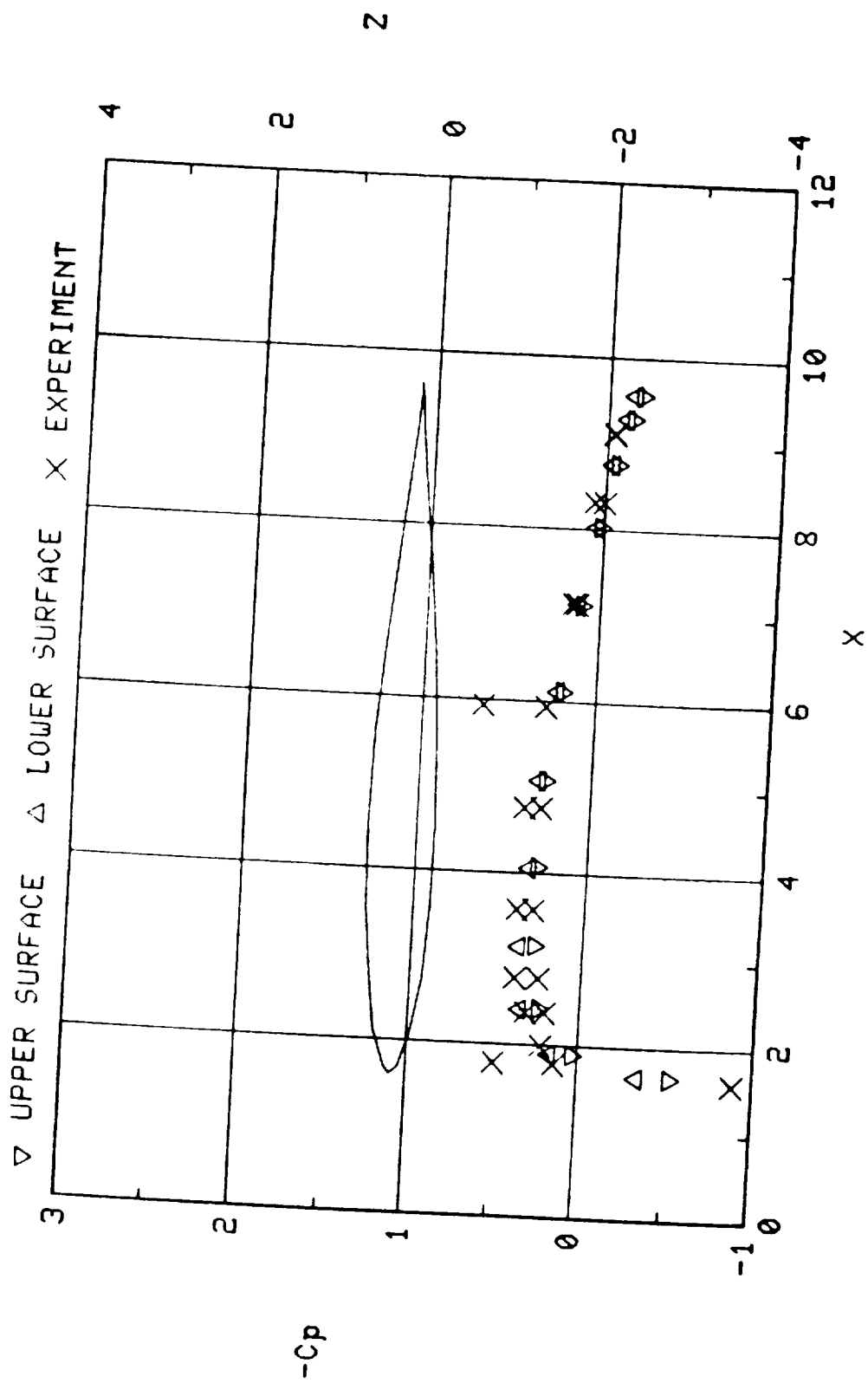
(d)  $C_p$  of Wing Section at  $Y = 5.04$

Figure 11. Continued.



(e)  $C_p$  of Wing Section at  $Y = 7.79$

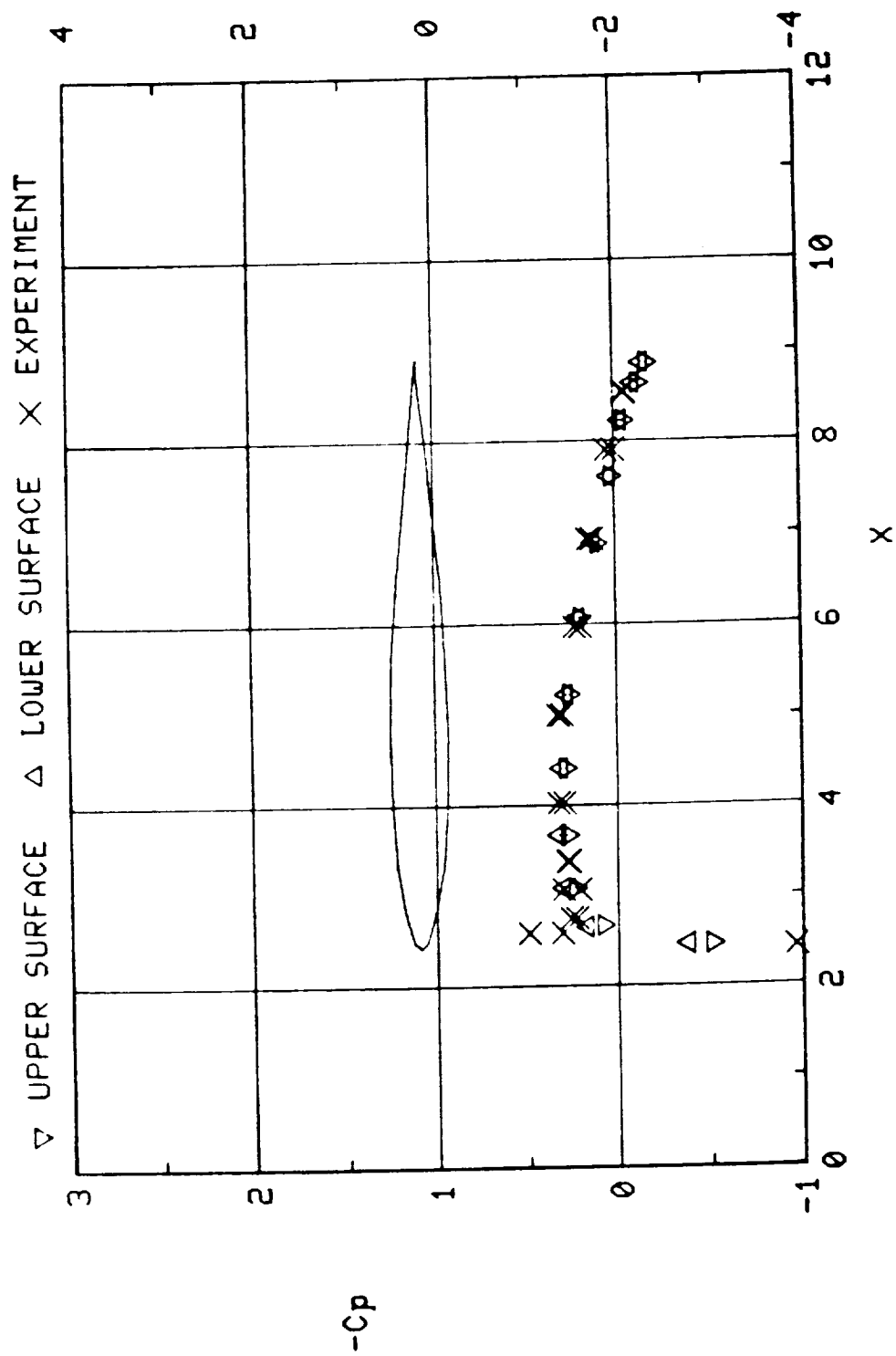
Figure 11. Continued.

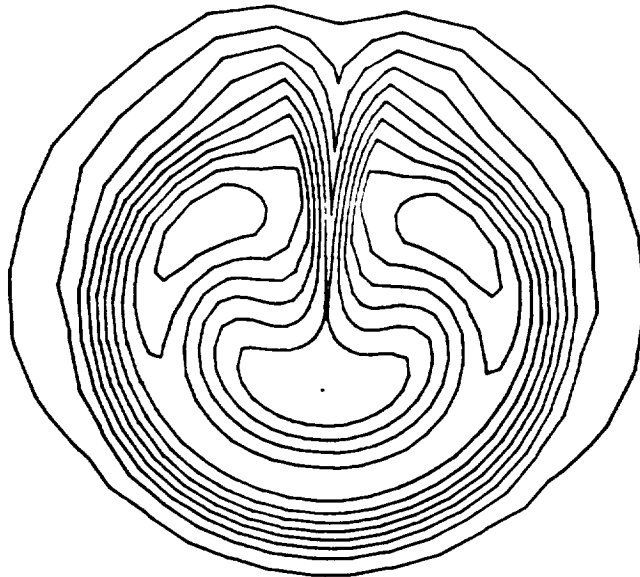


(f)  $C_p$  of Wing Section at  $Y = 10.55$

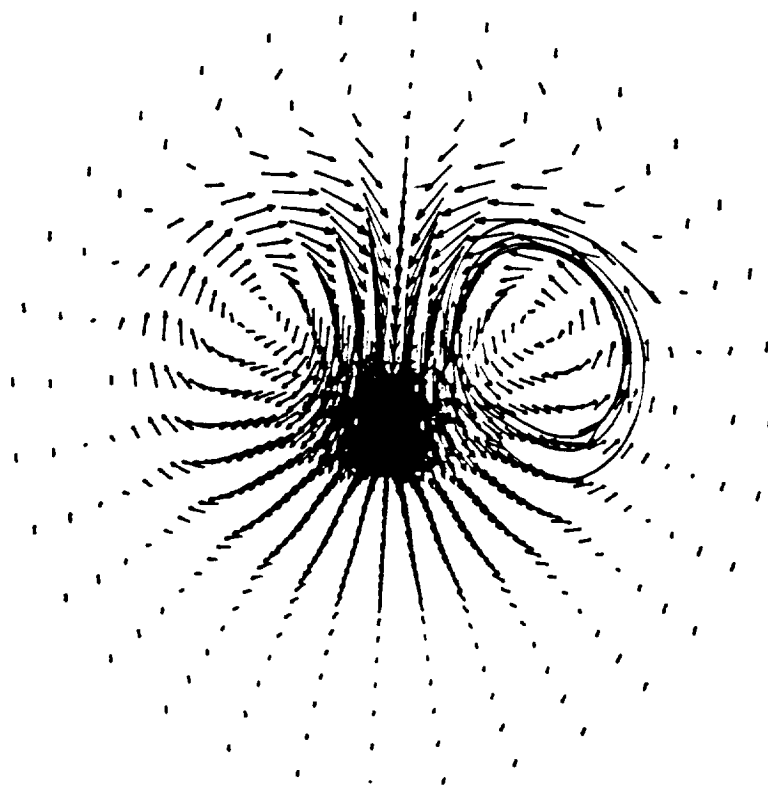
Figure 11. Continued.







(h) Streamwise Velocity Contours at  $90^\circ$  Incidence



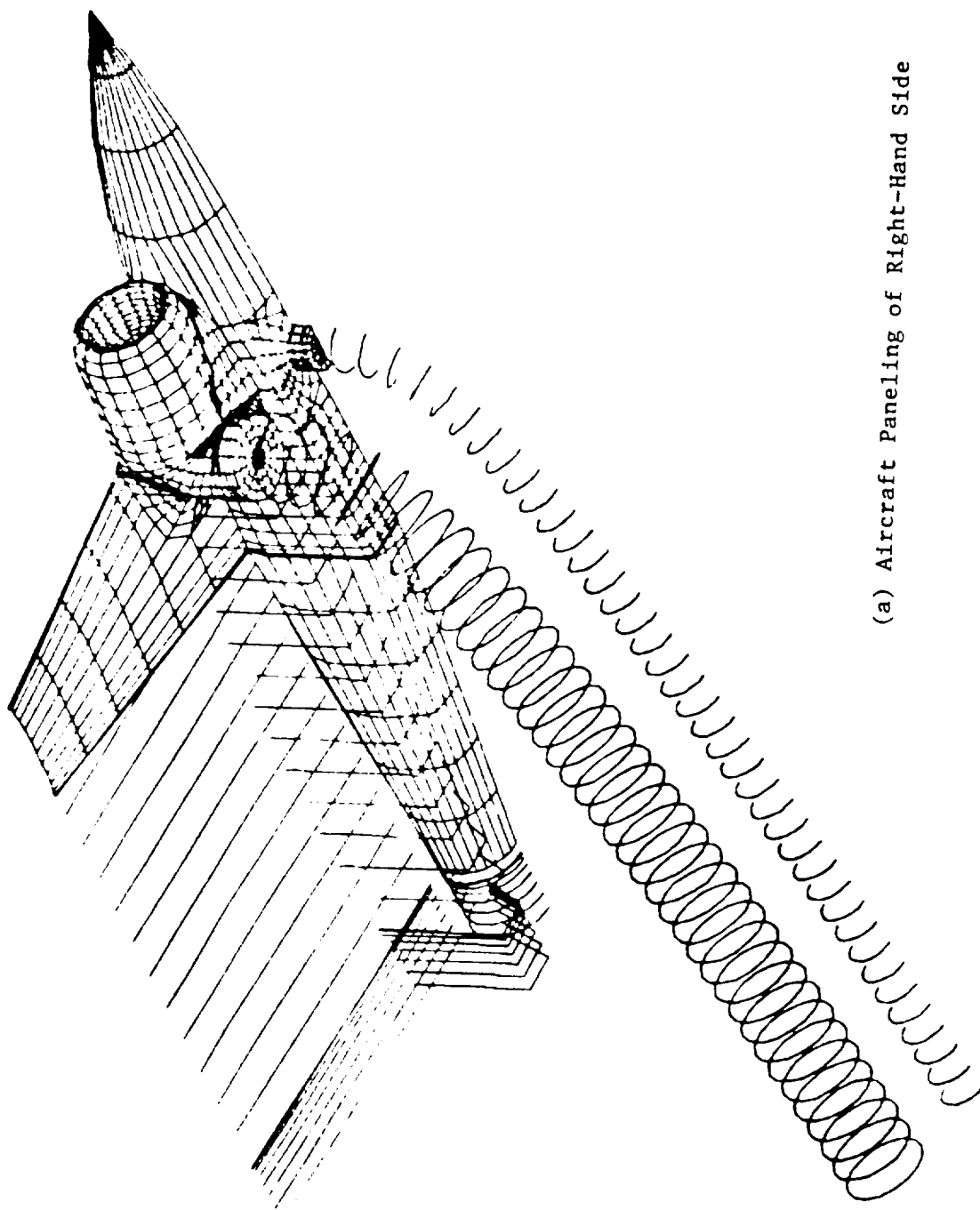
(i) Cross-Flow Velocity Vectors at  $90^\circ$  Incidence

Figure 11. Concluded.

#### 4.4 A Vectored-Thrust Model with Lift-Jet

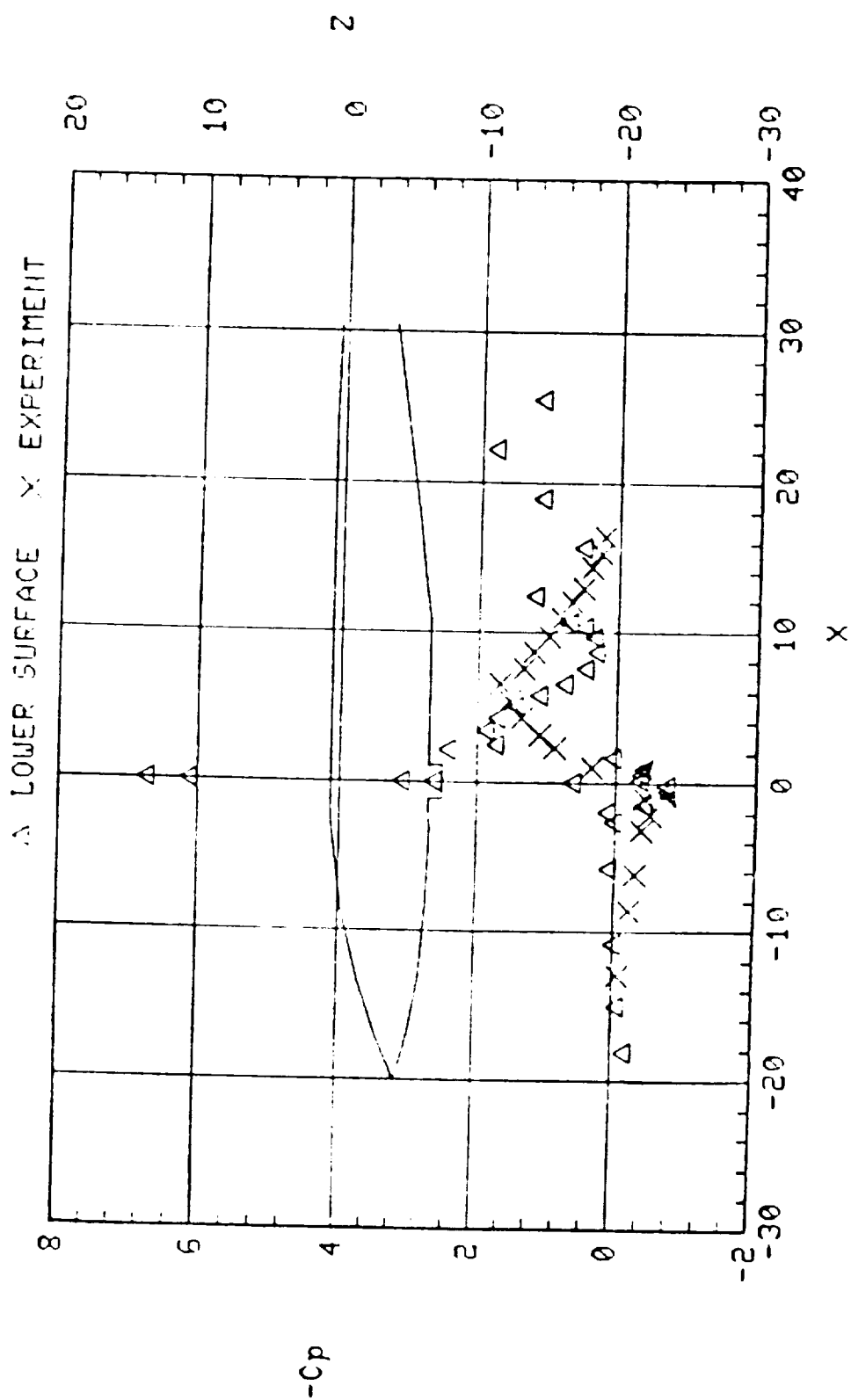
Computation was made for a front vectored-thrust model with the lift-jet for  $90^\circ$  exit deflection angle. The aerodynamic condition is  $V_j/V_o = 3.534$  with no angle of attack. The geometry has been considerably modified from the lift-jet-only geometry to include the front vectored-thrust nacelles underneath the wing. Substantial fairing is applied to streamline the pylon and other connecting parts to prevent the abrupt separation of the flow. Where the separation of flow is expected, the wake is attached to describe the vortex shedding. Figure 12(a) shows the paneling of the geometry with jets ejected from both the lift jet and vectored nozzle. A total of 2,038 panels were used. Among these, 1,246 panels represent the aircraft geometry in one side of the symmetry plane. 264( $8 \times 33$ ) panels for the lift-jet and 528( $16 \times 33$ ) panels for the thrust jet, respectively, were used. Computing time for the 2,038 panel body with only the VSAERO calculation was approximately 5 minutes of CPU time per iteration on the CRAY X-MP 48 at the NASA Ames Research Center.

Four iterations were made between the VSAERO and APPL codes in which the jet characteristics such as trajectory and cross flow were updated subject to the new boundary condition. At first this entire aircraft configuration with the jet wake model for both jets was run by VSAERO to provide the boundary conditions for the jet plumes analysis by APPL. Regular wakes emanate from the trailing edge of the wings, fuselage and pylon. Jet wakes are generated following Margason's jet trajectory (12). Figures 12(b) through (h) show the  $C_p$  distributions on the fuselage and the wing sections compared with experiment. It was discovered that the  $C_p$  fluctuation in Figures 12(b), (c) and (d) on the rear fuselage part was caused by strong vortex shedding from the pylon. Also,  $C_p$  values on the wing sections shown in Figures 12(e) and (f) are not in good agreement with experimental data. This is a direct consequence resulting from the lack of definition of the nacelle/wing/fuselage fairing, which leads to an approximate panel representation of the body surface. In Figures 12(b) and (h) it is noted that, in the experiment, the negative loading is shown at beyond 5 to 25% of the chord length, different from the current calculation showing the overall negative loading for the entire wing section. Both jet wakes were replaced after the first VSAERO solution by a solid surface with non-zero normal velocity such as one of the aircraft body elements. Figures 13(a) through 13(h) are from the second iteration, reflecting one feedback from the first APPL iteration. Figure 13(a) shows the same aircraft geometry with solid jet surfaces constructed from the APPL code. These surfaces were positioned adjacent to the outer edge of the plume shear layer. Figures 13(b) to 13(d) show better correlation of  $C_p$  on the fuselage than in Figures 12(b) to 12(d), whereas the  $C_p$  on the wing sections in Figures 13(e) to 13(h) does not indicate much influence from jet effects other than a slight decrease in negative loading. It was observed in this iteration that boundaries of two jets intersect, merging as a confluent jet. In this confluent jet, the vectored thrust jet outer boundary touched the core of the lift jet, which disturbed the velocity scan in VSAERO. A tightening of the jet "boundaries" was used in trying to avoid this difficulty. Figure 14(a) shows the right-hand side aircraft geometry with normal jets and Figure 14(b) shows tightened jets with still intersecting cores. The  $C_p$  values along wings and fuselage sections did not improve over the previous results in Figures 13(b) to (h).



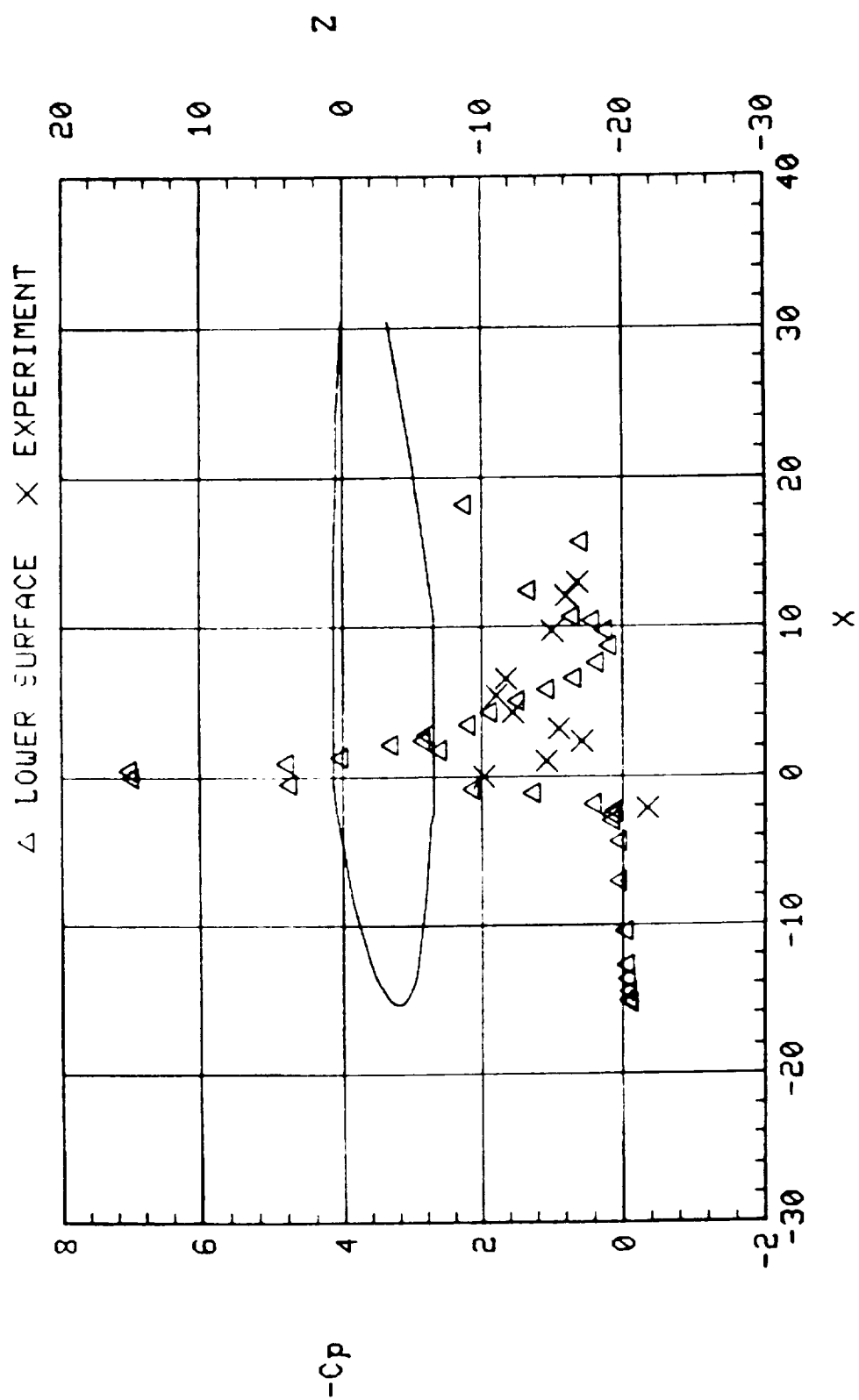
(a) Aircraft Paneling of Right-Hand Side

Figure 12. A Vectored-Thrust Model with Lift Jet (Dual Jet); First Iteration,  $V_j/V_o = 3.534$ .



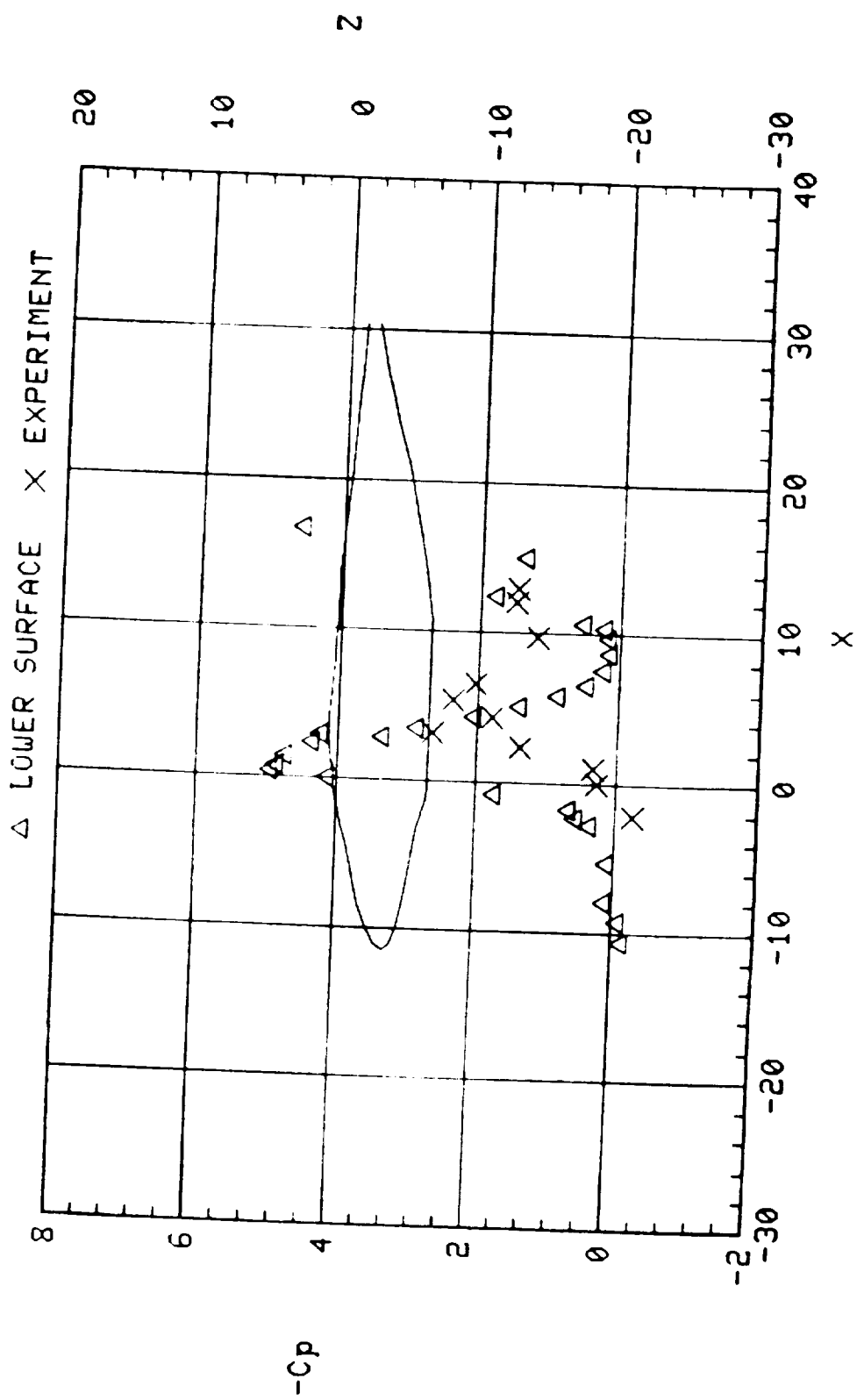
(b)  $C_p$  of Fuselage Bottom at  $Y = 0.0$

Figure 12. Continued.



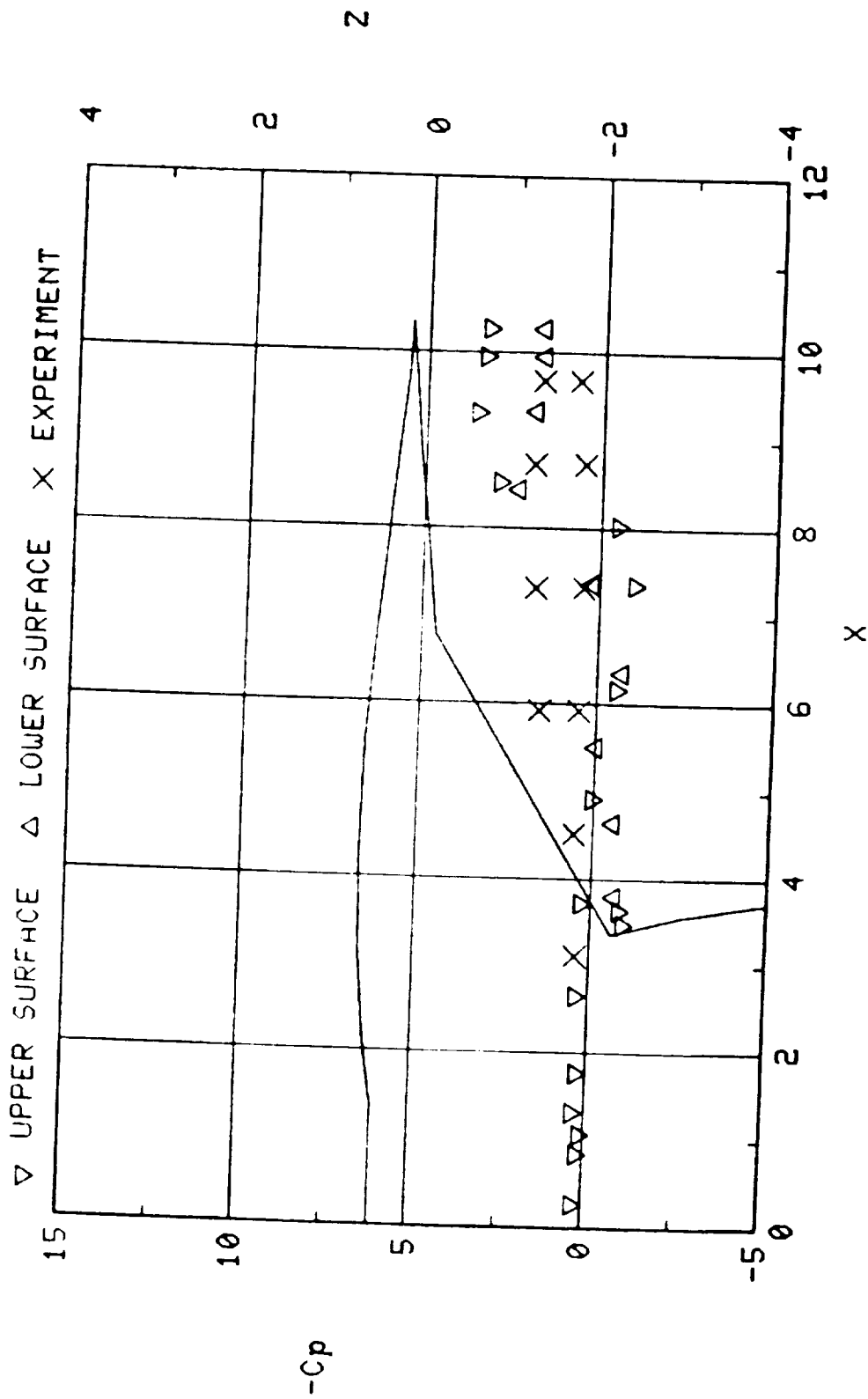
(c)  $C_p$  of Fuselage Bottom at  $Y = 1.25$

Figure 12. Continued.



(d)  $C_p$  of Fuselage Bottom at  $Y = 2.0$

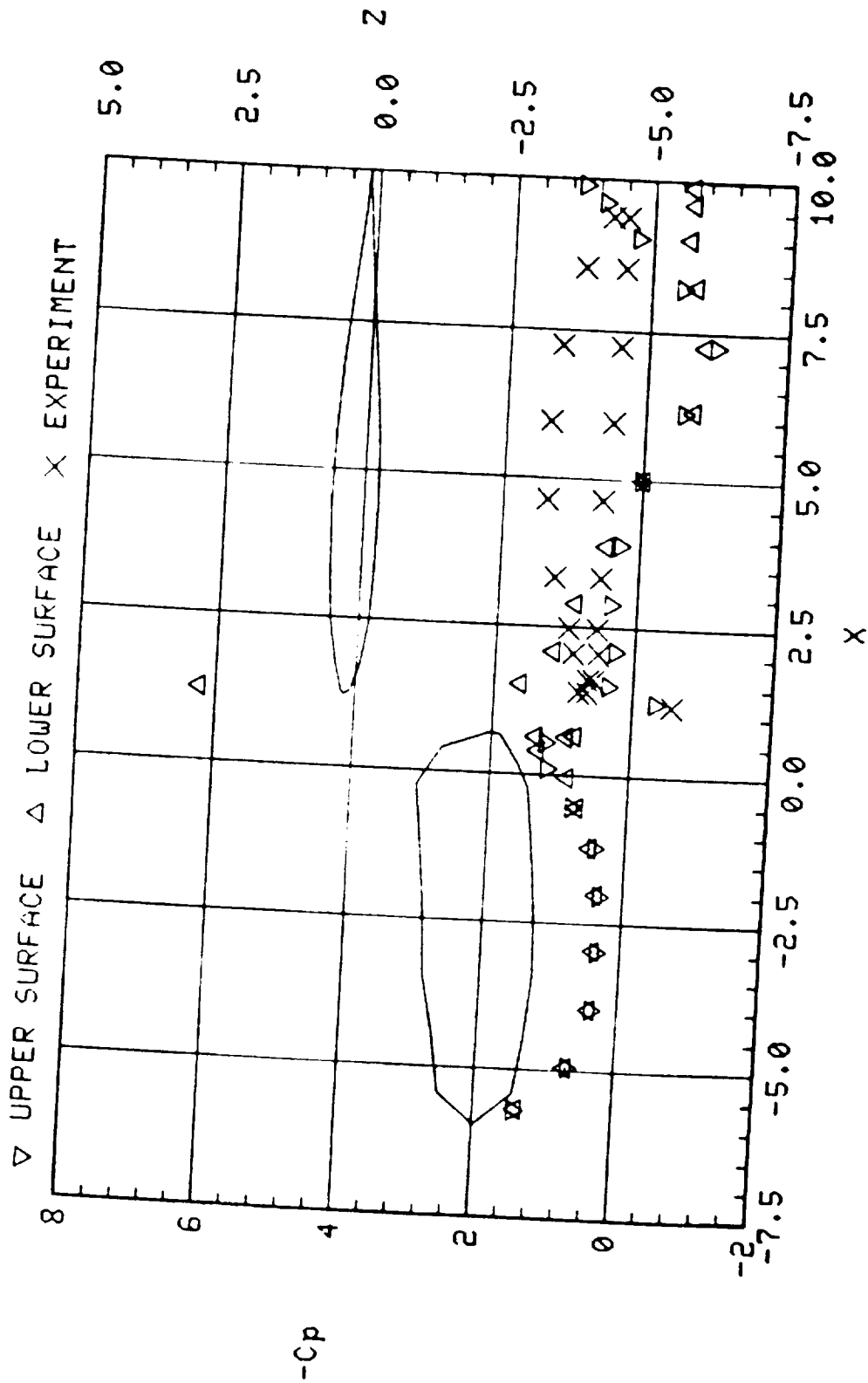
Figure 12. Continued.



(e)  $C_p$  of Wing/Nacelle Section at  $Y = 5.04$

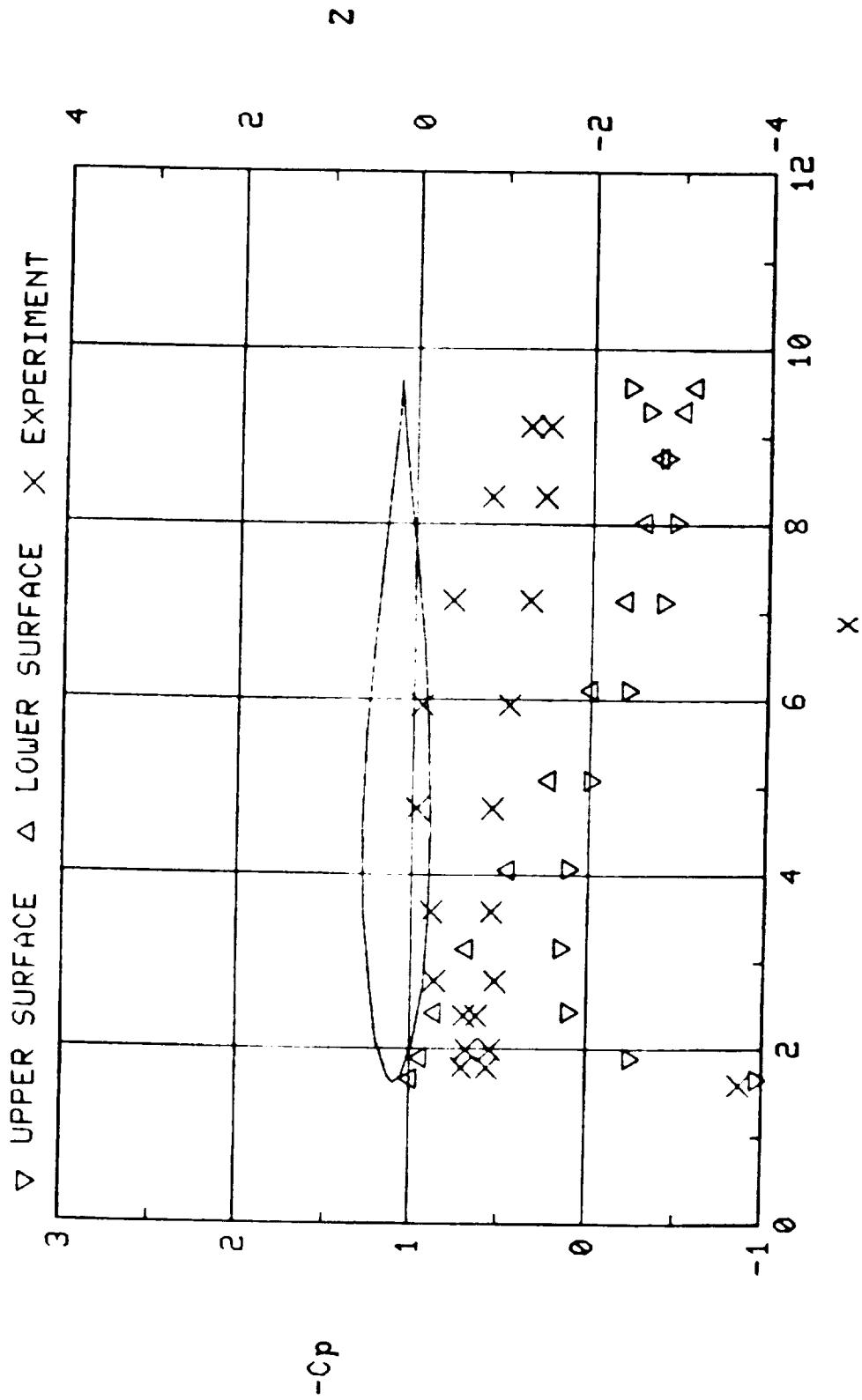
Figure 12. Continued.





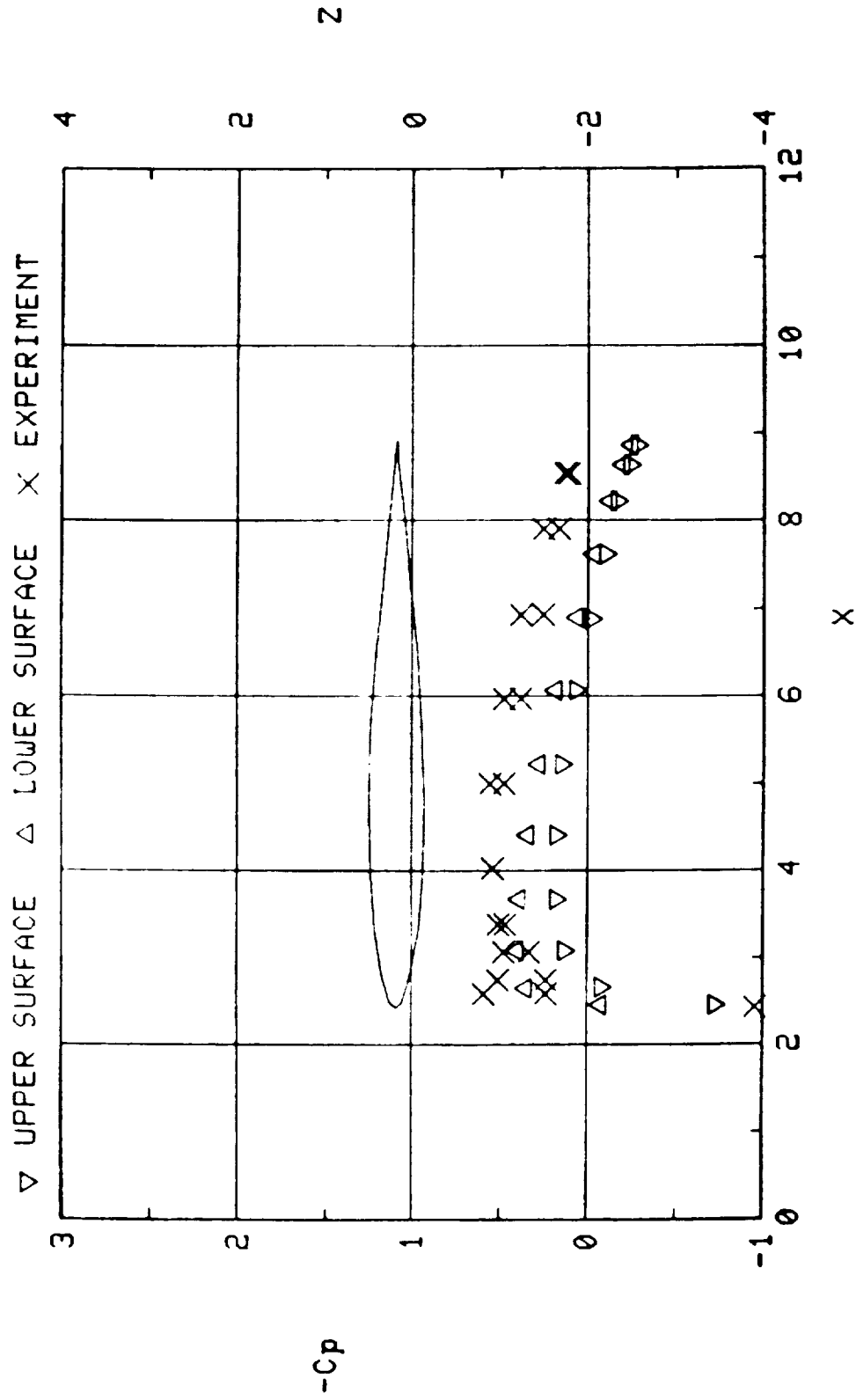
(f)  $C_p$  of Wing/Nacelle Section at  $Y = 7.79$

Figure 12. Continued.



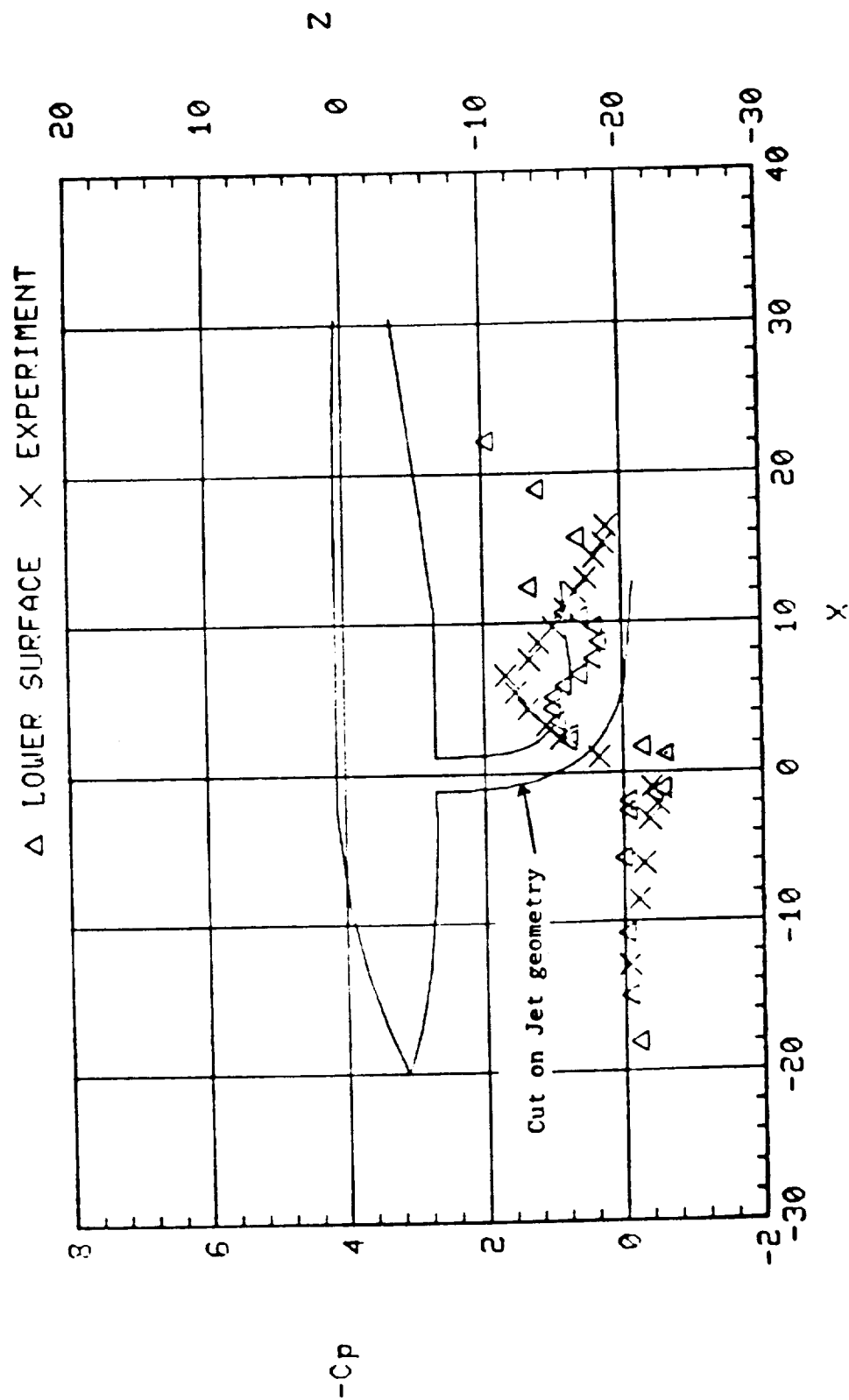
(g)  $C_p$  of Wing Section at  $Y = 10.55$

Figure 12. Continued.



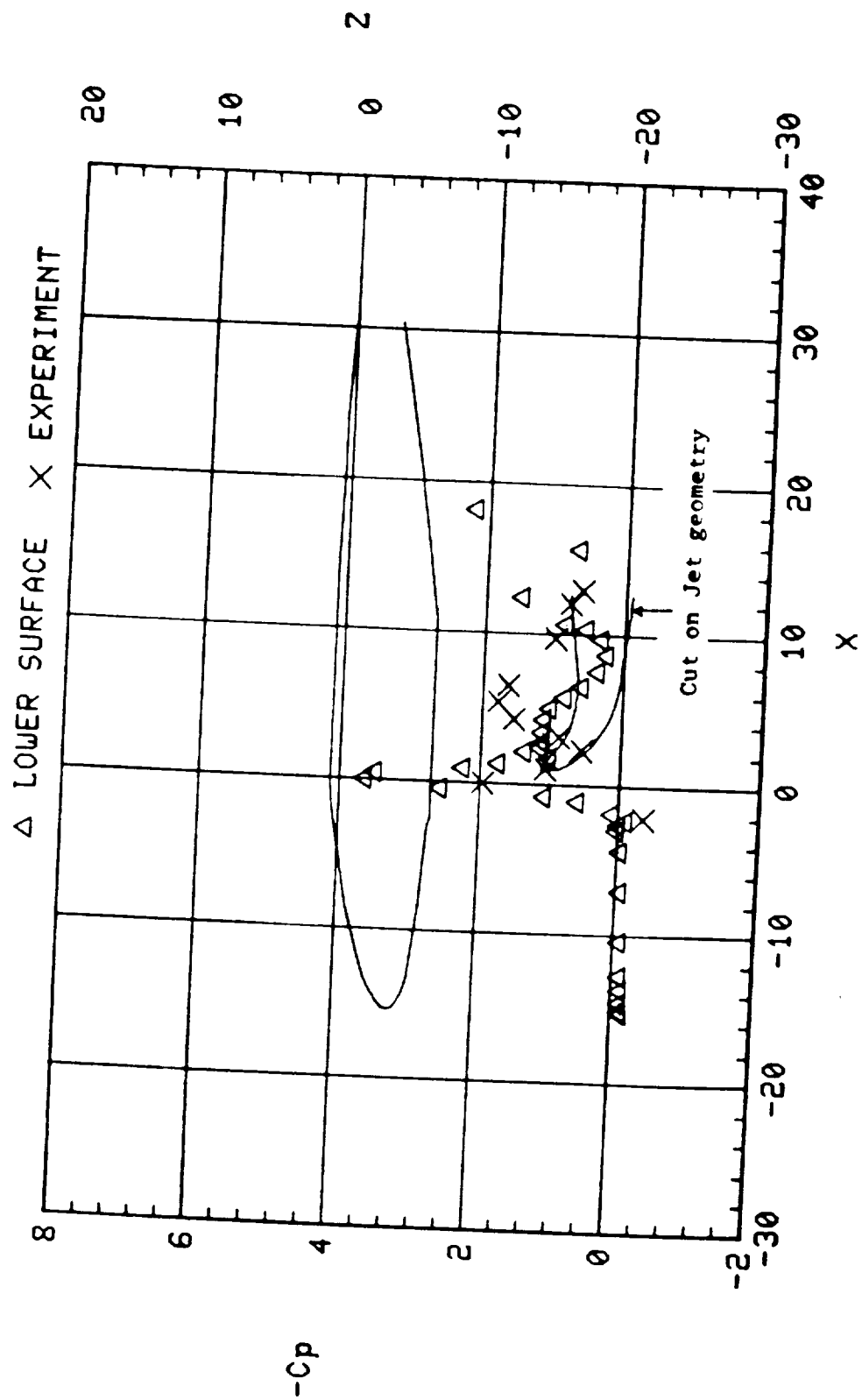
(h)  $C_p$  of Wing Section at  $Y = 16.05$

Figure 12. Concluded.



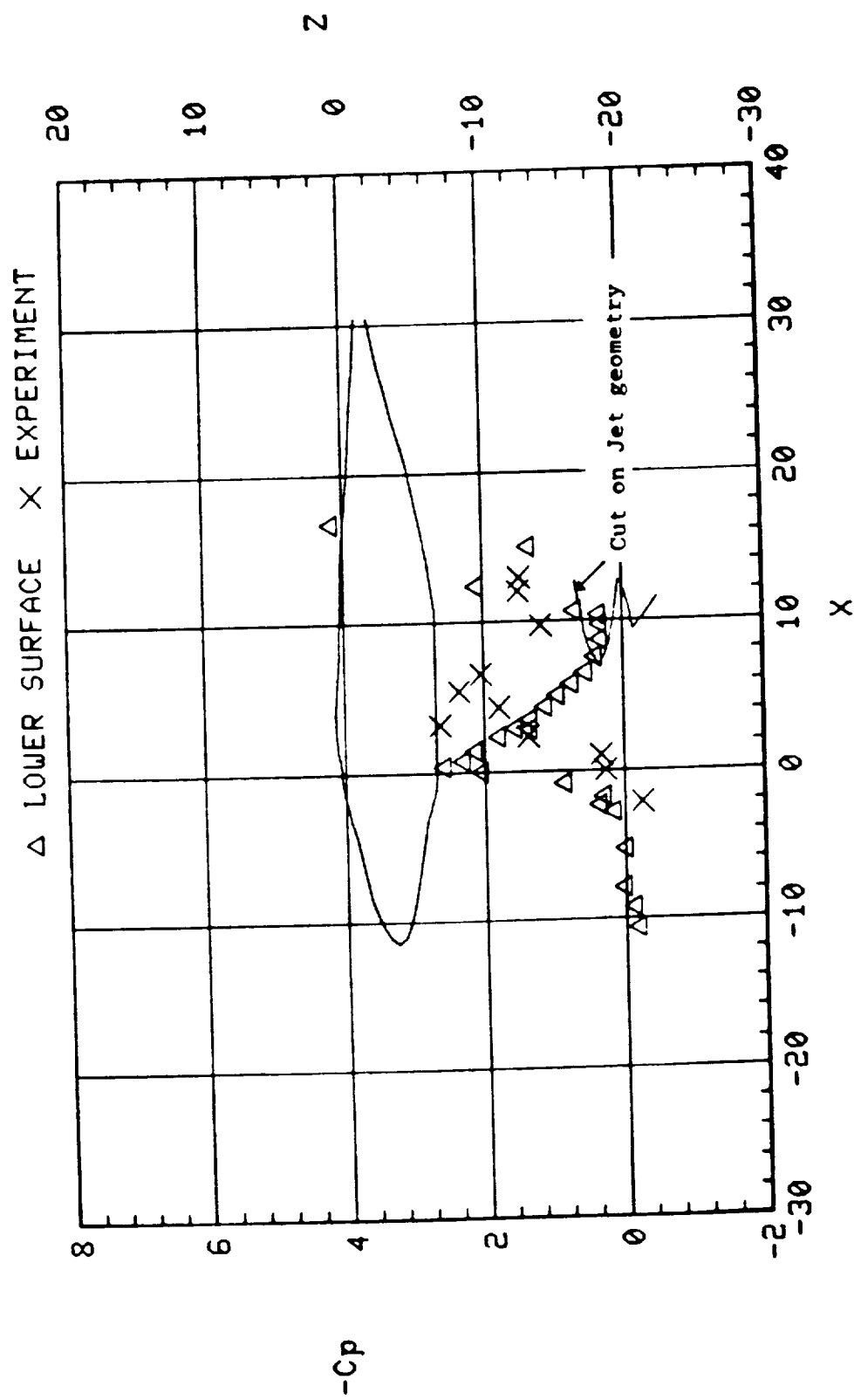
(a)  $C_p$  of Fuselage Bottom at  $Y = 0.0$

Figure 13. A Vectored-Thrust Model with Lift Jet (Dual Jet); Second Iteration.



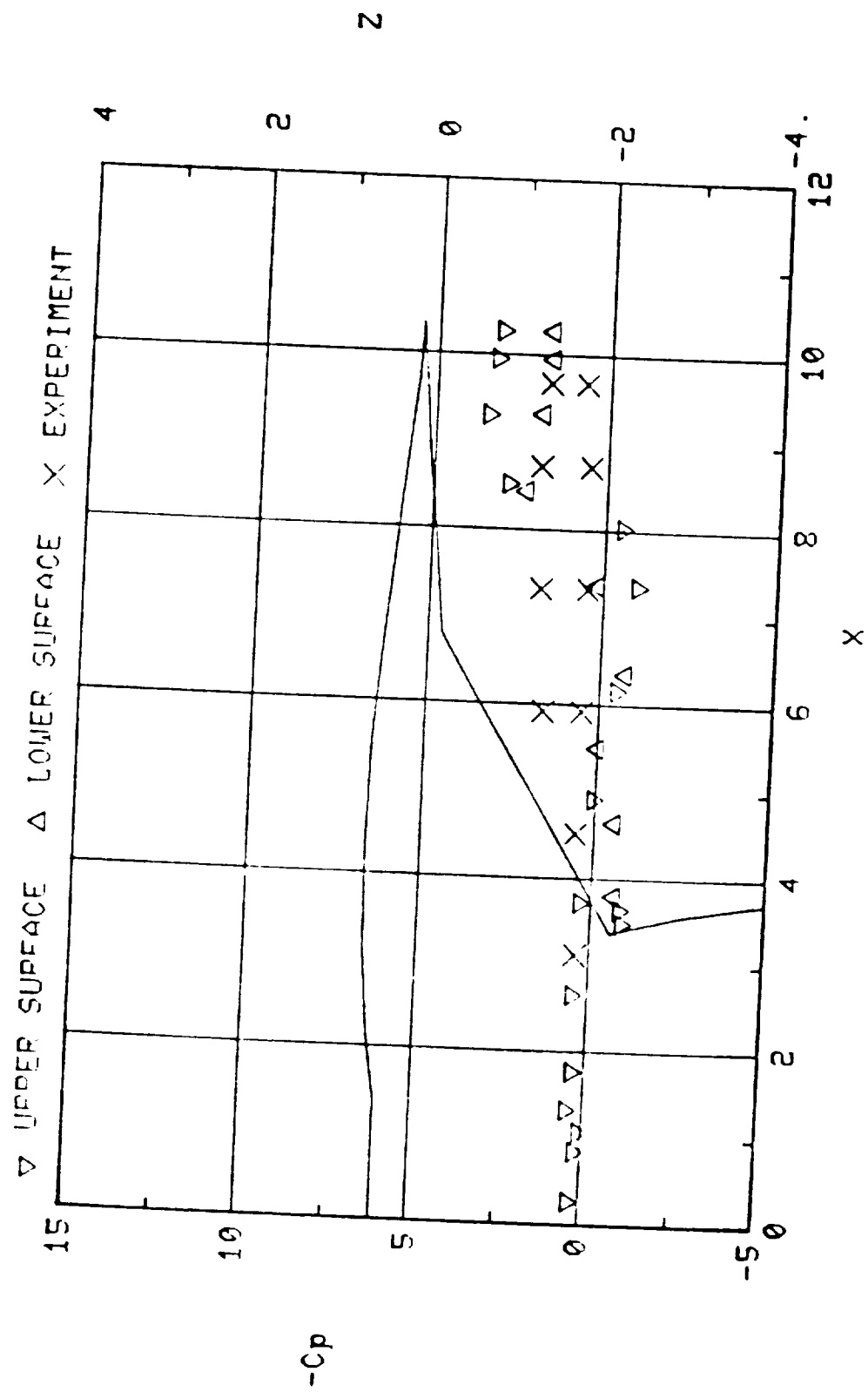
(b)  $C_p$  of Fuselage Bottom at  $Y = 1.25$

Figure 13. Continued.



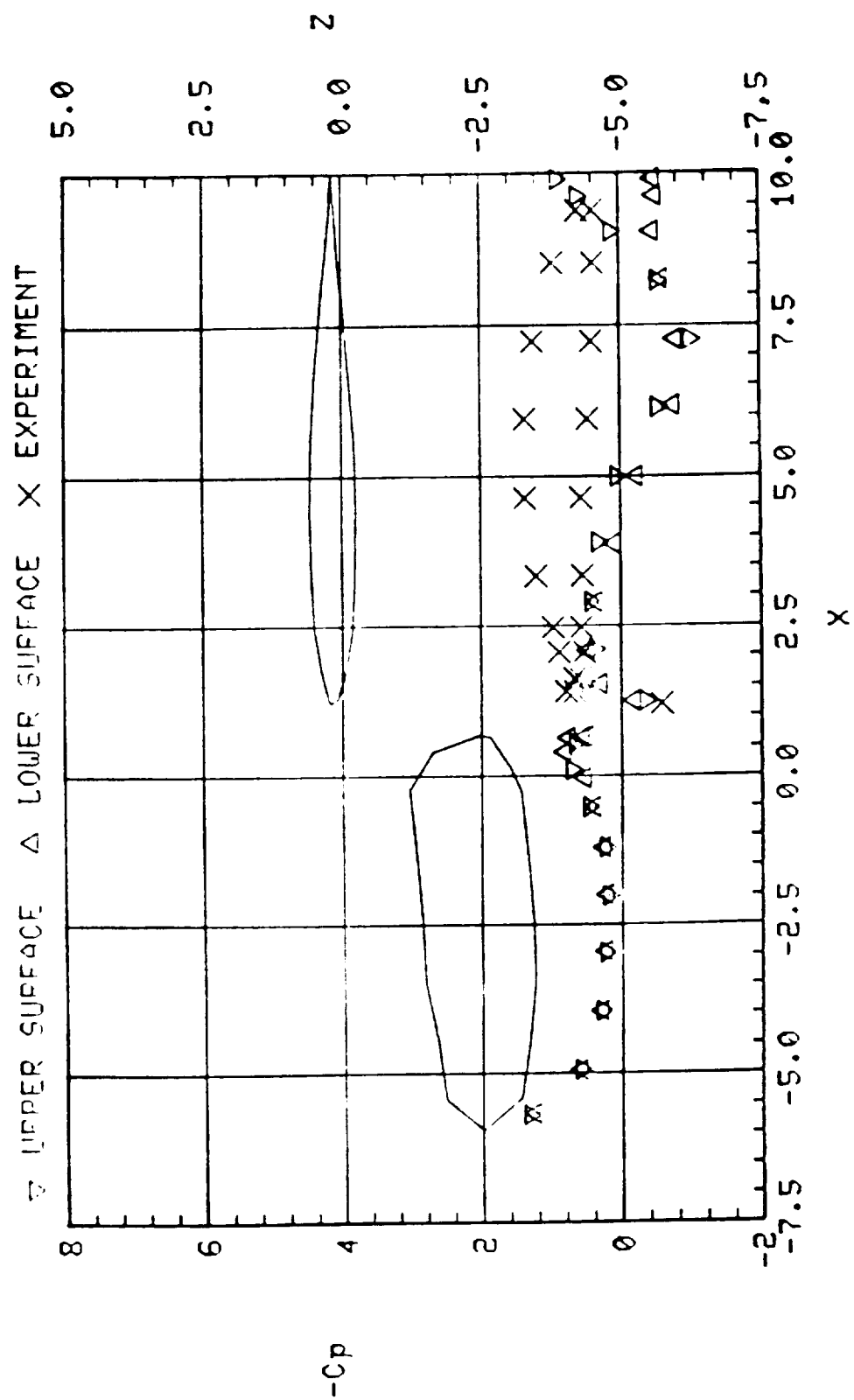
(c)  $C_p$  of Fuselage Bottom at  $Y = 2.0$

Figure 13. Continued.



(d)  $C_p$  of Wing/Nacelle Section at  $Y = 5.04$

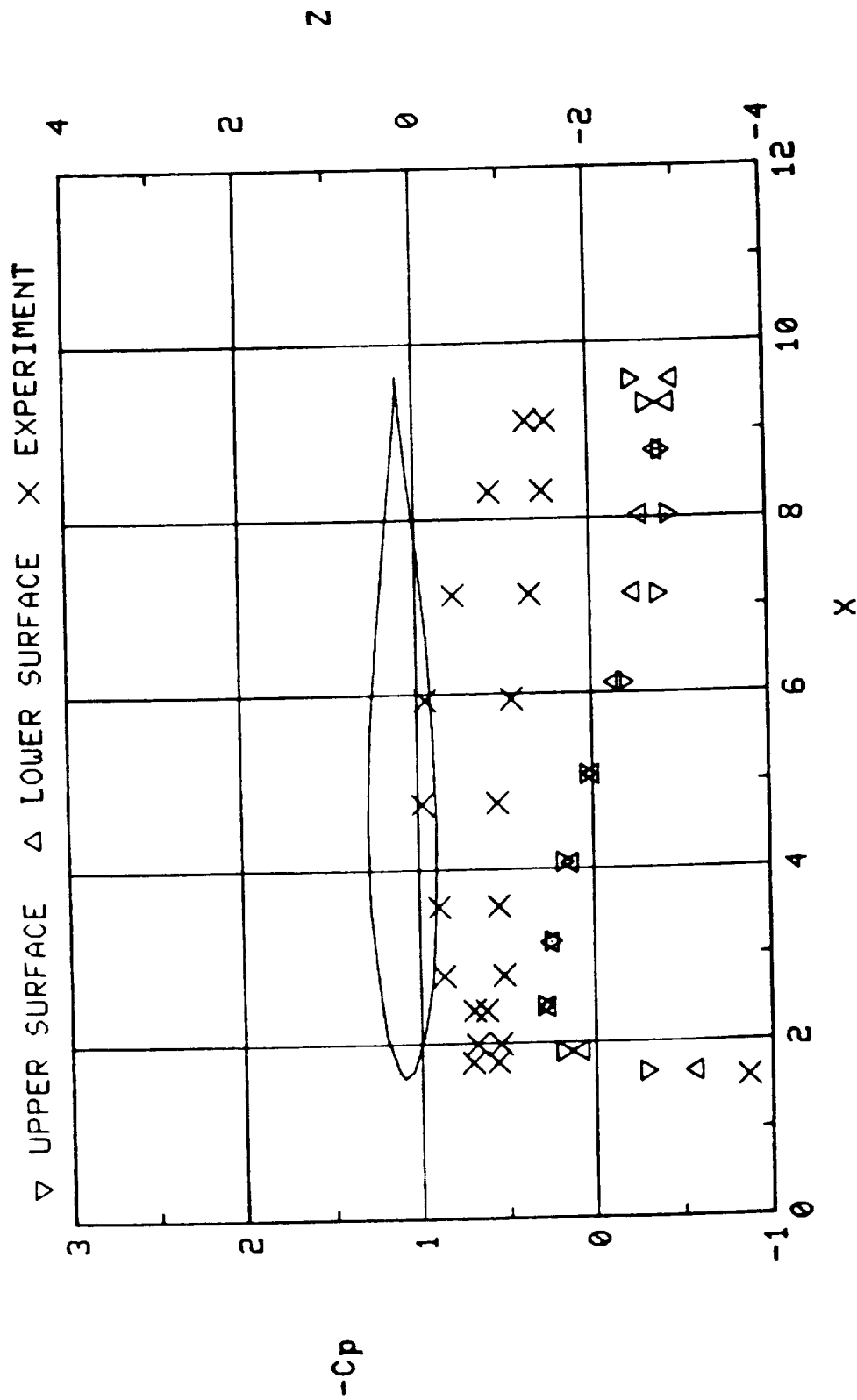
Figure 13. Continued.



(e)  $C_p$  of Wing/Nacelle Section at  $Y = 7.79$

Figure 13. Continued.

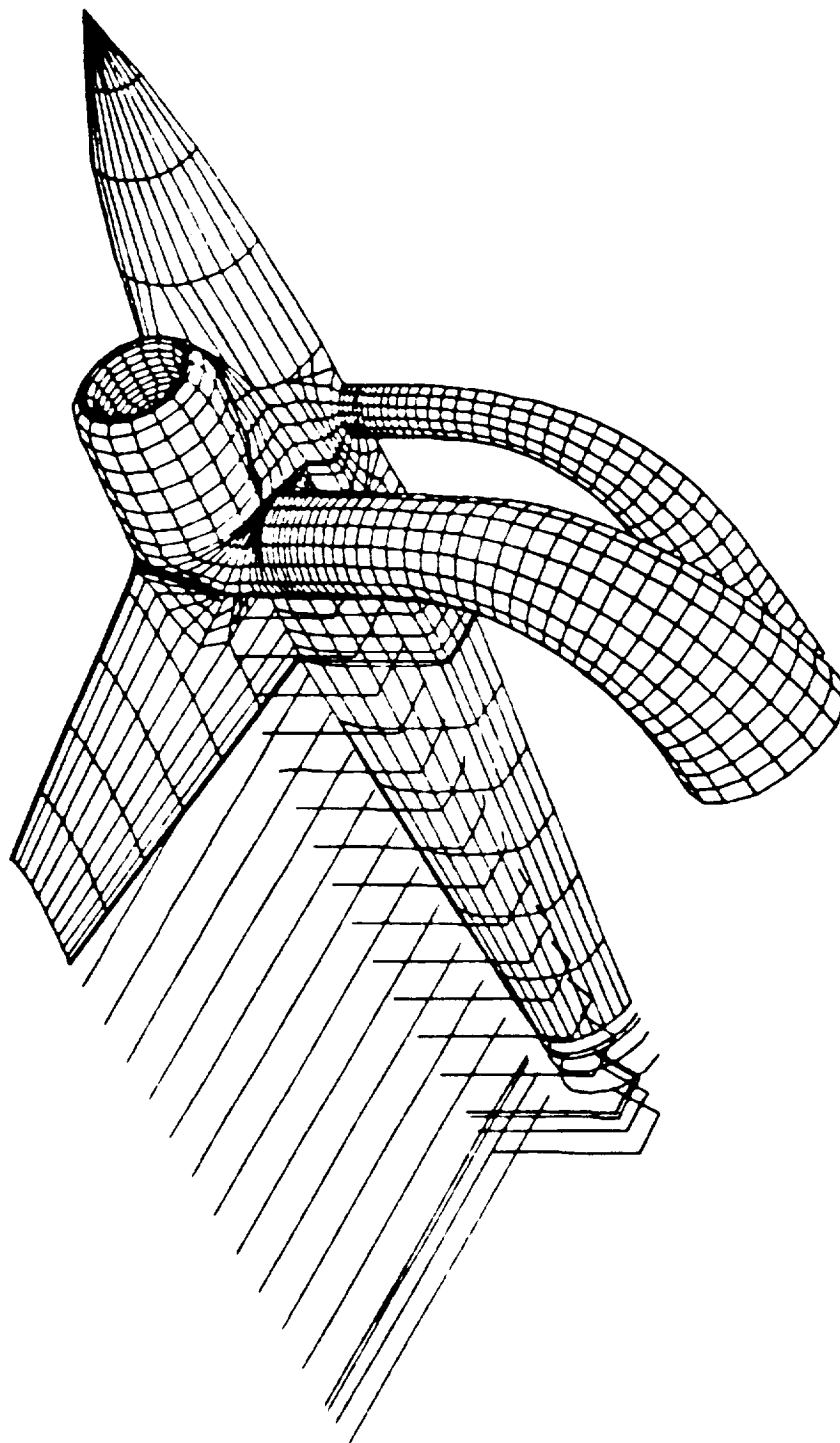




(f)  $C_p$  of Wing Section at  $Y = 10.55$

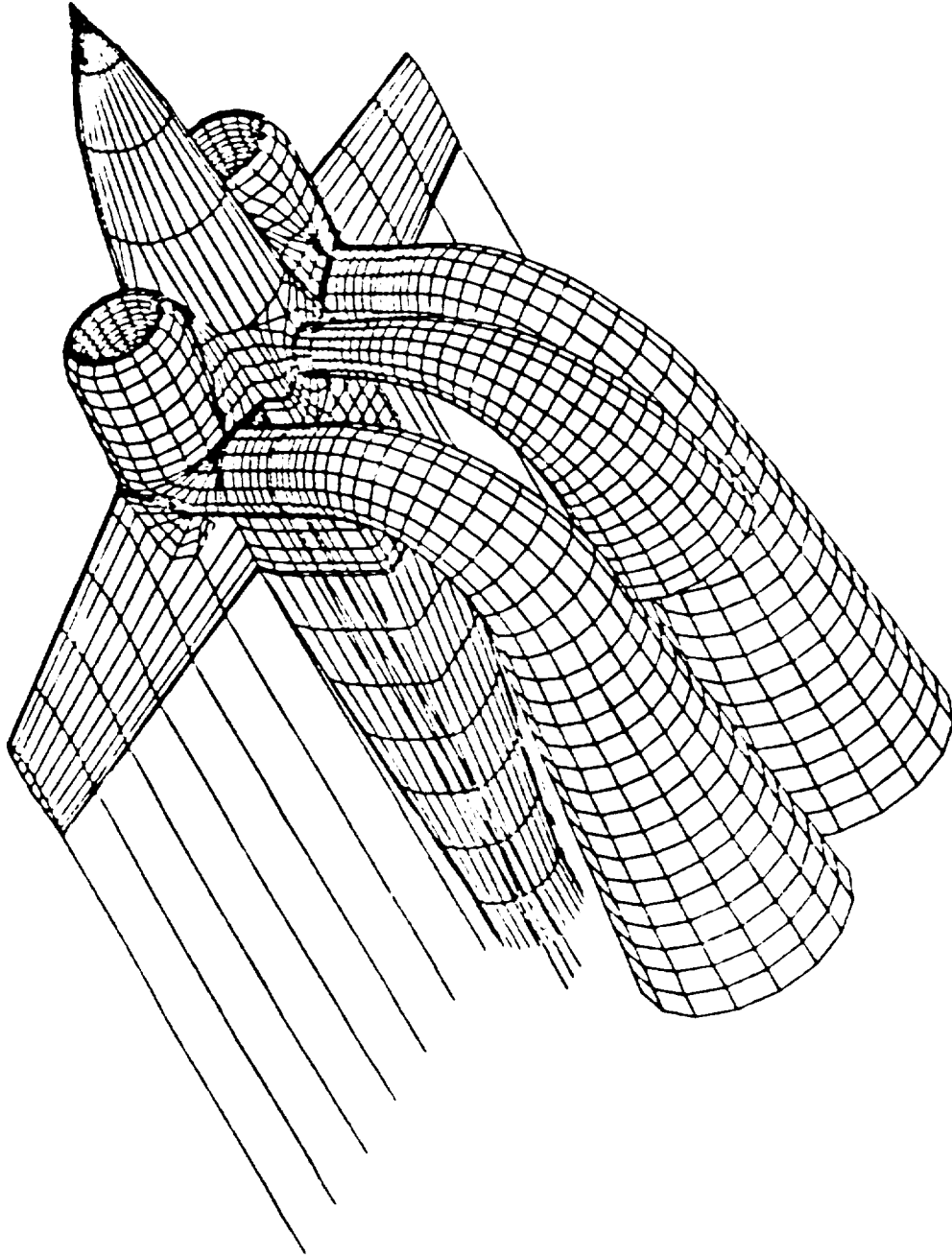
Figure 13. Continued.





(a) Right-Hand Side Paneling with Dual Jet Surfaces at Second Iteration

Figure 14. Jet Trajectories.



(b) Panelling with Tightened Dual Jet Surfaces at Second Iteration

Figure 14. Concluded.

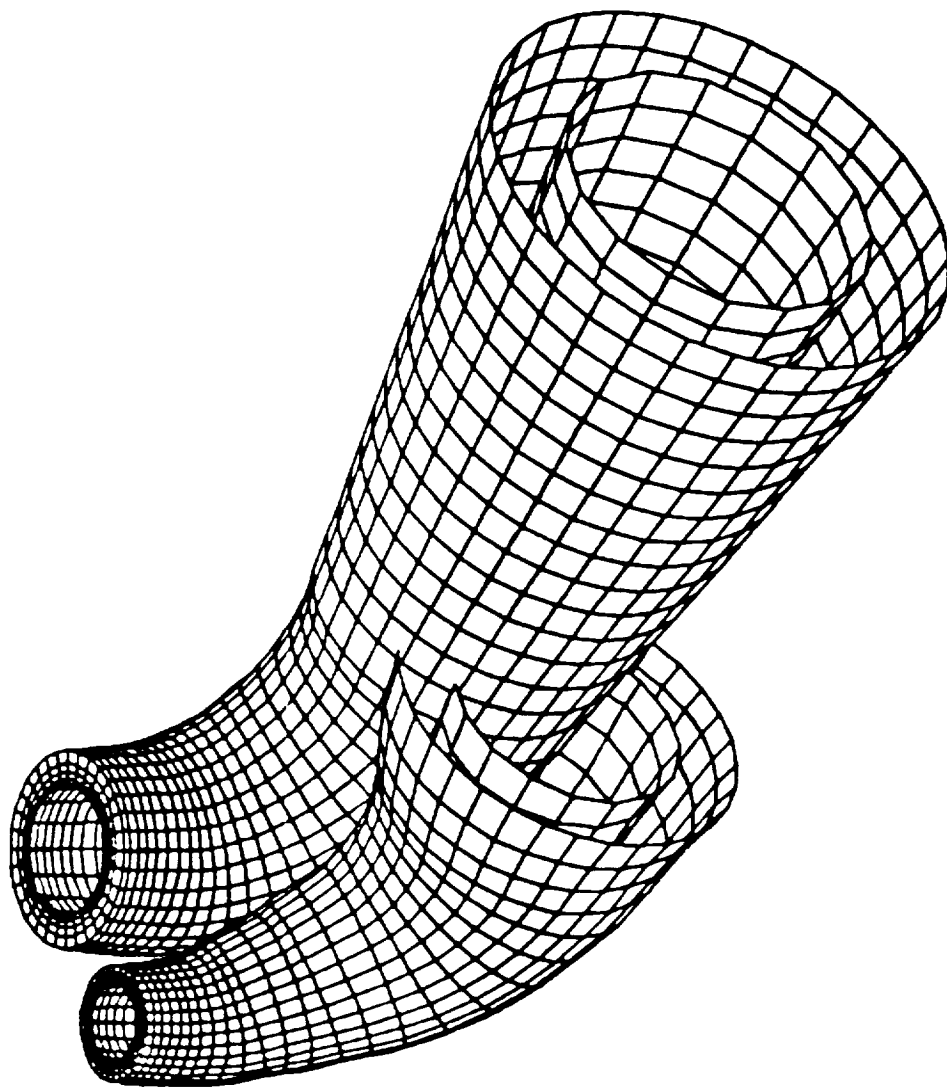


Figure 15. Intersecting Jet Plumes of Both Cores and Boundaries at Third Iteration.

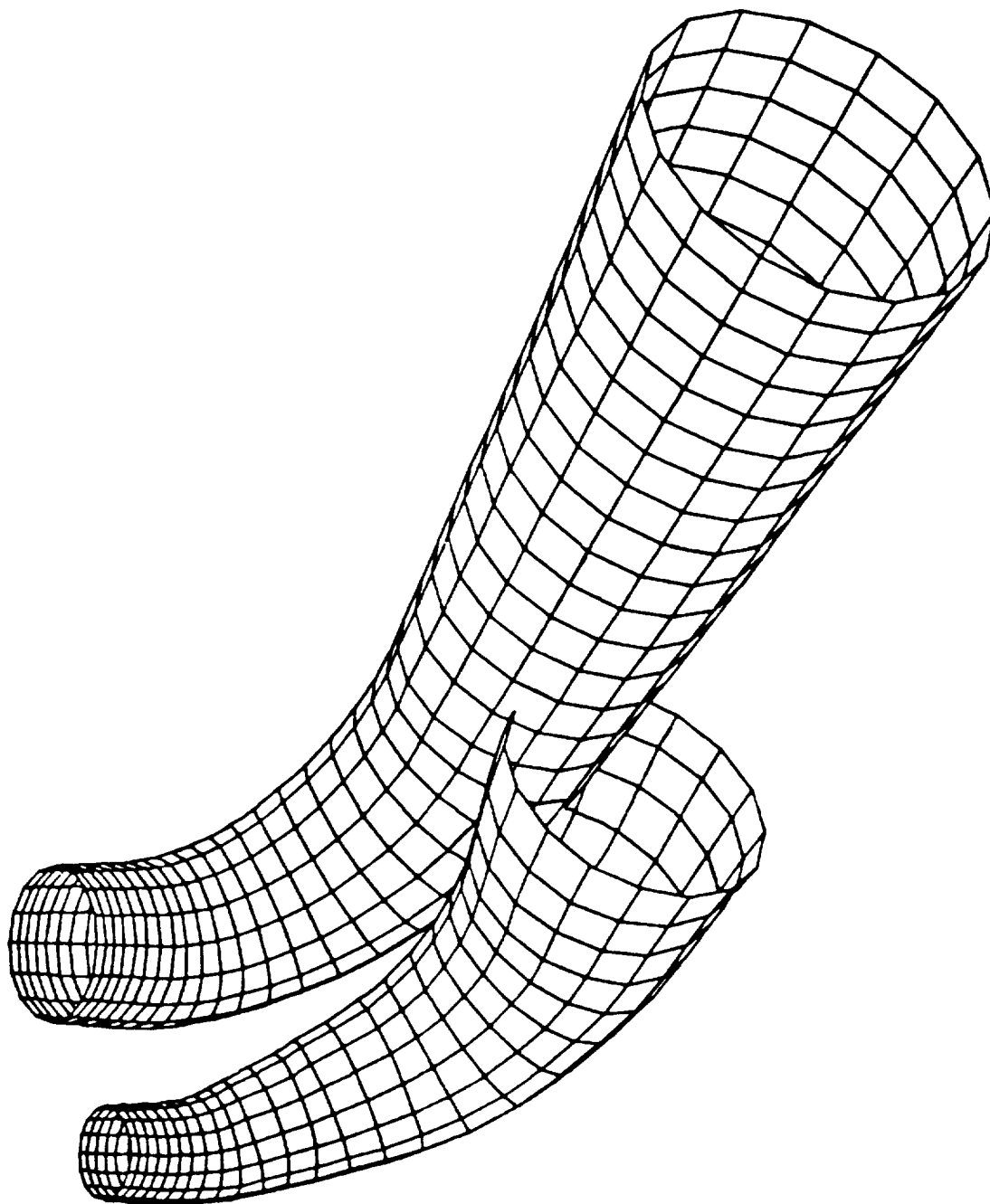


Figure 16. Development of Confluent Jet Core at Third Iteration.

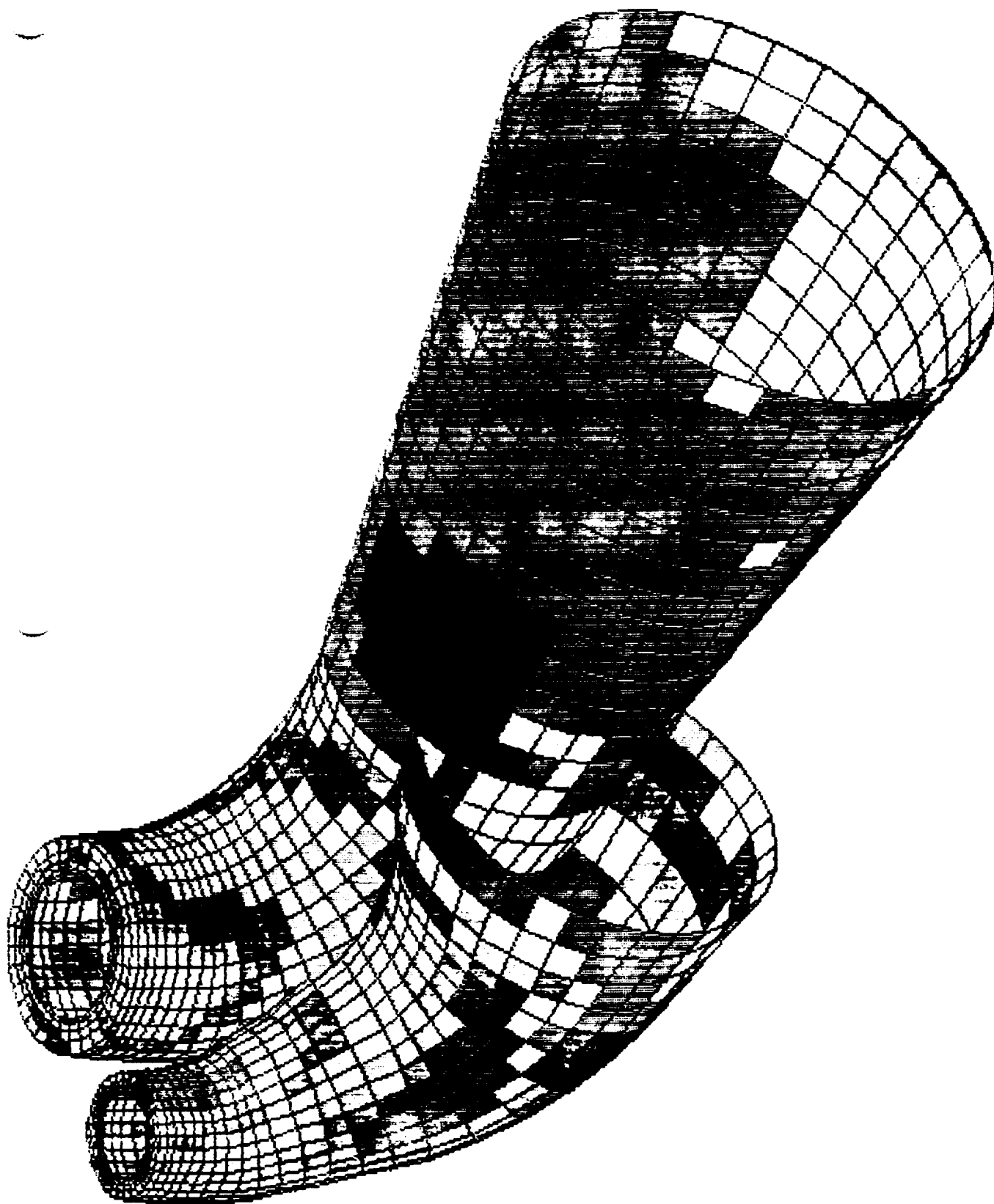


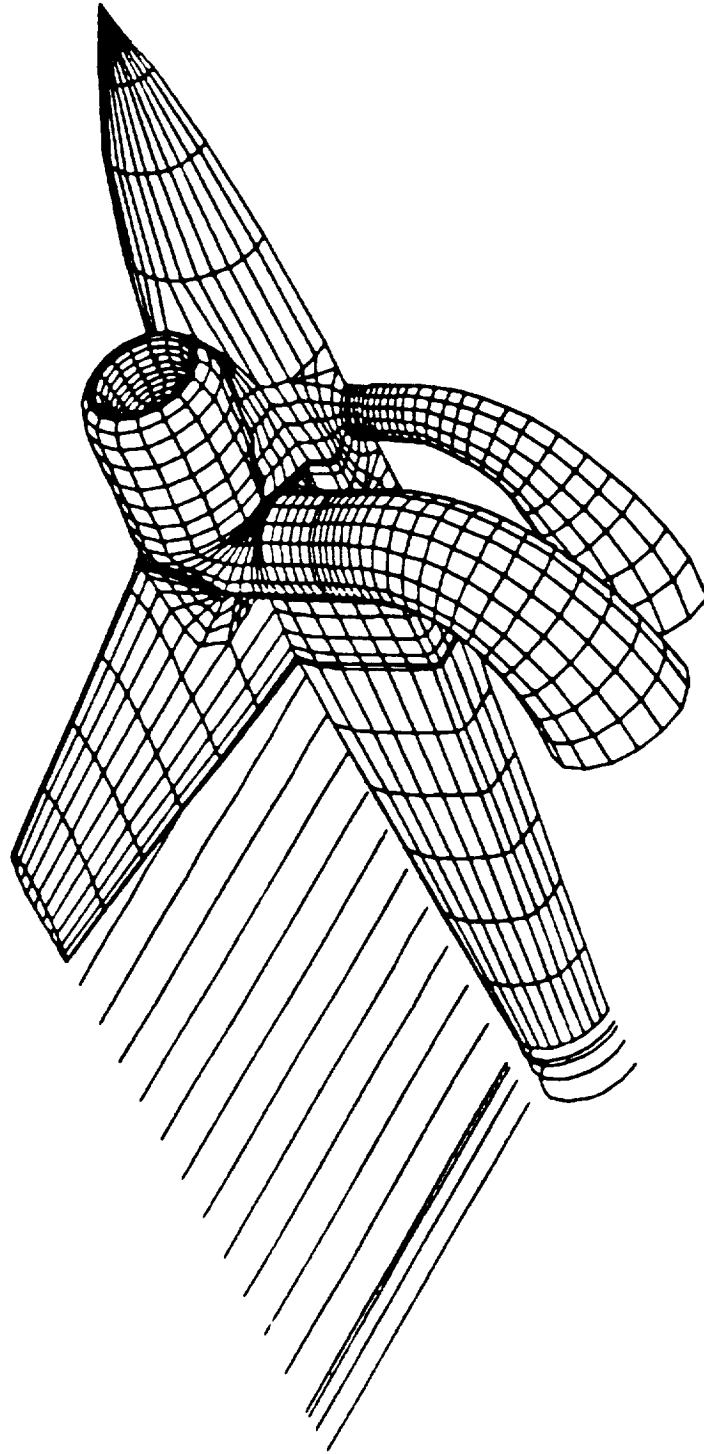
Figure 17. Cp Distributions on the Outer Boundaries at the Third Iteration.

the  $C_p$  predictions right behind the jet exit location became worse. Figure 18(a) shows the jet plume trajectories at the final iteration. Figures 18(b) through (d) show the  $C_p$  distributions on the fuselage sections and Figures 18(e) through (h) do on the wing sections.

This case was beyond the scope of the current work since the two jet boundaries tended to overlap as the jets developed downstream. This made a converged, coupled analysis impossible since reliable boundary conditions could not be obtained from the VSAERO solution in the overlap region. However, the results of the APPL runs provided some interesting features. The streamwise velocity contours for the fuselage jet, Figure 19, indicate a reduced roll-up compared with the single jet case, Figure 11(h). This is probably due to the blockage created by the outboard jet. The cross-flow velocity vectors, Figure 20, show a weaker vortex pair in the jet which is consistent with the reduced roll-up. A second vortex pair has also appeared as a result of the interaction with the outboard jet. The streamwise velocity contours, Figure 21, for the outboard jet show a definite skew as the jet is pushed further outboard. The jet moved towards the mesh boundary as the trajectory routine tried to keep up with it. The growth rate of the outer boundary was restricted to try to keep the two jets from overlapping. This restriction, which ultimately was not successful, led to a crowding of the jet flow field. The interaction of the jet with the boundary is clearly indicated in the cross-flow vector field, Figure 22. A vortex pair is not visible but a roll-up of the jet is observed in Figure 21. It is noted that the outboard jet was deflected by the interaction with the fuselage jet such that the centerline of the jet was pointing about  $20^\circ$  away from the plane of symmetry.

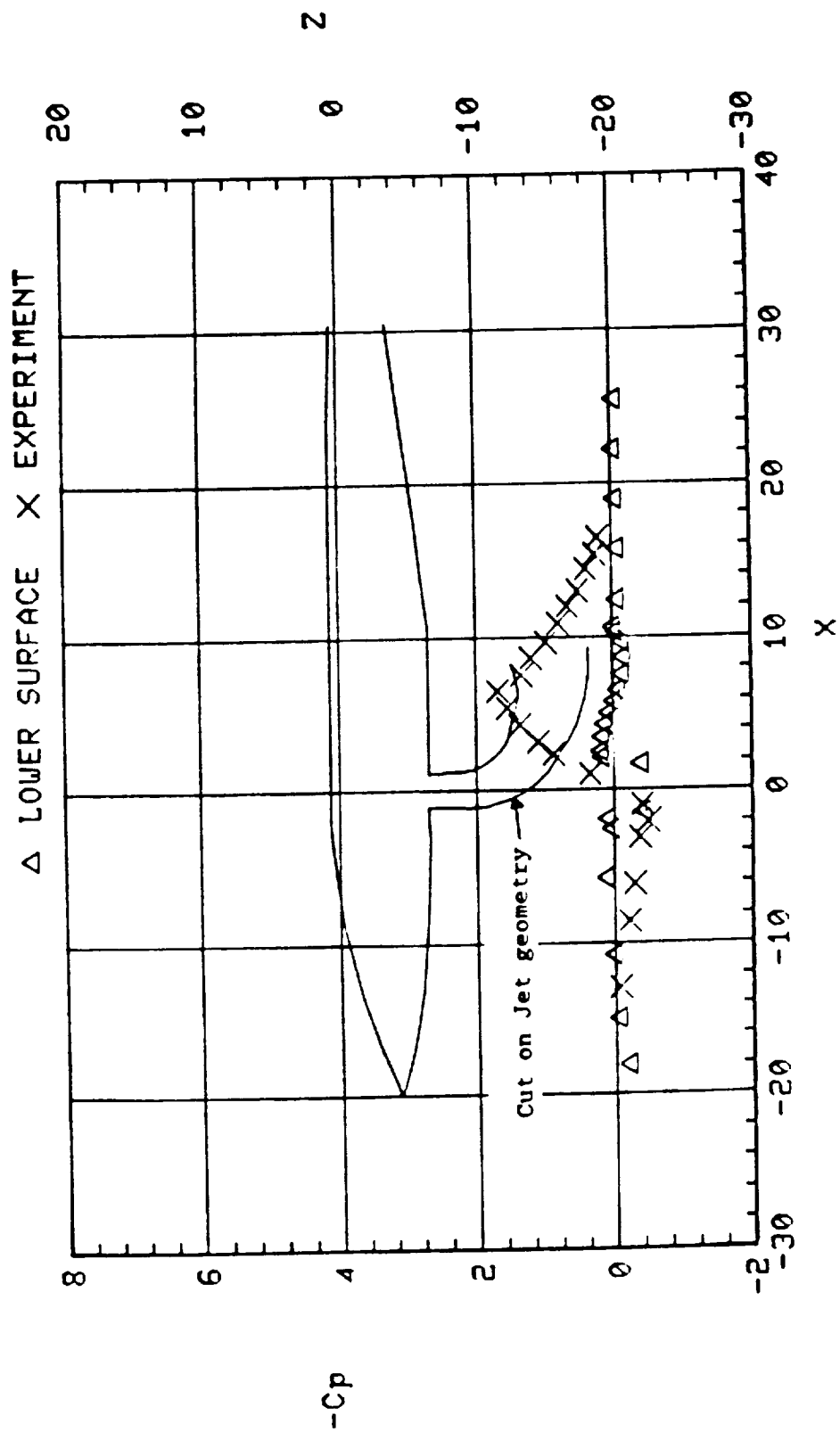
Finally, in a confluent jet situation, the line of intersection between the two jet boundaries must be identified and taken into account in the paneling. More complex situations will certainly arise, for example, when a jet impinges on or is in close contact with surfaces of the configuration. Multiple zone treatment geared to more complex flow descriptions for separated regions, vortical regions and compressible regions, will make this special and even more demanding.





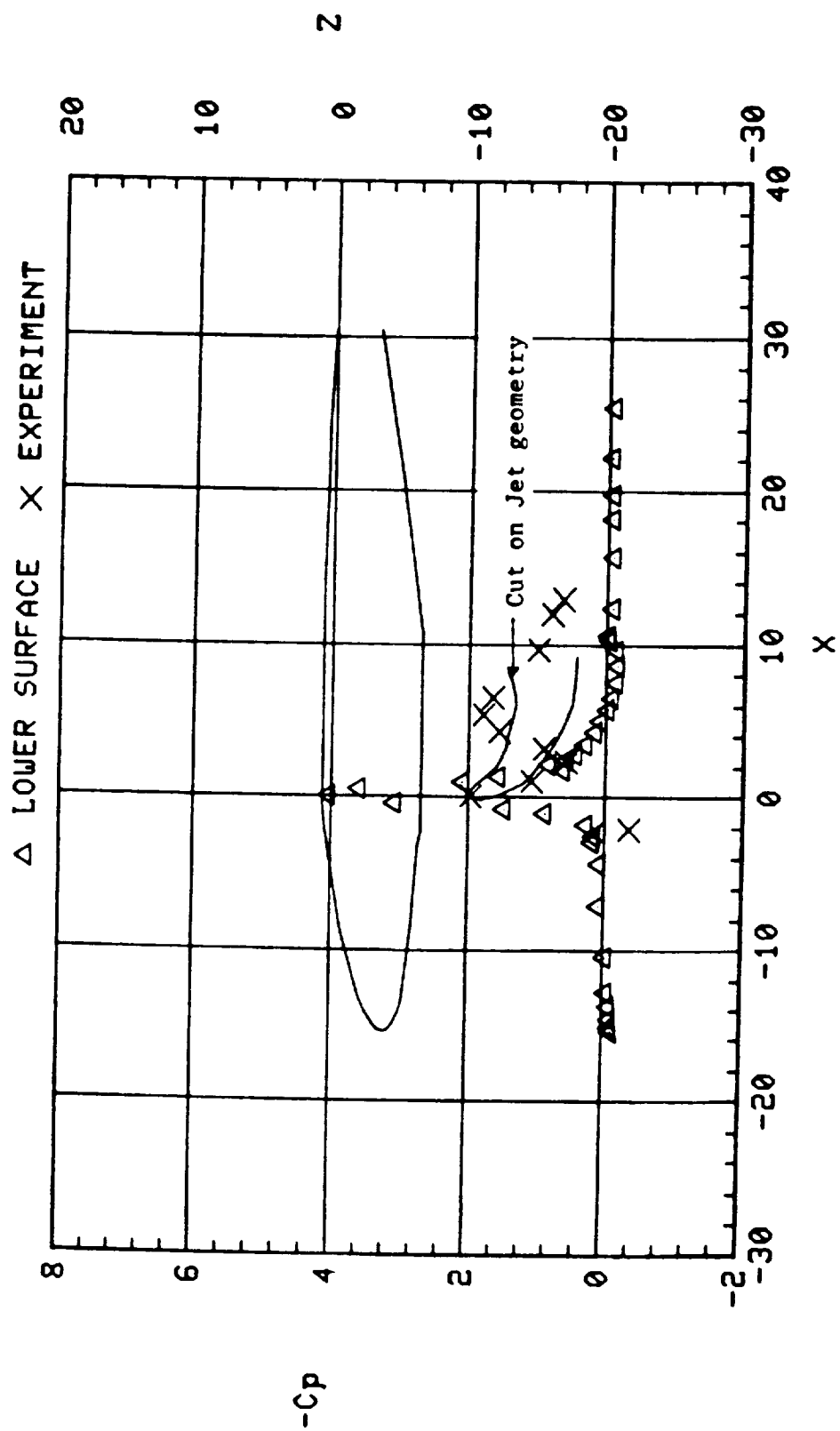
(a) Paneling of Aircraft with Jet Plume Surfaces

Figure 18. Vectored-Thrust Model with Lift Jet; Final Iteration.



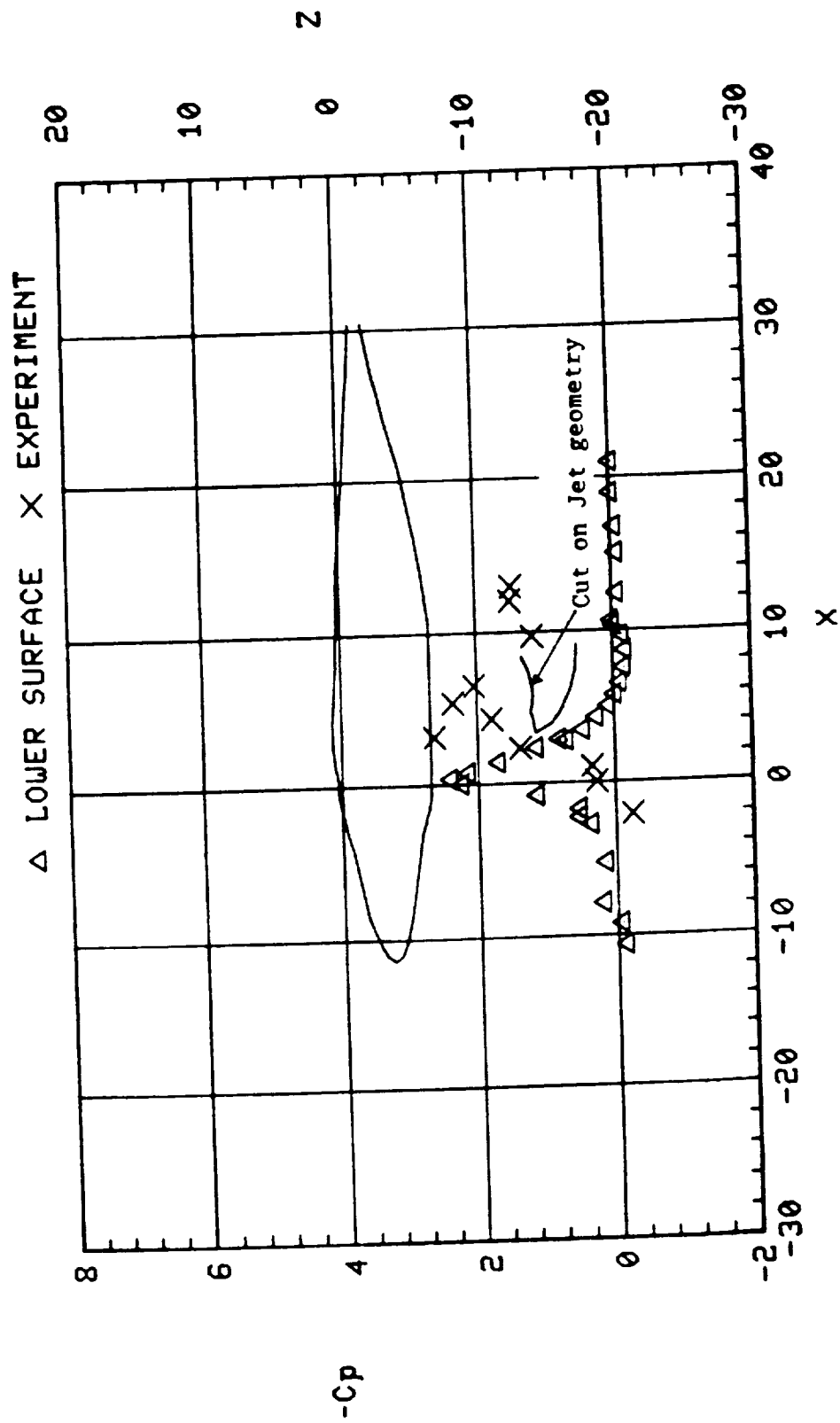
(b)  $C_p$  Distribution on Fuselage Bottom at  $Y = 0.0$

Figure 18. Continued.



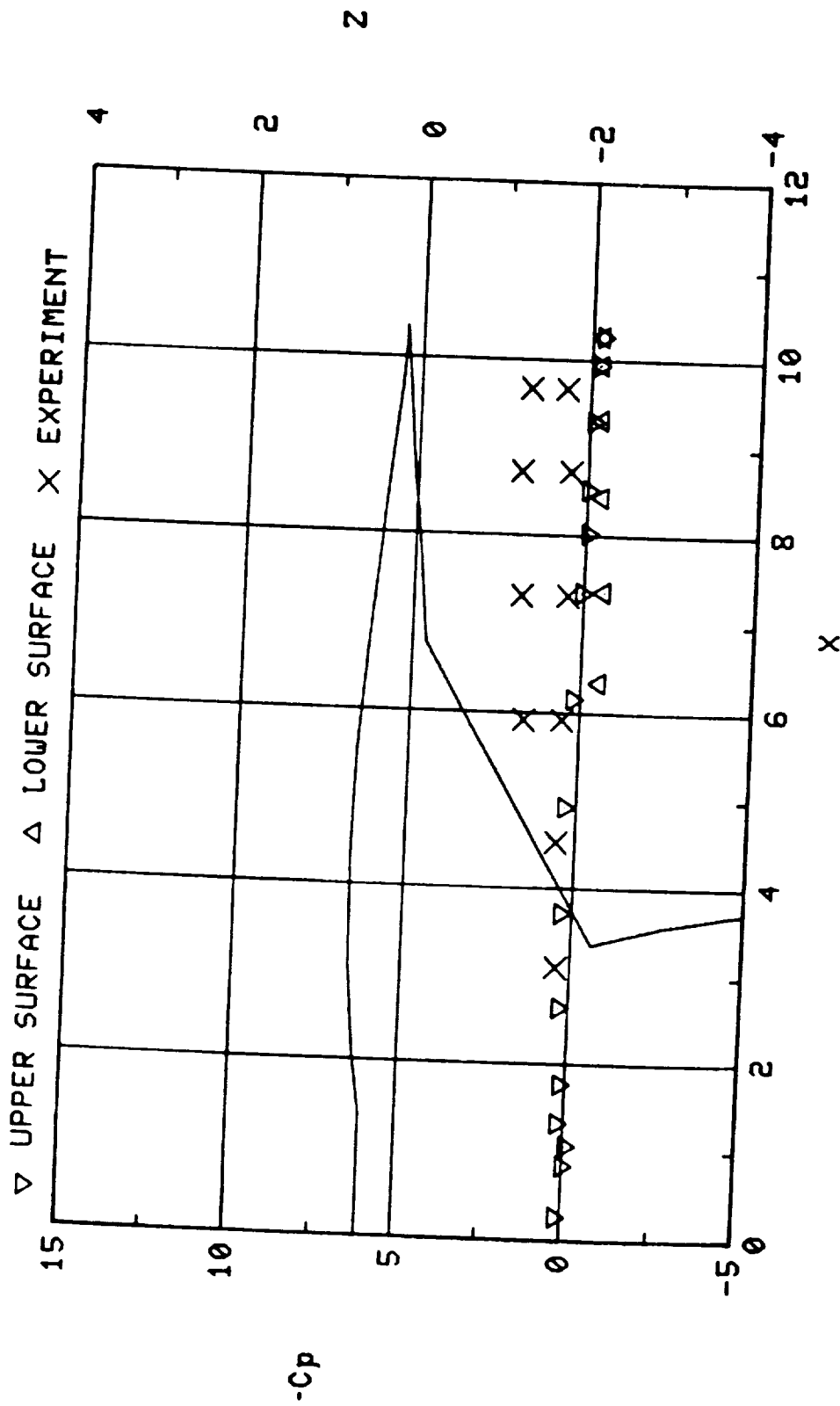
(c)  $C_p$  Distribution on Fuselage Bottom at  $Y = 1.25$

Figure 18. Continued.



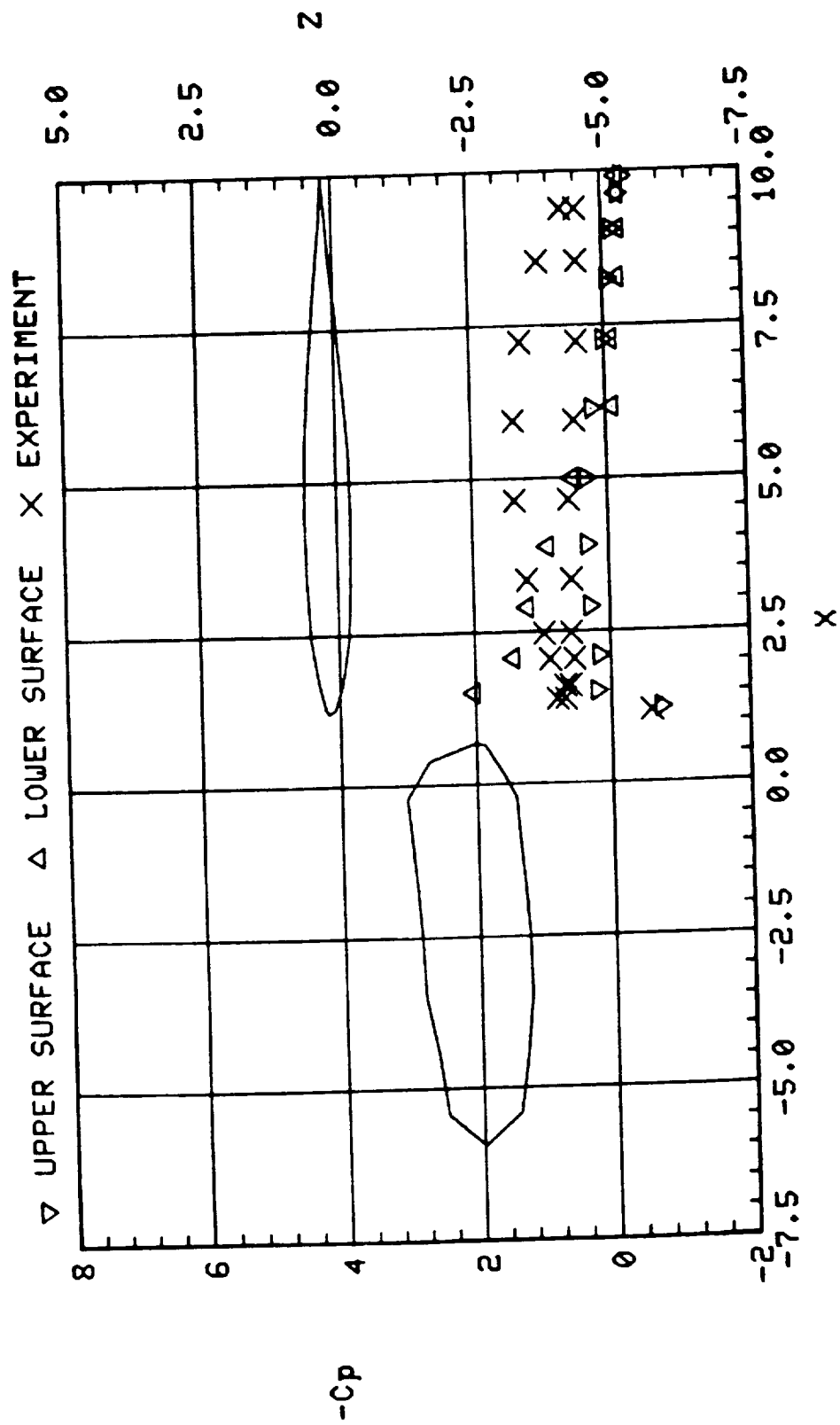
(d)  $C_p$  Distribution of Fuselage Section at  $Y = 2.0$

Figure 18. Continued.



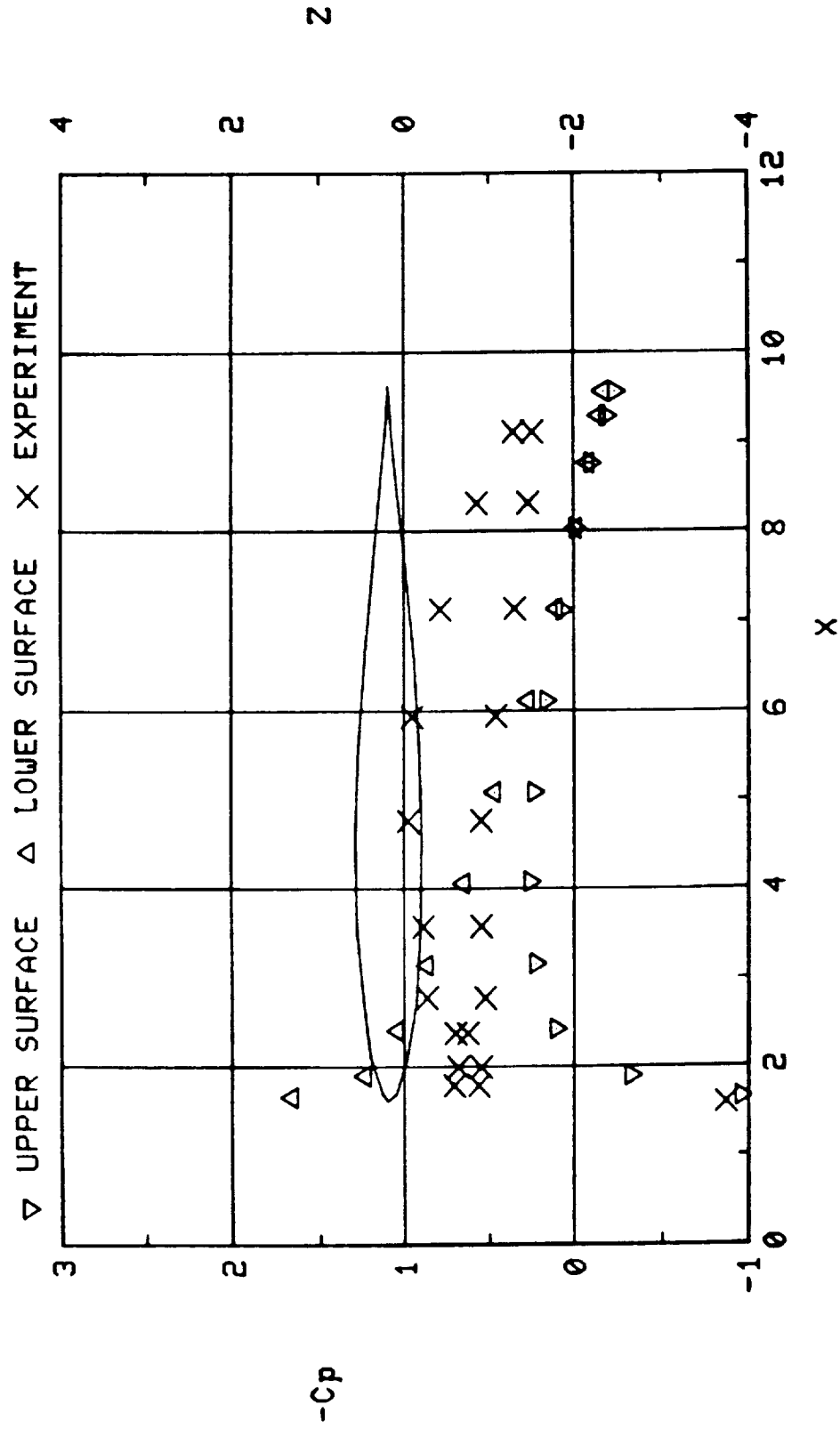
(e)  $C_p$  Distribution on Wing/Nacelle Section at  $Y = 5.04$

Figure 18. Continued.



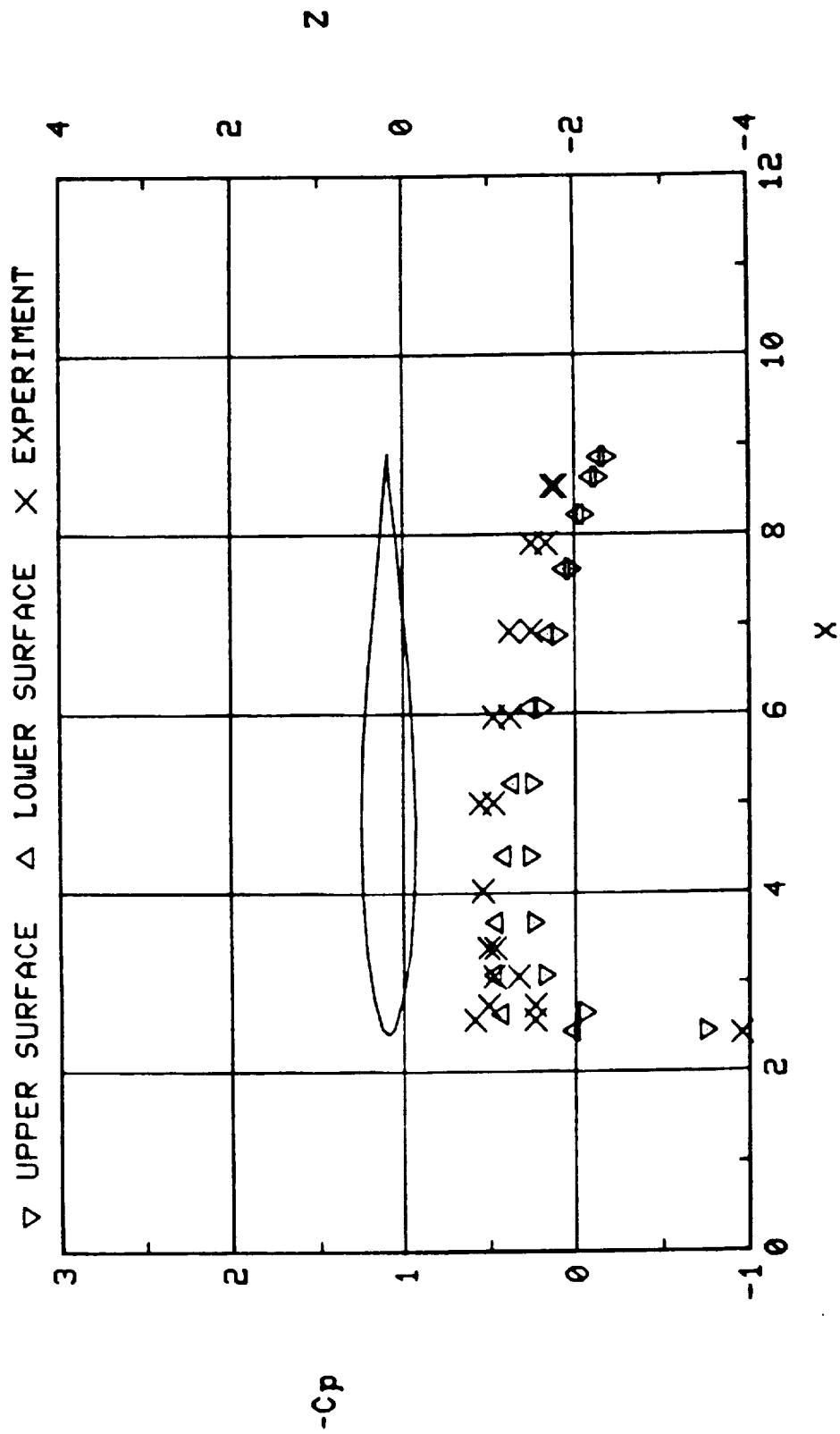
(f)  $C_p$  Distribution on Wing/Nacelle Section at  $Y = 7.79$

Figure 18. Continued.



(g)  $C_p$  Distribution on Wing Section at  $Y = 10.55$

Figure 18. Continued.



(h)  $C_p$  Distribution on Wing Section at  $Y = 16.05$

Figure 18. Concluded.



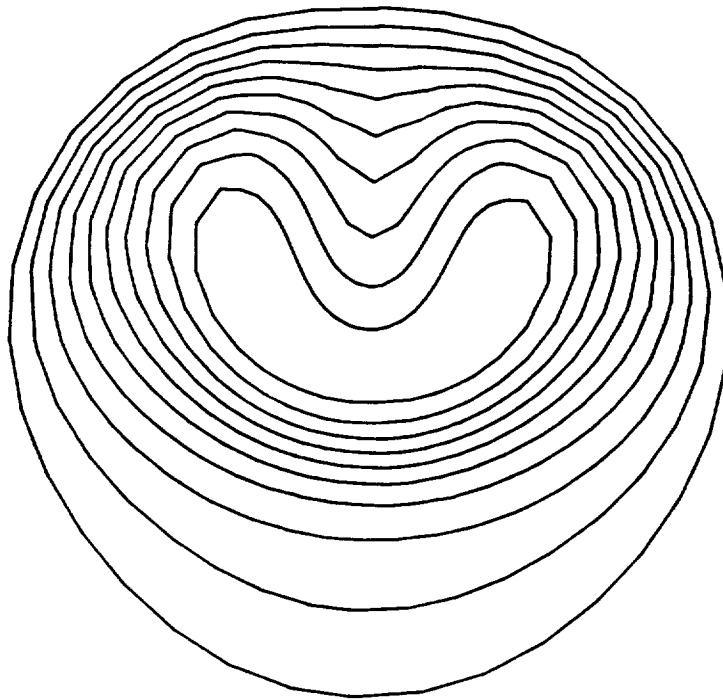


Figure 19. Streamwise Velocity Contours for Lift Jet at  $90^\circ$  Incidence.

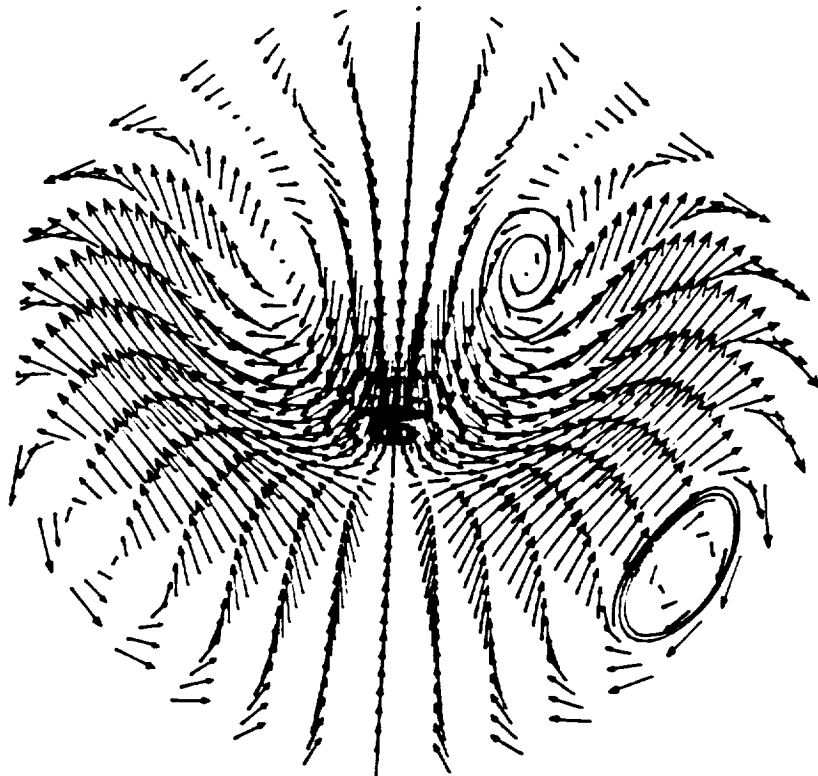


Figure 20. Cross-Flow Velocity Vectors for Lift Jet at  $90^\circ$  Incidence.

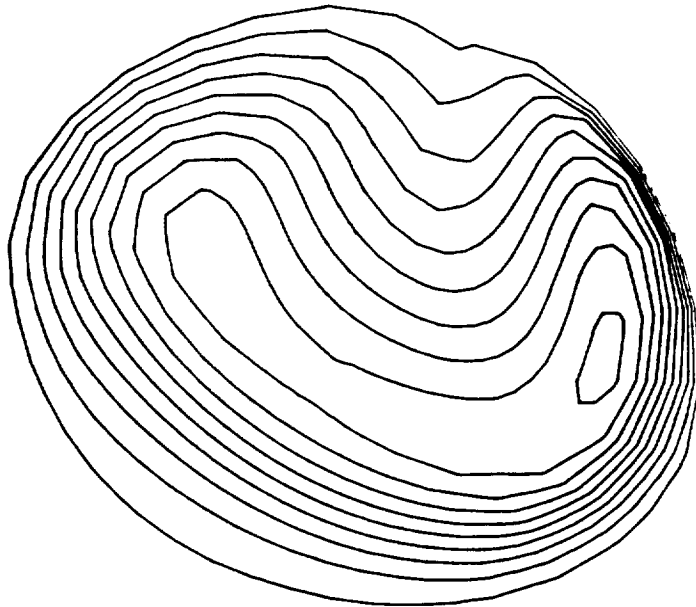


Figure 21. Streamwise Velocity Contours for Vectored-Thrust Jet at  $90^\circ$  Incidence.

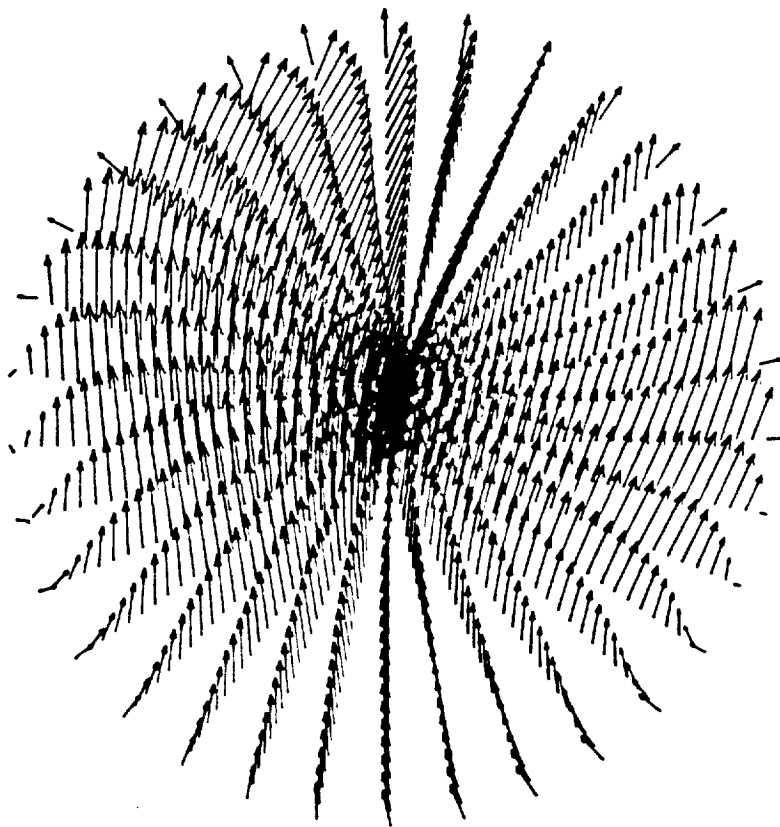


Figure 22. Cross-Flow Velocity Vectors for Vectored-Thrust Jet at  $90^\circ$  Incidence.

## 5.0 CONCLUSION AND RECOMMENDATIONS

The initially proposed approach of using APPL with an elliptic pressure equation and VSAERO with a jet wake treatment proved adequate for the current objectives, although a stronger entrainment modeling seemed necessary. The results from the first three cases are very encouraging, whereas the dual jet case requires more development. The poor correlation in the latter case is mainly ascribed to the lack of description of geometry details. It is noted that the potential flow solution from a panel method is heavily dependent upon how well a geometry input is described. Further, a confluent jet situation, which was not expected, added complexity to the dual jet analysis which is beyond the scope of the PNS method. This required a special treatment of both jet boundaries to be tightened; however, the core development of the jets did ultimately merge, making it impossible to perform separate analyses. In a viscous solution procedure, a PNS method with a space-marching technique experienced some difficulty in starting at an initial plane with the 90° jet. Until that time the iterations between two codes had been done manually, but could be automated after a certain stage. Some steps have been achieved in automating the file communication between the two codes; however, the two codes still run essentially independently. This final step could be automated within a JCL for a particular computer.

By taking these facts into account, the following effort is recommended to expand the capability of the current scheme.

- (1) Enhance the stability of initial starting conditions at a high angle of jet in the cross flow, or use a more robust code like ARC3D (19) instead of APPL to describe the jet plume development.
- (2) Develop a grid generation scheme that is more general to allow treatment of a confluent jet and other multiple viscous zones.
- (3) Complete the automation of the iteration procedure between the two codes.
- (4) Expand the capability of both codes to allow multiple-block calculations. Namely, other viscous regions surrounding a V/STOL geometry might be modeled using, say, ARC3D in addition to the existing plume modeling.
- (5) Generally enhance the graphics capability for treatment of the multiple-block calculations.

### Acknowledgements

This work was sponsored by the NASA Ames Research Center under Contract NAS2-12166, and monitored by Mr. Mike Dudley at NASA Ames.

## 6.0 REFERENCES

1. Hess, J.L., "Calculation of Potential Flow about Arbitrary Three-Dimensional Lifting Bodies", Douglas Aircraft Co. Report MDC J5679-01 (Contract N00019-71-C-0524), 1972.
2. Maskew, B., "Prediction of Subsonic Aerodynamic Characteristics: A Case for Low-Order Panel Methods", J. Aircraft, Vol. 19, No. 2., February 1982.
3. Magnus, A.E. and Epton, M.E., "PAN AIR--A Computer Program for Predicting Subsonic or Supersonic Linear Potential Flows about Arbitrary Configurations using a Higher-Order Panel Method", NASA CR-3251, April 1980.
4. Margason, R.J. et al., "Subsonic Panel Methods--A Comparison of Several Prediction Codes", AIAA 85--0280, January 1985.
5. Boppe, C.W., "Transonic Flow Field Analysis for Wing-Fuselage Configurations", NASA CR-3243, May 1980.
6. Roberts, D.W., "Prediction of Subsonic Aircraft Flows with Jet Exhaust Interactions", AGARD CP-301, May 1961.
7. Clark, D.R., Maskew, B. and Dvorak, F.A., "The Application of a Second Generation Low-Order Panel Method, Program VSAERO, to Powerplant Installation Studies", AIAA 84-0122, Presented at Aerospace Sciences Meeting, Reno, NV, January 1984.
8. Maskew, B., Strash, D., Nathman, J. and Dvorak, F.A., "Investigation to Advance Prediction Techniques of the Low-Speed Aerodynamics of V/STOL Aircraft", NASA CR-166479, February 1983.
9. Maskew, B., Rao, B.M. and Dvorak, F.A., "Prediction of Aerodynamic Characteristics for Wings with Extensive Separations", AGARD CP-291, September 1980.
10. Maskew, B., "Predicting the Aerodynamic Characteristics of Vortical Flows on Three-Dimensional Configurations using a Surface Singularity Panel Method", AGARD CP-342, April 1983.
11. Maskew, B., "An Improved Prediction Method for Powered Lift Vehicle Aerodynamics", Analytical Methods Report 8506, Phase I Final Report under SBIR Contract 04.09.9090, April 1985.
12. Margason, R.J., "The Path of a Jet Directed at Large Angles to a Subsonic Free Stream", NASA TND-4919, November 1968.
13. Maskew, B., "An Investigation to Advanced Prediction Techniques of the Low-Speed Aerodynamics of V/STOL Aircraft", Analytical Methods Report 8603, Final Report under Contract NAS2-11944, May 1986.
14. Shollenberger, C.A., "Analysis of the Interaction of Jets and Airfoils in Two Dimensions", J. Aircraft, Vol. 10, May 1973.

15. Launder, B. and Spalding, D.B., "The Numerical Computation of Turbulent Flows", Computer Methods in Appl. Mech. and Engr., 3, 1974, pp. 269-289.
16. Mineck, R.E. and Margason, R.J., "Pressure Distribution on a Vectored-Thrust V/STOL Fighter in the Transition Speed Range", NASA TMX-2867, March 1974.
17. Schlichting, H., Boundary-Layer Theory, 6th Ed., McGraw-Hill, 1968, pp. 170-174, 218-222.
18. Landis, F. and Shapiro, A.H., "The Turbulent Mixing of Coaxial Jets", Proc. Heat Transfer and Fluid Mechanics Institute, 1951, pp. 133-146.
19. Pulliam, T.H. and Steger, J.L., "Implicit Finite Difference Simulations of Three-Dimensional Compressible Flow", AIAA J., Vol. 18, No. 2, February 1980.

**APPENDIX: FILE MANAGEMENT**

## FILE MANAGEMENT

Under this contract a basic input structure of the VSAERO code has been modified and a capability to read separate input files was added for the purpose of creating a coupling procedure. A schematic flowchart is given in Appendix A.2 and detailed file structures are explained in Appendix A.3

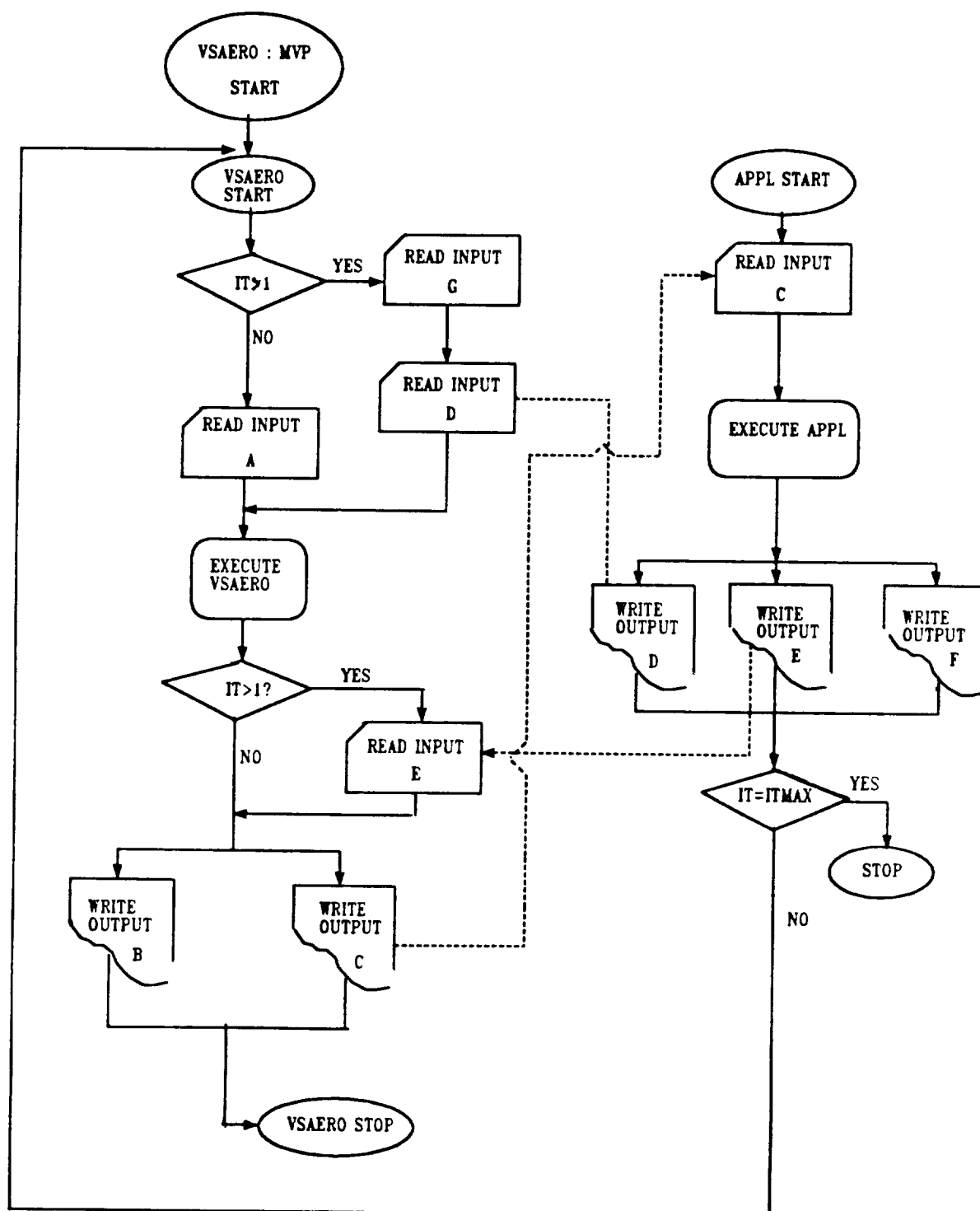
### A.1 File Communication

At the start, the VSAERO code reads a geometry input file, A, which has a jet wake description. At the end of the VSAERO execution, two files are generated. One is the original VSAERO output file, B, and the other is a new file, C, containing a set of jet boundary coordinates and the corresponding velocities.

Then the APPL code reads File C, generates a three-dimensional grid within the jet boundary and marches the solution downstream. During this execution, three separate files are generated as an output set. File D outlines a set of jet core points and the corresponding velocities, and is used to construct jet surfaces with a non-zero entrainment velocity. File E stores an array of outer jet boundaries. File F is a regular APPL output file.

In subsequent iterations, VSAERO starts a new input file, G, which omits the jet wake description in file A. Instead, a File D, passed from the APPL output, is used to construct the latest jet panel surface. After the VSAERO routine calculations, a field velocity scan is made for the points read in File E, and an output file, C, is written. Then the APPL code will begin the next iteration. This procedure continues until convergence is obtained.

## A.2 Flow Chart





### A.3 File Format

FILE A: A standard VSAERO input file with a jet input specification modification.

The new jet scheme is accessed through a new parameter, NGPSYS (for New Grid Plane System, on CARD 19. This must have a value of 1 for the jet; a value of zero is used for the old scheme.

The new jet model must use IDENTW=3 and new jets must be placed after all other wakes in the input file. Also, the new jet model must be used in conjunction with INPUT=5 on CARD 20. This accesses the same centerline trajectory geometry routine as in the earlier program. This routine, JETGOM, generates the jet surface geometry based on the initial orifice shape and the jet centerline trajectory. The trajectory is determined by an empirical expression developed by R.J. Margason (12), and is accurate for injection angles up to 90° with respect to the cross flow and jet velocity ratios through about 8.

The input to JETGOM is complete by specifying the diameter of the jet orifice (DJET) and the jet injection angle in degrees ( $\delta_{JET}$ ). Note that the jet velocity ratio is picked up from CARD SET 23 for the <sup>JET</sup>single jet case. The user may also specify a linear expansion factor (FAC) to be applied to the jet boundary to geometrically simulate the entrainment process. For coaxial jets, best results are obtained by setting the inner jet orifice diameter (DJET) equal to the value of the outer jet and using an average jet velocity for the value of the coaxial jet velocity ratio (VKOAX). This "average" jet velocity does not enter into any of the actual wake strength calculations and is only used to simulate an accurate coaxial jet geometry. provision is made to input schedules of entrainment velocity and total pressure decay.

Damping of the boundary relaxation calculation can be controlled by the user through a parameter, THLIM, which is a limiting angular displacement applied to a line segment in each predictor/corrector cycle. The default value of THLIM is 0.15 radians, but this can be overwritten after setting a negative value on the number of predictor/corrector cycles, NPCMAX, on CARD 3. (The default value for NPCMAX is 2.)

# ADDITION TO VSAERO USERS' MANUAL

## New Jet Specification

### CARD 3: Continued

<u>Columns</u>	<u>Variable</u>	<u>Value</u>	<u>Description</u>	<u>Format</u>
21-15	IMERGE	0	Vortex line merging future option	
26-30	NSUB		Number of subpanel intervals used on a near-field wake panel whose IDENTW>1 during the evaluation of wake influences in PHIMAT subroutine. These subpanels are used only in the streamwise direction here. (Default = 10)	
31-35	NSPMAX		Limit on the number of subpanels per panel used on near-field panels on a wake in the velocity (VEL) routine. (Default = 25)	
36-40	NPCMAX  NPCMAX		Limit on the number of predictor/corrector cycles in the steady (MODE=1) wake relaxation in subroutine WAKREL. (Default=2)	
		>0	If NPCMAX is negative, then CARD 3B must be included to specify the damping for the jet trajectory calculation in each predictor/corrector cycle	

Note: NRBMAX and ITGXXM are only active if the number of panels exceeds 320. For a smaller number of panels, a direct solver is used.

### CARD 3A: User-Specified Block Sizes in Blocked Gauss-Seidel Routine (DUBSOL) (Only if NRBMAX negative on CARD 3)

<u>Columns</u>	<u>Variable</u>	<u>Value</u>	<u>Description</u>	<u>Format</u>
1-10	NROWB(I) I=1,N		Where N= NRBMAX  on CARD 3. Number of rows in each block of the matrix	1615

### CARD 3B: Damping for the Jet Boundary Relaxation. (Only Present if NPCMAX is negative on CARD 3)

<u>Columns</u>	<u>Variable</u>	<u>Value</u>	<u>Description</u>	<u>Format</u>
1-10	THLIM		Limit (radians) on the angular displacement of a line segment in each predictor/corrector cycle; default value is 0.15	F10.0

CARD 19: Wake Card.

<u>Columns</u> 1-5	<u>Variable</u> IDENTW	<u>Value</u>	<u>Description</u> Type of wake	<u>Format</u> 2I5,5X I5,15A4
		1	Regular wake. Doublet distribution is constant in streamwise direction	
		2	Unsteady wake (continuously generated and transported streamwise in time-stepping loop)	
		3	Separated wake. Doublet distribution is linear in streamwise direction with unknown gradient	
		4	Jet model. Doublet distribution is linear in streamwise direction with specified gradient. Requires CARD 23A	
6-10	IFLEXW	0	Flexible wake--will be relaxed if wake shape iteration specified (NWIT>0 on CARD 4(a))	
		1	Rigid wake--will remain fixed throughout wake shape iteration cycles	
16-20	NGPSYS	0	Regular wake grid scheme	
		1	New grid plane scheme. Must have IDENTW=3 on this card, and must have INPUT=5 on CARD 20	
21-80	WNAME		Text for wake identification (optional)	

Note: Limit on number of wakes = 10;  
Limit on number of wake columns = 50;  
Limit on number of wake panels = 1,500.

CARD 20: Continued.

<u>Columns</u>	<u>Variable</u>	<u>Value</u>	<u>Description</u>	<u>Format</u>
26-30	INPUT (Cont'd)	4	Wake line geometry specified by x,y,z coordinates (global reference). Requires OPTION (d) on CARD 21	
		5	For 'jet'-type wakes, jet trajectory generated based on empirical center-line equation. Requires CARD SET 23B	
31-35	NODEWS	0	First or intermediate string of panels being specified	
		3	Completes a wake. Only INPUT and the following variables are active on this card. If INPUT>0, then the appropriate geometry of the last wake line for this wake (CARD 21) must follow	
		5	As for the NODEWS=3, but this completes the last WAKE in the input data	
36-40	IDWC		Future option to change the type of wake (IDENTW) on a column-by-column basis	
41-45	IFLXL		Future option to change the "flexible" status (IFLEXW) on a line-by-line basis	
46-55	DTKET		Option to rotate a wake line geometry about the local x-axis	

- Notes:
- (1) If, in a subsequent case the panel density is changed on a patch crossed by the separation line, then KWPA1, KWPA2 and possibly KWLINE might need to be changed also.
  - (2) The "direction" of the separation line is such that the wake-shedding panels "upstream" of the wake separation are on the left when looking along the line.

CARD 22: Continued.

<u>Columns</u>	<u>Variable</u>	<u>Value</u>	<u>Description</u>	<u>Format</u>
36-40	NPC	0	Manual Intervals. The input points are taken directly	
		>1	Number of intervals to be generated in the region just completed	
41-45			Form of spacing if NPC>0 (See Fig. 15)	
		0	Full cosine spacing with smaller intervals near the beginning of the region	
		1	Half-cosine spacing with smaller panels near the beginning of the region	
		2	Half-cosine spacing with smaller panels near the end of the region	
		3	Equal spacing throughout the region	

CARD SET 23: Additional Parameters for Jets.

CARD 23A: Type-4 Wake Velocity Data. (Only if IDENTW=4 on CARD 19)

<u>Columns</u>	<u>Variable</u>	<u>Value</u>	<u>Description</u>	<u>Format</u>
1-10	VIN		Tangential velocity on the under-side or inside of the vortex sheet wake	8F10.0
11-20	VOUT		As above but on the top side or outside surface	

Note: (1) If just one pair of values is given as above, then the code will set the same values for all columns on this wake. If different values are required on other columns of this wake, then NWC pairs of values must be input on the 8F10.0 format continuing onto additional cards if necessary. NWC is the total number of columns (i.e., number of wake shedding panels) on this wake.

CARD SET 23B: Jet Geometry Specification. (Only if INPUT=5 on CARD 20)

CARD 23B(i).

<u>Columns</u>	<u>Variable</u>	<u>Value</u>	<u>Description</u>	<u>Format</u>
1-10	DJET		Diameter of jet orifice	4F10.0
11-20	DELTAJ		Jet injection angle (deg)	
21-30	THETAJ		Sideways rotation angle of jet orientation (deg)	
31-40	FAC		Factor applied to jet boundary for expansion or contraction. Input value is ration of jet diameter at 10 jet diameters downstream to initial jet orifice diameter. Default = 1.0	

CARD 23B(ii).;

<u>Columns</u>	<u>Variable</u>	<u>Value</u>	<u>Description</u>	<u>Format</u>
1-5	NPL		Number of grid stations (equally spaced) along jet axis	5I5
6-10	NJC	>0	Number of stations where entrainment and/or jet total head decay is specified. Requires CARD SET 23B(iii)	
		0	No entrainment, no total head decay	
		<0	Number of stations where total head decay is specified but entrainment is by Albertson's equation. Requires CARD SET 23B(iii)	
11-15	KOAX	0-OFF 1-ON	For specifying jet injection velocity in the case of coaxial jets. Requires extra card, 23B(iv) if KOAX=1	
16-20	IPRINT	0-OFF 1-ON	Debug print control	
21-25	MFREZ	>0	Grid station beyond which the <u>shape</u> of the jet cross section is frozen	
		0	Cross section shape not frozen	

CARD SET 23B(iii): Jet Entrainment and Total Head Decay. (If |NJC|>0 on CARD 23B(ii)) Total number of cards in set = |NJC|.

<u>Columns</u>	<u>Variable</u>	<u>Value</u>	<u>Description</u>	<u>Format</u>
1-10	SJT		Dimensional distance along jet axis	3F10.0
11-20	VENT		Normal velocity entrainment (positive inwards)	
21-30	DHF		Jet total head decay factor (based on exit condition)	

CARD SET 23B(iv). (If KOAX=2 on CARD 23B(ii))

<u>Columns</u>	<u>Variable</u>	<u>Value</u>	<u>Description</u>	<u>Format</u>
1-10	VKOAX		Average coaxial jet injection ratio; i.e., $V_j/V_\infty$	F10.0

FILE B: This is a standard output file form the VSAERO run.

FILE C:

<u>Columns</u>	<u>Variable</u>	<u>Description</u>	<u>Format</u>
1-10	NPT	Total number of points	I5
1-10 11-20 21-30	$\begin{Bmatrix} X \\ Y \\ Z \end{Bmatrix}$	Coordinates	3F10.4, 5F10.3
31-40 41-50 51-60	$\begin{Bmatrix} V_x \\ V_y \\ V_z \end{Bmatrix}$	Corresponding velocities	
61-70	V	Magnitude of velocity	
71-80	Cp	Pressure coefficient	

Note: NPT = Number of records.

FILE D:

<u>Columns</u>	<u>Variable</u>	<u>Description</u>	<u>Format</u>
1-5	NPCT	Number of points in columnwise direction	2I5
6-10	NPST	Number of points in stationwise direction	
1-13 14-26 27-39	$\begin{Bmatrix} X \\ Y \\ Z \end{Bmatrix}$	Coordinates	6E13.5
40-52 53-65 66-78	$\begin{Bmatrix} V_x \\ V_y \\ V_z \end{Bmatrix}$	Corresponding velocities	

Note: NPCT x NPST = number of records.



FILE E:

<u>Columns</u>	<u>Variable</u>	<u>Description</u>	<u>Format</u>
1-5	NPT	Total number of points	15
1-10 11-20 21-30	$\begin{Bmatrix} X \\ Y \\ Z \end{Bmatrix}$	Coordinates	3F10.4, 5F10.3
31-40 41-50 51-60	$\begin{Bmatrix} V_x \\ V_y \\ V_z \end{Bmatrix}$	Corresponding velocities	
61-70	V	Magnitude of velocity	
71-80	Cp	Pressure coefficient	

Note: NPT = number of records.